# An Urban Surface Energy Balance Model

## To Improve the Representation of Building Geometry for Turbulence Modelling In Urban Areas

Rosalie Kievits

Delft University of Technology

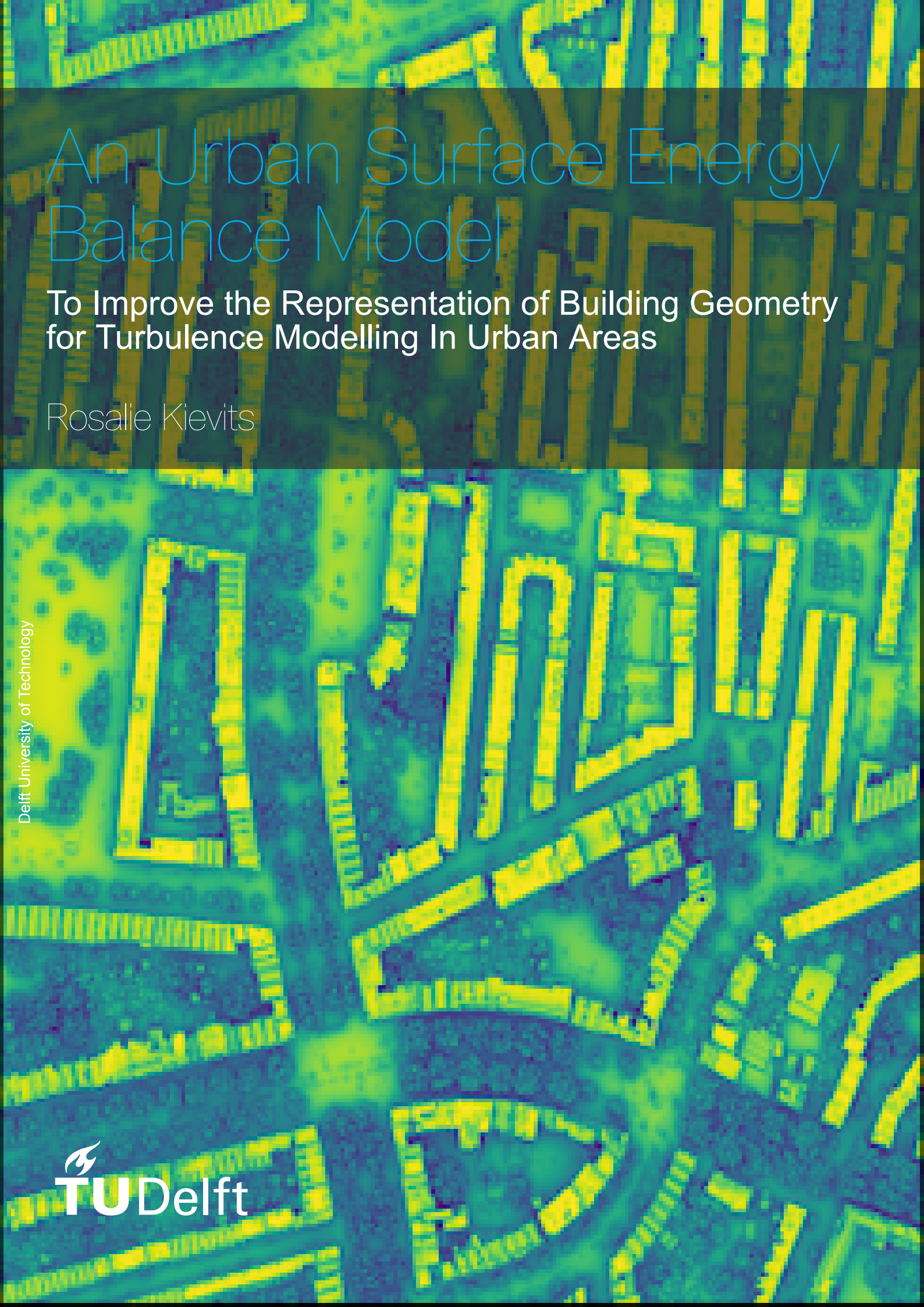

TU Delft

# An Urban Surface Energy Balance Model

## To Improve the Representation of Building Geometry for Turbulence Modelling In Urban Areas

by

Rosalie Kievits

to obtain the degree of Master of Science
at the Delft University of Technology

Student number: 4563921
Project duration: September 5, 2022 – June 9, 2023
Thesis committee:

| | |
|---|---|
| Dr. ir. S.R. de Roode, | TU Delft, supervisor |
| Prof. Dr. Ir. S. Kenjereš, | TU Delft |
| Dr. Ir. S.J.A. van der Linden, | TU Delft |

An electronic version of this thesis is available at http://repository.tudelft.nl/.

TU Delft

# Summary

In this research, a model to simulate the urban surface energy balance (SEB) model is developed. Buildings absorb and reflect shortwave (SW) radiation, and absorb and emit longwave (LW) radiation. Urban geometry, the city's physical layout, plays an important role in the SEB and the resulting surface temperatures. A well-known effect of how building geometry affects radiation is shadowing and trapping of LW radiation. The SEB model takes into account the height and arrangement of buildings. Simulations performed in this study show that when we use different building-resolving methods on the same domain, the amount of net surface radiation and resulting surface temperatures are significantly different.

## Objective of this Thesis

The objective of this thesis is to improve the understanding of how various factors affect the temperature behaviour of urban surface areas, where the focus is on urban geometry and grid averaging techniques. A horizontal domain is considered, where the geometry is determined from the height of the surface with 0.5m resolution, referred to as AHN ('Algemeen Hoogtebestand Nederland') data.

The goal of the energy balance model is to improve weather forecasting in urban areas with building-resolving turbulence models. The turbulence model is referred to as Large Eddy Simulation (LES), but every other turbulence model could be used as well. One of the subjects of this research is how to handle the difference between the grid resolutions of the AHN and the turbulence models, which use larger grid cells. This study quantifies the difference in SEB for different urban geometries and can guide the choice of building-resolving methods for turbulence models.

## Methods

The AHN is used to identify three surface types: roof, ground, and wall surfaces. The surfaces are further divided into horizontal layers. This allows for different materials and boundary conditions to be set for each surface type, and for temperature evolution to be evaluated separately. The environment is simulated through forcing parameters based on theory and data.

In order to capture the surface geometry, two algorithms are developed to calculate the sky view factor (SVF) and shadow factor (SF). The SVF represents how much of the sky is visible for a surface and influences diffuse radiation. The SF determines whether a surface receives direct solar radiation, based on the solar trajectory. These calculations are performed separately for roofs, walls, and roads, and can be computed at different grid resolutions. Both algorithms are verified by comparing values computed with the algorithms to the analytical solutions for an infinite canyon domain.

### The Sky View Factor Algorithm

The algorithm to compute the SVF consists of the following steps: for each data point on the domain, the points that influence the SVF are restricted within a maximum search range. For all points within this range, the area of the sky view that is not visible because of surrounding buildings, is computed by calculating the angle to the top of the building. The SVF is the summation of maximum horizon angles in all directions, subtracted from the total sky view.

The SVFs are computed on a domain in Rotterdam and compared to SVFs computed by the KNMI. We used a newer AHN data set (AHN3) than the version that was used by the KNMI (AHN2). The computed distribution of SVFs is close to known SVF data from the KNMI when the 0.5m AHN data is used, with an average difference of 10%. This disparity can be attributed, in part, to the usage of the newer AHN dataset, since the AHN2 is at least 6 years older. A second reason is that the KNMI uses an algorithm that computes the height of the horizon in 16 directions, whereas our algorithm takes all

obstacles within a maximum search radius into account and remembers the height of the horizon in all $360^o$. Lastly, in this study a minimum height was set below which data is ignored.

### The Shadow Factor Algorithm

The SF calculation employs an algorithm similar to the SVF algorithm. The solar azimuth and solar elevation angle are computed based on the latitude and longitude of our model domain and the UTC and date. For each data point on our domain, all points that have a top view (horizontal) angle with the evaluation point equal to the solar azimuth angle are selected. For all these points the side view (vertical) angle that the top of the obstruction has with the evaluation point is compared to the solar elevation angle. If the side view angle is larger than the elevation angle the point receives no direct SW radiation and the SF is set to 0.

To save computational expenses it is advised to compute the SFs for only one day per week instead of every day. Taking for example a weekly average results in a 7-fold decrease in computational expenses. To justify this, solar positions for different days of the week are compared.

### Sky View and Shadowing for Wall Surfaces

To simplify calculations, the SVF and SF for wall surfaces are estimated from the relation between roads and walls in an infinite canyon. This approach uses geometrical equations from the urban canopy model developed by Masson.

View factors are used to calculate the portion of the radiative heat flux which leaves one surface and strikes another surface. The view factors are used to calculate reflections and are deduced from the SVF, assuming streets resemble a canyon geometry. This method provides the benefits of simplicity and guarantees that all view factors add up to one, a requirement for energy conservation.

### Comparison of Sky View and Shadowing for Different Geometries

A grid determined directly from AHN data with a resolution of 0.5m, is compared to ones averaged with a method similar to the building-resolving models such as LES modelling, which usually have coarser grid sizes. The LES method considers 3D grid cells, where a grid cell has volume $\Delta x_{LES} \cdot \Delta y_{LES} \cdot \Delta z_{LES}$. An LES grid cell is considered part of a building if the volume is more than half filled, and empty if it is less than half filled. This gives a different city topography, which effect is captured by the difference in the SVF and SF.

SVFs are computed for 0.5m, 2.5m and 12.5m cell-size AHN grids, as well as 2.5m and 12.5m LES grids, for three domains. For lower-resolution AHN data, computed SVFs are higher, and the variability of the SVFs over the domain diminishes. For the LES-averaged grids the shift depends on the chosen new grid cell sizes and the tendencies are different for the different surface types.

## Main Findings

### Comparison of Two Geometries

The surface energy balance is simulated for both a 0.5m resolution AHN data grid and a 2.5m resolution LES-averaged grid. The mean SVF for the 2.5m grid is 0.38, compared to 0.6 for the 0.5m grid. The difference in SVF is largest for ground surfaces, with an SVF of 0.18 for the 2.5m grid versus 0.48 for the 0.5m grid. The roof SVF is 0.46 versus 0.68 and the wall SVF is 0.15 versus 0.31 for the 2.5m and 0.5m grids, respectively.

The SFs vary less throughout the day for the 2.5m grid. Because of the lower peak at midday, less direct shortwave radiation is absorbed: The 0.5m AHN grid reaches a maximum mean SF value of 0.69 whereas the 2.5m LES grid only reaches a maximum mean SF value of 0.41.

The two different grids result in large difference in SVF and SF values, which result in temperature differences up to around 6 K for the simulations run in this study. The simulations are affected by all simulation parameters, of which the aerodynamic resistance, outside temperature and building temperature, are discussed.

## Reflections of Shortwave and Longwave Radiation

The fluxes that compose the SEB are evaluated for both grids, and the surface temperature evolution is compared. The net absorbed SW radiation shows the greatest difference between the two grids for ground surfaces, relative to roof and wall surfaces, because the $SVF_{ground}$ differs most. Peak net SW values for the ground are a factor three higher for the 0.5m grid compared to the 2.5m grid. Comparing the peak SW values between the 0.5m and 2.5m grid results in a difference of a factor 1.5 for roof surfaces, and factor 2 for wall surfaces. The difference in absorbed SW radiation is mainly due to the radiation absorbed from the sky.

In terms of LW radiation, the 0.5m grid again predicts larger fluxes compared to the 2.5m grid. The largest difference in emitted LW radiation is again observed for ground surfaces, where the difference between the two grids is three times larger than the difference for both wall and roof surfaces. The 2.5m grid predicts a larger LW contribution from other surfaces, while the 0.5m AHN grid predicts a larger contribution from the sky. Additionally, the temporal fluctuations in LW emission are smaller: The difference for ground surfaces between minimum and maximum net LW during the simulation time of two days is three times lower for the 2.5m grid compared to the 0.5m grid.

Excluding reflections results in higher temperatures for both grids. This difference is however smaller for ground surfaces compared to roof surfaces. This is because the ground and wall surfaces receive more radiation reflected or emitted by other surfaces compared to roof surfaces. By excluding reflections, all radiation received from the sky is absorbed, which is a larger contribution to the net radiation of roof surfaces due to higher SVFs, compared to the net radiation of ground and wall surfaces. It is important to note that in the model, only first-order reflections are considered, which are assumed sufficient in the simulations since the reflected fluxes are small. However, other materials should be evaluated to explore the possibilities and necessity of incorporating additional reflections.

Because of the net radiation differences, predicted peak surface temperatures are higher for the 0.5m grid, which has higher SVFs, and the daily temperature variations are shown to be underestimated when using the 2.5m grid. The biggest difference in peak temperature is for ground surfaces, with a difference of up to 6 K for the used simulation parameters. The maximum temperature difference between the two grids for roof surfaces is smaller, of up to 2.5 K and the maximum temperature difference for wall surfaces is 2 K, three times smaller than the difference for ground surfaces.

## Sensible Heat Flux

The sensible heat flux (SHF) is calculated using the aerodynamic resistance to heat ($R_h$), which is geometry-dependent. This value is unknown and therefore used as a simulation parameter. To understand the impact of SHF on the SEB, simulations were conducted for $R_h$ values of 150 s/m and 30 s/m on both the 0.5m and 2.5m grids.

Comparing SHFs for both grids reveals that ground SHFs are most affected by the grid averaging procedures. Ground surface SHFs for the 0.5m AHN grid show significant temporal variations, while for the 2.5m LES grid, the rise in SHFs during daytime disappears: The SHF for the ground surface with an $R_h$ of 150 s/m reaches a maximum four times higher for the 0.5m grid compared to the maximum SHF for the 2.5m grid. The difference in mean SHF is however small between the two grids for both aerodynamic resistances.

The comparison of SHFs for the two aerodynamic resistances within each grid shows that the maximum difference occurs for roof surfaces. The temporal mean difference between the $R_h$ of 150 s/m and 30 s/m for roof surfaces is similar for both grids. However, the maximum difference can become significant, suggesting that the aerodynamic resistance of the surface has a significant effect on SHF flux and temperature. Therefore it is recommended to investigate the influence of grid geometry on the aerodynamic resistance of the surface, but this is beyond the scope of this research.

## Building Heating Temperature

In our model, a bottom layer boundary condition on the roof and wall surfaces is imposed to simulate the typical temperature control in buildings by heating or cooling systems. This alters the emitted grey body radiation and sensible heat flux, which is investigated by varying the indoor temperature ($T_{building}$)

and outdoor weather conditions.

Comparing the 0.5m and 2.5m LES grids, the variation in SHF between daytime and nighttime is reduced for the latter. The largest difference in SHF is observed for ground surfaces, where the SHF for the 0.5m grid reaches a four times higher maximum in summer, and three times higher maximum in winter, compared to the 2.5m grid. For ground surfaces, the mean difference in net LW radiation between the grids is again most significant due to the large disparity in sky view factors.

## Conclusion

From the results, we conclude that the choice of grid has a significant impact on surface temperature and energy fluxes. Surfaces with smaller SVFs absorb less SW radiation, which is the largest share of the net radiation during the day. Simulated peak temperatures are therefore much lower. Surfaces with smaller SVF values emit less LW radiation and have higher view factors, leading to a larger LW-trapping effect. The SHF is also affected by the choice of grid size. The largest difference between the two grids in simulated fluxes and temperatures is for ground surfaces for all simulations.

The findings show the importance of carefully considering grid size when modelling energy balance in urban areas. Simulated heat fluxes differ up to a factor 3 for two different grids, and temperature differences between the two grids are up to several Kelvin. By understanding how the geometry of urban areas influences the surface energy balance, we can develop more accurate models to improve turbulence modelling in cities and predict urban heat islands.

*Rosalie Kievits*
*Delft, June 2023*

# Contents

**List of Symbols and Abbreviations** **1**

**1 Introduction** **3**
1.1 Surface Energy Balance . . . 3
1.2 Surface Geometry . . . 4
1.3 Thesis Structure . . . 4
1.4 Background . . . 5

**2 Literature** **7**
2.1 Urban Canopy Models . . . 7
2.2 Sky View Factor . . . 7
2.3 Representing the Variability of the Urban Geometry . . . 8
2.4 SVF Calculations Based on Different Inputdata . . . 8
2.4.1 DSM and DTM Data . . . 9
2.5 Grid Resolution . . . 9
2.6 Shadow Casting . . . 9
2.7 Material Properties . . . 9
2.8 Sensible and Latent Heat Flux . . . 9

**3 Applications of Theory and Physical Principles** **11**
3.0.1 The Surface Energy Balance . . . 11
3.1 The SVF Using the AHN . . . 13
3.1.1 SVF for Wall Surfaces . . . 14
3.1.2 Reflections . . . 16
3.2 Shadow Casting . . . 18
3.2.1 Solar Position Algorithm . . . 18
3.2.2 Shadow Factor . . . 19
3.2.3 SF for Wall Surfaces . . . 20
3.3 Components of the Surface Energy Balance Equation . . . 21
3.3.1 SW Radiation Budget . . . 21
3.3.2 LW Radiation Budget . . . 23
3.3.3 Latent and Sensible Heat Fluxes . . . 24
3.3.4 Conductive Heat Flux . . . 25
3.4 Assumptions . . . 26

**4 Methods** **27**
4.1 The Grid . . . 27
4.1.1 Larger Resolution Grids . . . 28
4.1.2 LES Averaging . . . 28
4.1.3 Grid Comparison . . . 29
4.2 Sensitivity Analysis of the SVF . . . 33
4.2.1 Grid Resolution . . . 33
4.2.2 Maximum Search Radius . . . 34
4.2.3 Steps in the Horizontal Angle . . . 35
4.3 Verification of the SVF . . . 36
4.3.1 Infinite Canyon . . . 36
4.3.2 KNMI SVF Map . . . 36
4.3.3 SVF Distributions . . . 37
4.3.4 SVF Map . . . 38
4.3.5 Mean SVF Comparison . . . 39

4.4 Verification of The Shadow Casting Algorithm . . . 41
4.4.1 Solar Position Calculator . . . 41
4.4.2 SF Validation for an Infinite Canyon . . . 42
4.4.3 SF Distributions . . . 43
4.4.4 Shadow Factor Map . . . 46
4.4.5 SF for LES Averaged Grid . . . 47
4.5 The Three Different Surfaces . . . 48
4.5.1 Separating Surface Types . . . 48
4.5.2 Influence of the Grid on Surface Fractions . . . 48
4.6 Number of Layers . . . 49
4.6.1 Material Properties . . . 51
4.7 Boundary Conditions . . . 51
4.8 Model Forcings . . . 52

**5 Results** **53**
5.1 Comparison of Two Geometries . . . 53
5.1.1 SVF and SF Differences . . . 54
5.1.2 SEB Differences . . . 54
5.2 LW and SW Budget Components . . . 55
5.2.1 Shortwave Radiation . . . 55
5.2.2 Longwave Radiation . . . 55
5.3 Surface Temperature Evolution . . . 57
5.3.1 Including versus Excluding all Reflections . . . 57
5.3.2 Including Shortwave or Longwave Reflections . . . 57
5.3.3 Main Take-Away . . . 57
5.4 Sensible Heat Fluxes . . . 59
5.4.1 Comparison of the Aerodynamic Resistances for Both Grids . . . 59
5.4.2 Comparison of the Grids for Both Aerodynamic Resistances . . . 60
5.5 Different Building Heating Temperatures . . . 62
5.5.1 Sensible Heat Flux . . . 62
5.5.2 Longwave Radiation . . . 62
5.5.3 Surface Temperature . . . 63

**6 Discussion and Recommendations** **65**
6.1 SVF and SF Computation . . . 65
6.1.1 DSM Data . . . 65
6.1.2 The Discretization in SVF and SF Algorithms . . . 65
6.1.3 Wall SVF and SF . . . 66
6.2 Reflections . . . 67
6.3 Simulation Parameters . . . 67
6.4 Aerodynamic Resistance to Heat . . . 68

**7 Conclusion** **69**

**A Appendix: Visualisation of the SVF** **71**

**B Appendix: SVFs for 2 more neighbourhoods** **73**
B.1 2nd Neighbourhood . . . 73
B.1.1 SVF PDFs . . . 73
B.2 3rd Neighbourhood . . . 73
B.2.1 SVF PDFs . . . 74

**C Appendix: Solar Position 1st of November** **77**

**D Appendix: Shadow Factor Averaging** **79**
D.1 SF Distributions for gridratio 25 . . . 79
D.2 SF Distributions for gridratio 50 . . . 80

**E Appendix: 3rd Grid** **81**

# List of Symbols and Abbreviations

## Abbreviations

| | |
|---|---|
| $UHI$ | Urban Heat Island |
| $DALES$ | Dutch Atmospheric Large Eddy Simulation |
| $LES$ | Large Eddy Simulation |
| $LiDAR$ | Light detection and ranging |
| $RRTM$ | Rapid Radiative Transfer Model |
| $UCM$ | Urban Canopy Model |
| $SEB$ | surface energy balance |
| $SVF$ | sky view factor |
| $SF$ | shadow factor |
| $LCZ$ | local climate zone |
| $DEM$ | Digital Elevation Model |
| $DSM$ | Digital Surface Model |
| $DTM$ | Digital Terrain Model |
| $AHN$ | Algemeen Hoogtebestand Nederland |
| $KNMI$ | Koninklijk Nederlands Meteorologisch Instituut |

# Symbols

| | | |
|---|---|---|
| $SF$ | shadow factor | [0,1] |
| $SVF$ | sky view factor | [0,1] |
| $C$ | volumetric heat capacity | $JK^{-1}m^{-3}$ |
| $t$ | time | $s$ |
| $T$ | temperature | $K$ |
| $d$ | layer thickness | $m$ |
| $SW$ | shortwave radiation flux | $Wm^{-2}$ |
| $LW$ | longwave radiation flux | $Wm^{-2}$ |
| $LHF$ | Latent heat flux | $Wm^{-2}$ |
| $SHF$ | sensible heat flux | $Wm^{-2}$ |
| $G$ | conductive flux | $Wm^{-2}$ |
| $\lambda$ | heat conductivity | $Wm^{-1}K^{-1}$ |
| $\sigma$ | Stephan Boltzman constant | $5.67Wm^{-2}K^{-4}$ |
| $\epsilon$ | emissivity | - |
| $a$ | albedo | - |
| $\rho$ | density | $kgm^{-3}$ |
| $C_p$ | heat capacity under constant pressure | $JK^{-1}$ |
| $\theta$ | potential temperature | $K$ |
| $L_v$ | latent heat of vaporization | $kJkg^{-1}$ |
| $q$ | specific humidity | $gkg^{-1}$ |
| $Z_0$ | roughness length | $m$ |
| $A$ | surface area | $m^2$ |
| $\delta$ | franctional area | - |
| $h$ | building height | $m$ |
| $\Delta x$ | gridbox length | $m$ |
| $R_{max}$ | maximum search radius | $m$ |
| $r$ | radius | $m$ |
| $\beta$ | azimuth angle between data points | radians |
| $\psi$ | vertical angle between heights of data points | radians |
| $\Delta$ | julian day | day |
| $UTC$ | Coordinated Universal Time | hour |
| $\omega$ | hour angle | radians |
| $\delta$ | daily declination value | radians |
| $\alpha_s$ | solar elevation angle | radians |
| $\gamma_s$ | solar azimuth angle | radians |

# 1

# Introduction

The urban surface energy balance has been studied around the world for decades, but recently interest has increased due to the consequences of climate change (Van Hove et al., 2011).
A growing population, increasing energy consumption and anthropogenic heat production cause an increase in the urban heat island (UHI) effect, with temperatures transcending the human comfort range (Dirksen et al., 2019). Urban Heat Islands emerge when densely built areas replace vegetation, where the pavements and buildings consisting of artificial materials absorb and retain heat. This has severe consequences: During heat waves, areas of high pressure create stagnant air, concentrating air pollution in urban areas (Center for Science Education, 2023). Furthermore, this induces the spreading of viruses and heat-related diseases and increases energy costs for air-cooling. On top of this, changing lifestyles and the urbanization of the world have caused urban areas to be responsible for 2/3 of the global energy consumption (Ali et al., 2021), this is expected to worsen over the coming decades and has therefore become a popular field of research (Agathangelidis et al., 2019; Schrijvers, 2020).
Urban geometry plays a significant role in the surface energy balance (SEB) and the resulting surface temperatures. Therefore, understanding how different urban geometries affect the SEB is important for improving our ability to mitigate the UHI effect and design sustainable urban environments.

## 1.1. Surface Energy Balance

The urban surface energy balance, visualized in figure 1.1, consists of the net shortwave (SW) and longwave (LW) radiation, the latent and sensible heat flux, and the conductive flux into the ground. A net heat flux will result in a temperature change of the surface.

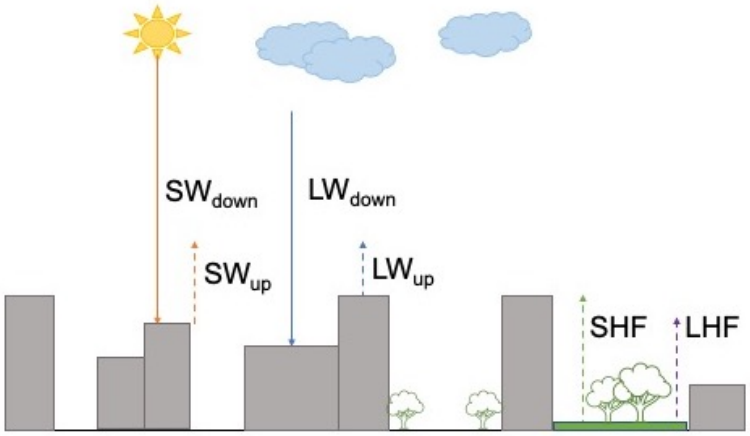


Figure 1.1: Fluxes of the Urban Surface Energy Balance: The net shortwave (SW), which is the difference between $SW_{down}$ and $SW_{up}$. The net longwave (LW) flux, which is the difference between $LW_{down}$ and $LW_{up}$, and the latent (LHF) and sensible (SHF) heat flux. A net heat flux will result in a conductive flux into the ground, and causes a temperature change of the surface.

The influence of different heat fluxes on the temperature of surfaces in the city, and the detail with which each should be taken into account, are investigated, with an emphasis on the representation of the urban geometry. The differences in behaviour between buildings and rural terrain impact the boundary layer of the atmosphere (Harman N, 2003), which is the part of the atmosphere directly influenced by the Earth's surface. Simulations can provide insight into how the presence of buildings influences the different heat fluxes that form the surface energy balance. Thereby we can enhance weather and dispersion simulations and help in environmentally aware city planning to reduce UHI effects (Agathangelidis et al., 2019; Van Hove et al., 2011).

## 1.2. Surface Geometry

The absorption, retention, and emission of radiation by a surface depend on both the surface material properties and geometry. A well-known effect of how building geometry affects the radiation is shadowing and trapping of LW radiation shown in figure 1.2.

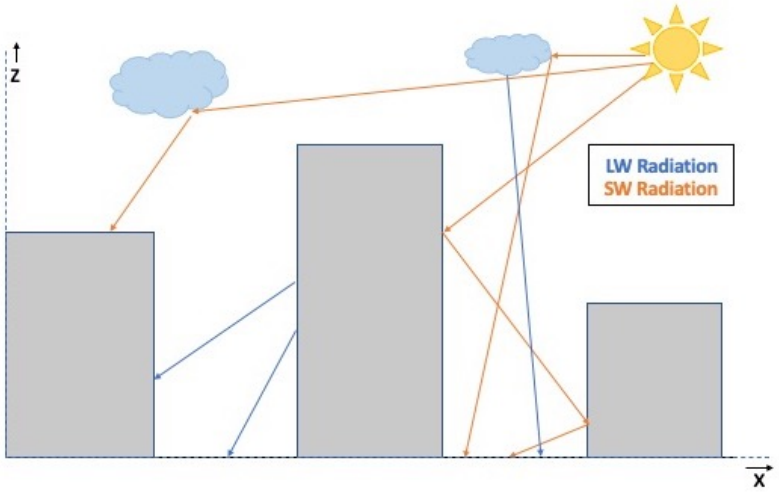


Figure 1.2: The absorption and emission of longwave (blue) and shortwave (orange) radiation, and the reflections between buildings. The leftmost building does not receive direct solar radiation due to the high middle building but receives diffuse solar radiation. The clouds and buildings themselves emit longwave radiation. Radiation can be absorbed or reflected by a surface. Multiple reflections between the two rightmost buildings cause solar radiation to eventually reach the ground surface.

However, incorporating the geometry of cities and reflections from other surfaces is complex. A simplified approach also applied in this thesis, is to include view factors and material properties of other surfaces in the net radiation equations.

Two key parameters in determining radiation for a geometry are the sky view factor (SVF) and the shadow factor (SF), both of which will be computed with an algorithm. The SVF represents how much of the sky is visible and influences diffuse radiation, and the SF determines whether a location receives direct solar radiation based on the solar trajectory.

## 1.3. Thesis Structure

Previous studies and literature on which the research is built are discussed in Chapter 2. In Chapter 3: Theory, all physical principles of the model are presented, and the algorithms to compute the SVF and the SF are explained. In Chapter 4: Methods, the assumptions and parameters of the model are discussed. In Chapter 5: Results, the results of the simulations are presented. In Chapter 6: Discussion, these results are discussed and recommendations for future studies are presented. From all of this, a conclusion can be drawn which is done in Chapter 7: Conclusion.

## 1.4. Background

The goal of surface energy balance modelling applied to turbulence models, including in this research, is to improve high-resolution turbulence and building-resolving simulations of the atmosphere in urban areas.

Dales, a turbulence-resolving large-eddy simulation (LES), is an advanced meteorological modelling system for turbulence modelling. A Rapid Radiative Transfer model (RRTM) is used to model the radiation fluxes through the atmospheric columns. In the RRTM the radiation fluxes are calculated, taking molecules, water vapour and cloud formation into account. These fluxes are used as input in our SEB model.

# 2

# Literature

In this research a model to simulate the urban surface energy balance model is developed. Buildings absorb and reflect SW radiation, and absorb and emit LW radiation. To simulate these fluxes, the study applies modelling techniques sourced mainly from literature. While there exist numerous urban surface energy balance models, each with varying assumptions and simplifications to account for the complexity and diversity of cities, reviews and comparisons of different methods are scarce, as noted by Ali et al. (2021).

## 2.1. Urban Canopy Models

This research adopts the Urban Canopy Model (UCM) approach from Masson (2000) to separate surfaces into roof, ground and wall surfaces, and the equations for LW and SW radiation budget as the basis for our net LW and SW equations. The UCM distinguishes three types of surfaces: roof, road and wall surfaces, with each type having a different temperature, but surfaces of the same type are equal (i.e. two rooftops consist of the same materials and have the same temperature). In UCMs the urban geometry is composed of rows of homogeneous buildings characterized by the height-over-width ratio, which is the ratio of the canyon height over the canyon width indicated in figure 2.1. The LW and SW radiation fluxes are emitted at the top of the urban canyon. Among others, Masson, Wang et al. (2011a) and Kusaka et al. (2001) have developed UCMs to use as the boundary condition for a larger atmospheric LES simulation and validated the models with data (Masson et al., 2002; Wang et al., 2011a).

This study investigates the effect of implementing a less simplified geometry, as the radiation terms in reality depend heavily on the surface orientation, shading, and field of view (Suter et al., 2022).
To represent the urban geometry with more detail, a method based on the *'Algemeen Hoogtebestand Nederland'* (AHN) of the Netherlands is developed to compute the sky view factor and shadow factor based on raster-based data.

## 2.2. Sky View Factor

The SVF is a key parameter that determines the amount of diffuse SW and LW radiation absorbed and emitted by surfaces. It ranges between 0 and 1 and is affected by the surrounding buildings, which limit the amount of radiation that a surface receives. Surfaces with low SVF values warm up more slowly, but at night they become relatively warmer than surfaces with higher SVFs, causing an increase in the net heat storage within buildings and contributing to the Urban Heat Island effect (Jiao et al., 2019; Schrijvers et al., 2015; Baghaeipoor & Nasrollahi, 2019; Dirksen et al., 2019; Van Hove et al., 2011).

In UCMs, SVFs and SFs are typically computed from simple geometric parameters such as the height-over-width ratio. In the models of Masson, Wang et al. and Kusaka et al. this ratio is the same for every street, and there is only one SVF for each of the three surface types. The simplicity of these models allows for analytical solutions for the SVF to be computed. In the UCMs the direct SW radiation

is multiplied with a function of the height-over-width ratio and the position of the sun, this factor is called the shadow factor in this research. In figure 2.1 the SVF and SF for an infinite canyon are indicated.

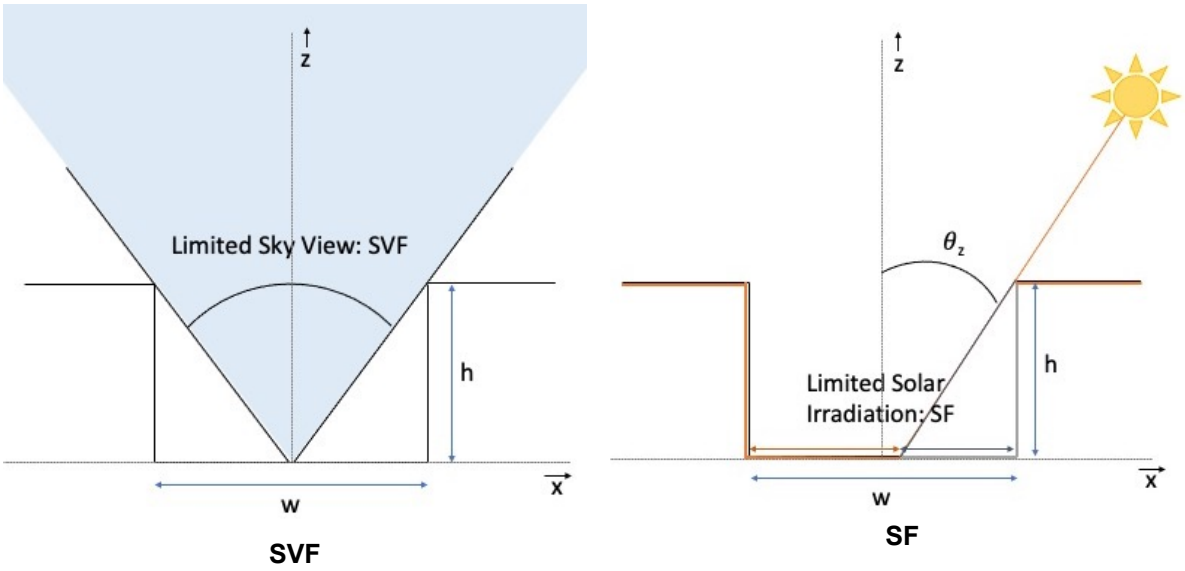


Figure 2.1: Schematic of an infinite canyon. On the left the SVF is indicated, which is the visible portion of the sky. On the right the SF is indicated, which is the fraction of direct solar radiation a surface receives. Both the SVF and SF depend on the height-over-width ratio, indicated in the figure, and the SF also depends on the solar zenith angle $\theta_z$

## 2.3. Representing the Variability of the Urban Geometry

To accurately represent the variability of urban geometries with varying building heights and widths, an algorithm is used to compute the Sky View Factor (SVF). Previous studies have used algorithms to compute SVF for complex and real urban domains, converging to analytical SVF solutions for infinite canyon geometry (Dirksen et al., 2019; Kastendeuch, 2013; Lindberg & Grimmond, 2010; An et al., 2014).

Another approach to compute a more variable SVF is to take a similar approach in computing SVFs solely from geometric parameters as with an infinite canyon but to derive the geometric parameters from data averages of a specific city (Hammerberg et al., 2018; Agathangelidis et al., 2019; An et al., 2014; Ferreira et al., 2021; Bernard et al., 2018; Tsirantonakis & Chrysoulakis, 2022) .
Determining the height-over-width ratio and other geometric parameters for an entire city at once has been shown to reduce the variability and not be representative of the extreme ranges. To solve this issue the city can be divided into local climate zones (LCZ) where a distinction is made for different zones depending on building height, open surface / built area fractions and other factors. This way a distinction can be made between suburbs, centre, and green areas and a more accurate SVF can be calculated. Nonetheless, determining the average geometric parameters for each LCZ presents its own challenges. (Bernard et al., 2018; Ferreira et al., 2021; Hammerberg et al., 2018). Therefore in this research the SVF is computed with an algorithm directly.

## 2.4. SVF Calculations Based on Different Inputdata

To determine SVFs for more complex geometries geo-spacial data is used. This is a common approach, but data formats vary among methods. A main differentiation between different SVF calculations can be made in the input data, where fish-eye or street view pictures (images) is one category, and vector or raster data that represent the location of obstructions as the other (Middel et al., 2018). Since Fish-eye pictures are not as widely available as height data, in this research the latter option is used.

### 2.4.1. DSM and DTM Data

A rectangular array with heights of each point can be constructed from Digital Surface Model (DSM) and Digital Terrain Model (DTM) data, which can be used for SVF algorithms (Desthieux et al., 2018; Kastendeuch, 2013; Dirksen et al., 2019). The wide availability of DSMs supports the applicability of this method, and is also used in this research as input data. DSM and DTM data of the Netherlands is available from the AHN site with a resolution of either 0.5 or 5m. This can then be filtered and scaled to the desired resolution with an averaging algorithm.

## 2.5. Grid Resolution

The accuracy of the SVF algorithm is influenced not only by the data input but also by other parameters. In a study by Dirksen et al. (2019), who used DSM data as well to develop an SVF map for the KNMI, it was found that decreasing the grid resolution leads to a lower UHI temperature raise, leading to the conclusion that SVF needs a high grid resolution of at least 1m to accurately capture houses and trees. Overestimating the SVF can lead to an overestimation of the escaping LW and SW radiation, resulting in an underestimation of the UHI effect as the LW trapping effect of buildings is not represented accurately. However, a smaller grid size will slow down computations and limit the size of the domain. Other parameters such as the maximum search radius and angular step division are compared to results in this study as well.

## 2.6. Shadow Casting

The solar trajectory is taken into account to predict if a location receives direct radiation or that this is blocked by surrounding buildings. The challenge to accurately determine direct solar irradiation without overextending computational resources is one of the subjects of this research.
The relative position of the sun can be calculated using the latitude and longitude of the location and time of the year (Bhattacharya et al., 2021). A shadow-casting algorithm that leaves a pattern of ones and zeroes depending on whether or not a point receives direct sunlight is developed, based on previously developed algorithms (Lindberg & Grimmond, 2010; Ratti & Richens, 2004).
The same method was used and validated with data of Geneva (Desthieux et al., 2018). This took over 900 hours to run however, demanding too many computational expenses. In this research we will investigate which assumptions about the solar trajectory can be made to reduce these computational expenses.

## 2.7. Material Properties

Besides geometry, the UHI effect is caused by surface coverage of artificial materials in city's (Tsirantonakis & Chrysoulakis, 2022; Oswald et al., 2019; Schrijvers, 2020; Yaghoobian et al., 2010). The city's surface coverage consists of a wide range of materials, but an assumption of the most used materials can be made by for example setting one material for each surface type (i.e. walls, rooftops, roads (Masson, 2000)).

The surface materials of the other surfaces are included in the net radiation equations, together with the view factors that represent reflections between different urban surfaces. Another way to address reflections is to use a ray-tracing or Monte Carlo approach, but these methods are computationally intensive (Löwe & Helbig, 2012). Several numerical methods exist to calculate view factors between surfaces, since in most cases the analytical solution to the problem is not known (Suter et al., 2022). The effect of considering one or more reflections and the influence of surface material properties is discussed in this research as well.

## 2.8. Sensible and Latent Heat Flux

In this study the influence of the SHF and LHF on the total SEB is evaluated by varying the aerodynamic resistance as a parameter. The SHF depends on the aerodynamic resistance to heat $R_h$, which is sensitive to many parameters and therefore hard to calculate (Wang et al., 2011b; McShane et al., 2017). The $R_h$ however has important consequences for urban meteorology and related applications (Yang et al., 2019). Analytical solutions exist based on roughness lengths, but determining the aero-

dynamic resistances is not the main goal of this research. Therefore in this research, the aerodynamic resistance is a parameter that is varied to investigate the influence of the sensible heat flux on surface energy balance (Yang et al., 2019; Masson, 2000; Grimmond & Oke, 1998).

# 3

# Applications of Theory and Physical Principles

In this research, the influence of the urban geometry on the surface energy balance equation is explored. The buildings, determined from the AHN data, cast shadows and influence the LW and SW radiation. The goal of the energy balance model is to improve weather forecasting in urban areas with high-resolution building-resolving models. One of the subjects of this research is how to handle the difference between the grid resolution of the AHN and the resolution of the turbulence models. The turbulence model is referred to as LES, but every other turbulence model could be used as well.

First, the surface energy balance equation, the principle equation of the model, is presented. The way urban geometry influences the different components of the SEB is explained in the first part of the chapter, followed by a more detailed explanation of all the different fluxes part of the SEB. The presented physical equations are used to model the heat exchange of the urban surface with the air above it.

### 3.0.1. The Surface Energy Balance

The surface energy balance equation in eq. 3.1 forms the basis of the model used to evaluate the SEB. The absorption and emission of different fluxes at the top of the surface are components in the surface energy balance equation, and cause heating or cooling of the Earth surface as shown in figure 3.1.

$$C\frac{\delta T_s}{\delta t} = \frac{1}{d}(SW_{net} + LW_{net} - SHF - LHF - G_{out}) \tag{3.1}$$

$SW_{net}$ and $LW_{net}$ represent the net shortwave and net longwave radiation fluxes, SHF and LHF are the sensible and latent convective heat fluxes. These four fluxes penetrate the top layer of the surface. The conductive flux G is the ground heat flux that goes into the subsurface layers. For every layer below the top layer there is thus a conductive heat flux from the above layer, $G_{in}$, a heat flux to the next layer, $G_{out}$, resulting in a net heat flux $G_{net}$.

The change of the surface temperature $T_s$[K] is proportional to the volumetric heat capacity $C$[J/m$^3$K] of that material and the thickness of the layer, $d$[m]. In a surface energy balance model coupled to a building-resolving model, the received direct and diffuse radiation is computed by a radiative transfer model. Direct solar radiation is received in a straight line from the sun. Diffuse solar radiation is caused by Rayleigh scattering of sunlight, clouds and aerosol particles. The absorbed fluxes depend on the surface geometry and material properties and are thus computed by the SEB model.

The influence of urban geometry on the surface energy balance is captured by two factors named SVF and SF. The first influences all diffuse radiation, the latter one influences direct radiation only.

The amount of visible sky for a surface compared to the unobstructed sky, known as the SVF, determines the surface's ability to absorb and emit diffuse radiation. In appendix A the SVF is visualised as a fisheye picture; this is how one would observe the limitation of sky view when standing between

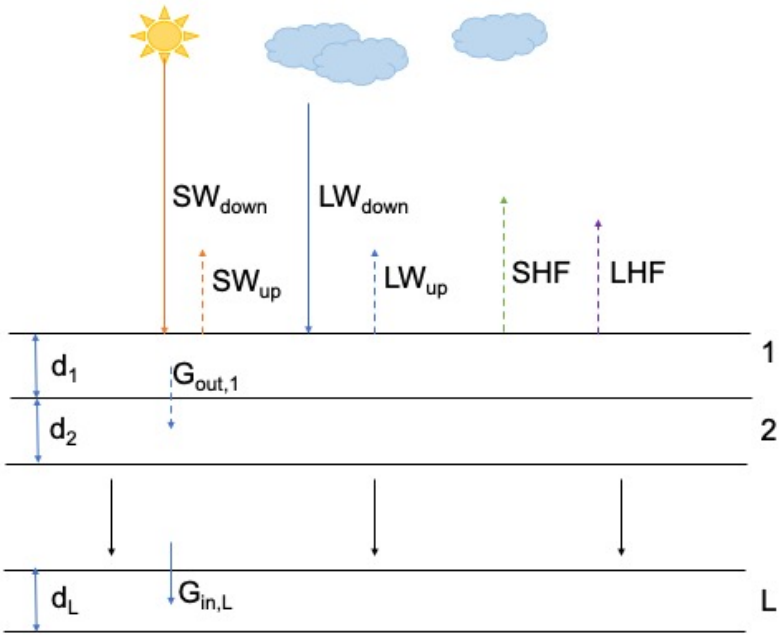


Figure 3.1: Schematic of the surface energy balance. Incoming fluxes (solid lines) add positively to the net radiation of that layer, outgoing fluxes (dotted lines) negatively. The surface consists of L layers, indicated with the numbers 1,2,...L, with layer thicknesses $d_1, d_2, \ldots d_L$. The (shortwave) SW, longwave (LW), and sensible and latent heat fluxes (SHF and LHF) only contribute to the net heat flux of the top layer. For all other layers there is a net conductive heat flux $G_{net}$, which is the difference between $G_{in}$ and $G_{out}$.

buildings. The SVF is 1 for surfaces without any obstruction and decreases to 0 when buildings and trees emerge until no direct light is seen. It therefore influences the LW radiation budget, since LW radiation is diffuse, and the diffuse part of the SW radiation budget.

The shadow factor is a factor between 0 and 1 that tells if a surface is irradiated directly by the sun. This factor is 0 for a surface if another building is in the same direction as the sun and high enough, such that it blocks the direct SW radiation flux.

The $SW_{net}$ and $LW_{net}$ are thus influenced by the SVF and SF, which in turn cause a temperature change, which comprises the boundary condition for the sensible heat fluxes and conductive heat flux. In this research, the SVF and SF are computed using an algorithm and the height at every point (the AHN). This algorithm is explained in the following section.

## 3.1. The SVF Using the AHN

When using the AHN of the Netherlands, a SVF can be computed for every location, based on the heights of all the surrounding buildings. This algorithm is based on the ones used by Dirksen et al. (2019) and Jiao et al. (2019). The AHN is divided in square boxes with dimensions x-cells and y-cells, where every grid cell has length $\Delta x_{AHN} = \Delta y_{AHN}$. The data thus consists of a 2D array of size x-cells times y-cells with the height at $[x_{AHN}, y_{AHN}]$ for this entry. Since the cells are square the length of a gridbox of the AHN is referred to as $\Delta x_{AHN}$ from now on.

The first step in the algorithm is to assume only a limited amount of points of the AHN, within a certain radius, influence the SVF at a certain location. Therefore, all points in the AHN outside a defined radius, referred to as $R_{max}$, can be left out of the calculation, and points with a lower height than the evaluation point within $R_{max}$ can also be omitted. The grid and $R_{max}$ are shown in figure 3.2.

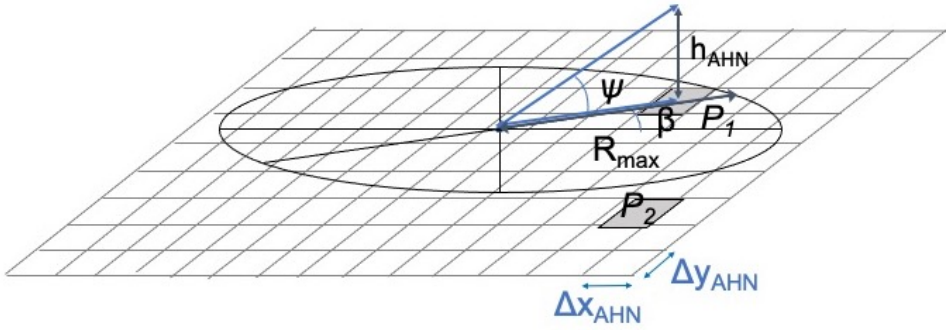


Figure 3.2: The point under evaluation on a raster view, with maximum radius $R_{max}$. gridbox $P_1$ is inside $R_{max}$ and will thus be taken into account for the SVF. gridbox $P_2$ is outside $R_{max}$ and is assumed to not influence the SVF because it is to far away. $\beta$ is the horizontal (or azimuthal) angle, and $\psi$ is the vertical angle between the height of two points, where the evaluation point has 0 height in this case.

The angle $\beta$ of a point is defined as the horizontal angle of the point with respect to the evaluation point, as shown in figure 3.3a. $\beta$ can thus range from $0$ to $2\pi$, and is discretized in steps$_\beta$, with each step the size of $2\pi/\text{steps}_\beta$. Every point that has a height $h_{AHN}(x_{AHN}, y_{AHN})$ larger than the height of the point under evaluation forms an obstruction for the sky view.
For all points within the maximum radius, the angle to the top of the obstruction is called $\psi$. $\psi$ is calculated from the height $h_{obstruction}(x_{AHN}, y_{AHN})$ and distance defined as $r^2_{obstruction} = x^2 + y^2$, as shown in figure 3.3b. The angle $\psi$ can thus vary from 0 at ground level to $\pi/2$.

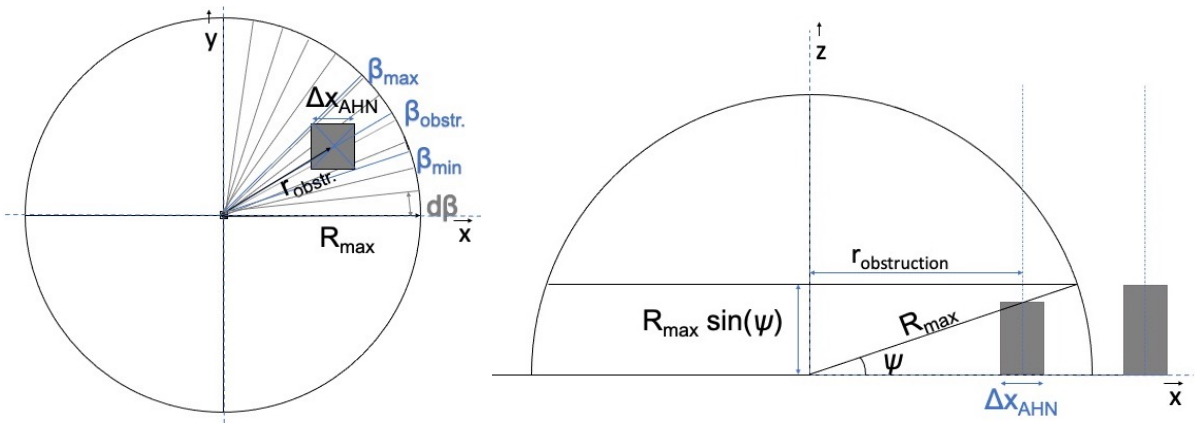


a) Top View b) Side View

Figure 3.3: a) Top view of the SVF calculation: One obstruction, wider than $d\beta$, so it is stored in multiple indices of $\psi_{max}(\beta)$. b) Side view of the SVF calculation: The angle $\psi$, to the top of an obstruction that lies within $R_{max}$, for a certain angle $\beta$

An obstruction close to the point under evaluation, with a small $radius$, thus has a larger angle $\psi$. A larger $\psi$ limits the SVF more, than a building with the same height but at a larger distance. A list with all $\psi$ values keeps track of the largest $\psi$ value for every $\beta$. These $\psi$ values are called $\psi_{max}(\beta)$.

$$\psi = tan^{-1}\left(\frac{h_{obstruction}}{r_{obstruction}}\right) \tag{3.2}$$

The width of the obstruction is calculated in degrees. For all $\beta$ values between $\beta_{\text{min}}$ and $\beta_{\text{max}}$ defined in 3.3 and 3.4, the values for $\psi_{max}(\beta)$ get replaced by $\psi$ unless the current $\psi_{max}(\beta)$ is larger than $\psi$.

$$\beta_{min} = -sin^{-1}\left(\frac{\Delta x_{AHN}}{r_{obstruction}}\right) + \beta \tag{3.3}$$

$$\beta_{max} = sin^{-1}\left(\frac{\Delta x_{AHN}}{r_{obstruction}}\right) + \beta \tag{3.4}$$

If there already exists a larger $\psi_{max}$ for this $\beta$ the current obstruction does not influence the SVF and we move on to the next point. One building can thus correspond to multiple items of the list of $\psi_{max}(\beta)$ as shown in figure 3.3.

The final result is thus a list the size of $steps_\beta$, that has the largest angle of obstruction $\psi_{max}(\beta)$ for all $\beta$. The SVF is calculated by integrating over the visible area. In our case the integral is approximated with a summation over all angles $\psi_{max}(\beta)$ with eq. 3.5. This is repeated for each data point on the AHN domain.

$$SVF = \frac{1}{steps_\beta} \sum^{steps_\beta} cos(\psi_{max}(\beta))^2 \tag{3.5}$$

Shortly summarized, the SVF for every data point is computed as follows: for each data point on the domain, the points that influence the SVF are restricted within a maximum search range. For all points within this range the area of the sky view that is not visible because of surrounding buildings, called obstructions, is computed by calculating the angle to the top of the obstruction. The SVF is the summation of maximum angles to all surrounding buildings subtracted from the total sky view.

### 3.1.1. SVF for Wall Surfaces

This algorithm could be adjusted to also use for wall surfaces. The angle $\beta$, that varies between 0 and $2\pi$ for the horizontal surfaces, varies only between 0 and $\pi$ for the wall surfaces, since it is assumed that the vertical surfaces cannot receive SW and LW radiation from within the building. In figure 3.4 the top view of the $SVF_{wall}$ is visualized.

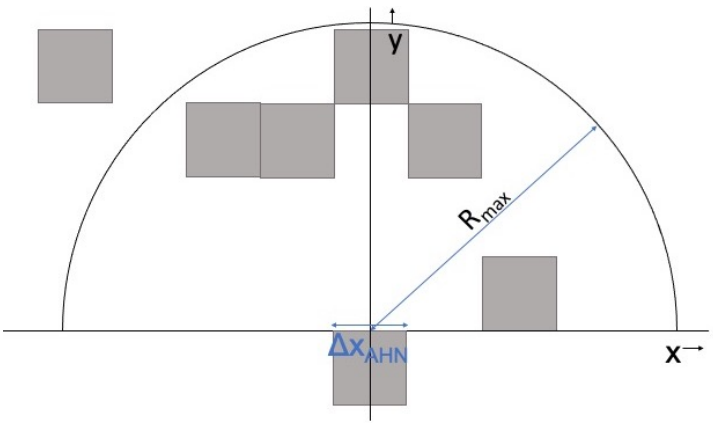


Figure 3.4: Top view of obstructions for the middle of the wall. $R_{max}$ is the maximum search radius.

Since there is a height difference between the bottom and top of the wall $SVF_{wall}$ has to be integrated between 0 and the wall height to find the average. In the figure 3.5 the difference in view factors for a higher point on the wall is clearly visible.

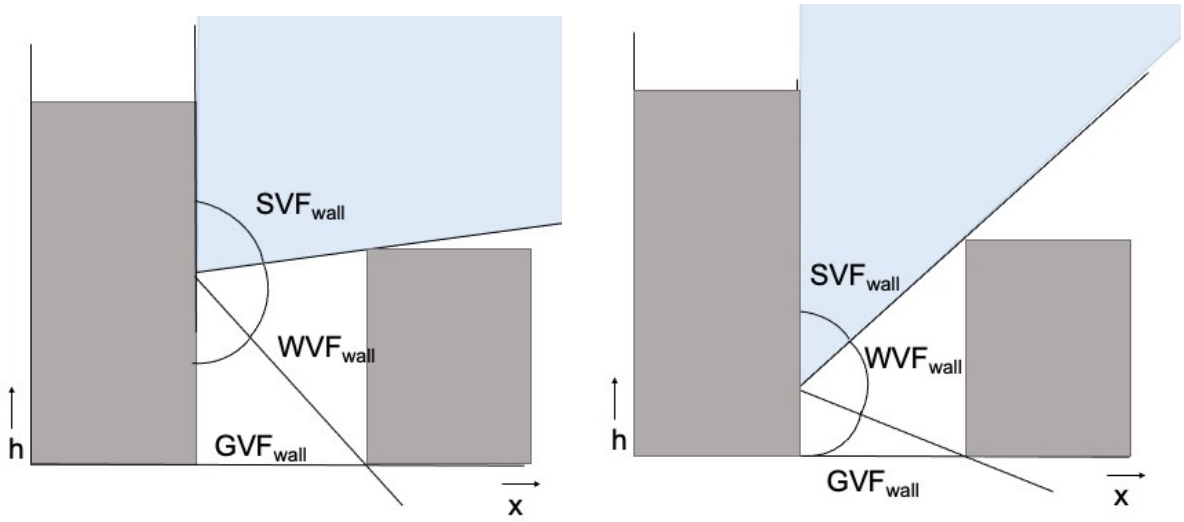


a) High Point b) Low Point

Figure 3.5: side view of $SVF_{wall}$, $WVF_{wall}$ and $GVF_{wall}$ for a high (a) and a low (b) point on the wall, to show the difference in view factors.

Every building has 4 walls, and therefore 4 $SVFs_{wall}$, one on each side, that is computed by numerically integrating the SVF over the height on that side. This can become computationally expensive very fast.

To avoid these extended calculations a novel method is proposed to estimate $SVF_{wall}$: To this end, the city is seen as a large distribution of canyons with different heights and widths, and the $SVFs_{wall}$ are computed with the analytical expressions used in the Urban Canopy Model (UCM). The UCM represents the city as an infinite canyon, where the walls of the canyons are the buildings and the roads are the bottom of the canyon, as shown in figure 2.1. The SVFs and SFs can be computed analytically and are presented here since they are used to verify the SVF and SF algorithms and used to deduce the $SVFs_{wall}$ from $SVFs_{ground}$.

The equations for the SVF in the UCM for road and wall surfaces are integrated over the canyon width and height and therefore only depend on the height-to-width ratio, while the SVF for roof surfaces is 1 at all times. A more detailed derivation can be found in the works of Schrijvers (2020); Masson (2000); Kusaka et al. (2001).

We use Eq.(9) and Eq. (10) from Masson, which read

$$SVF_{ground} = \sqrt{\left(\left(\frac{h}{w}\right)^2 + 1\right)} - \frac{h}{w} \tag{3.6}$$

$$SVF_{wall} = \frac{1}{2}\left(\frac{h}{w} + 1 - \sqrt{\left(\frac{h}{w}\right)^2 + 1}\right)\frac{w}{h} \tag{3.7}$$

By isolating the height-over-width (h/w) ratio from eq. 3.6, the $SVF_{wall}$ can be related to the $SVF_{ground}$, shown in eq. 3.9.

$$\frac{h}{w} = \frac{1 - SVF_{ground}^2}{2 \cdot SVF_{ground}} \tag{3.8}$$

To apply this to our model the grid must be separated into ground and roof surfaces based on a minimum height. The distribution of $SVF's_{ground}$ can be related to distribution of $SVF's_{wall}$ for a certain

domain, or for an LES cell the $SVF_{wall}$ is computed based on the average $SVF_{ground}$ for that grid cell of size $\Delta x_{LES}$.

$$SVF_{wall} = \frac{1}{2}\left[\left(\frac{1 - SVF_{ground}^2}{2 \cdot SVF_{ground}}\right) + 1 - \sqrt{\left(\left(\frac{1 - SVF_{ground}^2}{2 \cdot SVF_{ground}}\right)^2 + 1\right)}\right]\frac{2 \cdot SVF_{ground}}{1 - SVF_{ground}^2} \tag{3.9}$$

### 3.1.2. Reflections

Surfaces have an albedo and emissivity depending on the material, and therefore do not absorb all radiation that reaches the surface. Also, all surfaces emit LW radiation that can be absorbed by other surfaces in their surrounding. The fraction of radiation that leaves one surface and reaches another is described by view factors. The wall view factor for the roof ($WVF_{roof}$) and ground surfaces ($WVF_{ground}$) can be deduced from the fact that all view factors for a surface must add up to one (Kusaka et al., 2001), this is shown in figure 3.6.

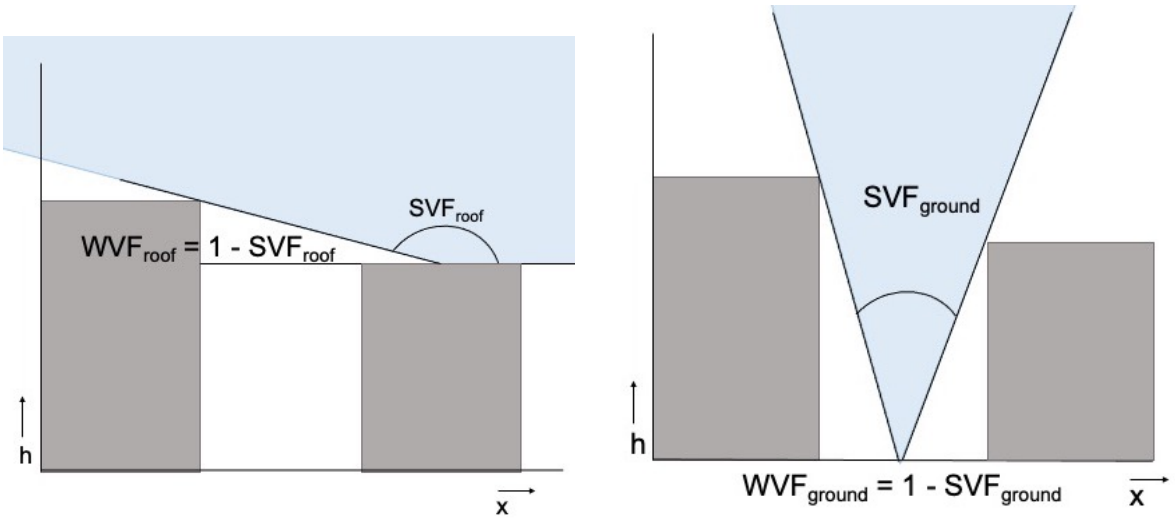


a) Roof b) Ground

Figure 3.6: Side view of the sky view factor (SVF) and wall view factor (WVF) for roof surfaces (a) and ground surfaces (b)

The wall view factor for the roof therefore reads,

$$WVF_{roof} = 1 - SVF_{roof} \tag{3.10}$$

The wall view factor for the ground reads,

$$WVF_{ground} = 1 - SVF_{ground} \tag{3.11}$$

A big difference with the infinite canyon approach, is that when height differences between buildings occur, the SVF for roof surfaces is not one: Some of the light gets blocked by other buildings, and light gets reflected of the walls of other buildings onto the roof. This must mean that some roofs of lower buildings reflect light to the walls of higher buildings as well. A certain roof view factor $RVF_{wall}$ for walls can be taken into account.

$$WVF_{wall} = 1 - SVF_{wall} - RVF_{wall} - GVF_{wall} \tag{3.12}$$

However, $RVF_{wall}$ is very small, and can therefore be neglected. Neglecting this fraction allows for the calculation of the WVF for wall surfaces in the same manner as Masson.

In literature different approaches are found to calculate reflections, varying from neglecting reflection at all, considering one reflection, or considering all reflections till net radiation converges (Harman N, 2003). Here we consider only first reflections. This can be supported by the fact that albedos of

building materials are generally quite low, such that the amount of reflected SW radiation, proportional to the albedo, is also small. The emissivity $\epsilon$, which is proportional to the absorbed and emitted LW radiation, is generally high for building materials (Löwe & Helbig, 2012). Instead of using individual surface thermal properties, only average solar reflective values per grid cell are used, one for all roof surfaces, one for all wall surfaces, and one for ground surfaces.

## 3.2. Shadow Casting

The exchange of diffuse radiation between a surface and the sky is restricted by the SVF, which is a value between 0 and 1 for each data point. Moreover, some points may fall in the shadows of their surroundings due to the trajectory of the sun and surface geometry, which results in receiving no direct radiation. The shadow casting algorithm determines whether a point $x_{AHN}, y_{AHN}$ receives direct SW radiation or not, generating a Boolean value called $SF_{x,y}$. $SF_{x,y}$ is zero when the point is in the shadow and 1 if it receives direct SW radiation. In early morning and late afternoon there are more points $x_{AHN}, y_{AHN}$ with $SF_{x,y} = 0$ compared to midday, just as there are more points $x_{AHN}, y_{AHN}$ with $SF_{x,y} = 0$ in winter compared to summer.

### 3.2.1. Solar Position Algorithm

First the position of the sun can be calculated using the method of (Bhattacharya et al., 2021). The time has to be corrected for the difference in longitude $\lambda$ from the center of time zone definition.

$$\Delta = julianday \frac{360}{365.25} \tag{3.13}$$

The equation of time is the difference between solar time and mean time, this reads

$$EOT = -0.128 \cdot sin(\Delta - 2.80^o) - 0.165 \cdot sin(2\Delta + 19.7^o) \tag{3.14}$$

$$T_{corrected} = T + (\lambda - \lambda_{timezone})/15 + EOT \tag{3.15}$$

where T is the time in hours in UTC, which can be a decimal, i.e. 11:30 a.m. is T = 11.5. $\lambda$ is the longitude of the location, where eastwards is positive and Greenwich is 0.

From this point on we convert to radians as it is the standard angle unit in Python. The daily declination value is calculated as:

$$\delta = sin^{-1}(0.3987 \cdot sin(\Delta - 1.4 + 0.0355 \cdot sin(\Delta - 0.0489))) \tag{3.16}$$

The elevation angle varies during the day and therefore the hourly angle $\omega$ that varies between sunrise and sunset has to be calculated as well, for this we use eq. 3.17. The hour angle is the angular displacement of the sun east or west of the local meridian due to the rotation of the Earth around its axis, and corresponds to $360^o/24\text{hours} = 15^o$ per hour or 0.26 rad, with mornings being negative and afternoon positive.

$$\omega = (T - 12) \cdot 15^o \cdot \frac{\pi}{180} \tag{3.17}$$

The solar elevation angle $\alpha_s$, which we use for the shadow casting algorithm is calculated from the solar declination value $\delta$, the hourly angle $\omega$ and the latitude $\phi$. The solar elevation angle is measured from ground surface and is related to the solar zenith angle $\theta_z$ as $\alpha_s = \pi/2 - \theta_z$:

$$sin(\alpha_s) = sin(\phi)sin(\delta) + cos(\phi)cos(\delta)cos(\omega) \tag{3.18}$$

One obtains the solar sunrise and sunset angles, $\omega_{sunrise}$ and $\omega_{sunset}$, by setting the solar altitude angle to zero (Buter, 2002) as in eq. 3.19. These angles can be converted again to time and the difference between them is defined as the daylength.

$$\omega_{sunset} = cos^{-1}(-tan(\phi)tan(\delta)) \tag{3.19}$$

the solar azimuth angle $\gamma_s$ is obtained by eq. 3.20 (Kalogirou, 2022):

$$sin(\gamma_s) = \frac{cos(\delta)sin(\omega)}{tan(\phi)} \tag{3.20}$$

This is true provided that

$$cos(\omega) > tan(\delta)tan(\phi) \tag{3.21}$$

if not, the azimuth has to be corrected with $\gamma_s = abs(\gamma_s) - \pi$ for morning hours and $\gamma_s = \pi - \gamma_s$ for afternoon hours. To measure from north, such that the angle can be easily compared to the angle we measure between points in the dataset, the azimuth is also corrected with $\pi$.

### 3.2.2. Shadow Factor

The computation of the shadow factor uses the computed elevation angle $\alpha_s$ and azimuth angle $\gamma_s$. In the same manner as for the SVF we iterate over all points in our domain. First all points are selected that have the same angle $\beta$ with the current evaluation point as the solar azimuth angle. In order to compare the top view angle $\beta$ with the azimuth angle of the sun the angle has to be in a certain range of the azimuth angle. This range depends on $\Delta x_{AHN}$ and the distance to the point, as described in 3.22 and 3.23. Assuming the sun produces a collimated light beam, the width of the shadow is considered equal to $\Delta x_{AHN}$, although nuances are discussed in the Discussion chapter 6.1.2.

$$\beta_{min} = -sin^{-1}\left(\frac{\Delta x_{AHN}}{r_{obstruction}}\right) + \gamma_s \tag{3.22}$$

$$\beta_{max} = sin^{-1}\left(\frac{\Delta x_{AHN}}{r_{obstruction}}\right) + \gamma_s \tag{3.23}$$

If the angle with the top of the obstruction is higher than the elevation angle, this point obstructs the light and therefore the Boolean $SF_{x,y}$ becomes 0 for that time and location.

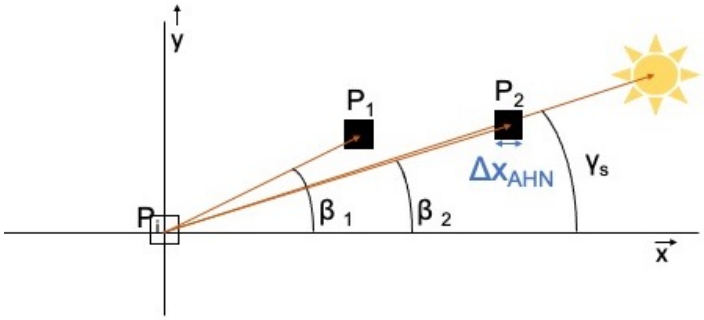


Figure 3.7: The top view for two points on our data set and the azimuth angle of the sun. Point $P_1$ is not in the same direction as the sun, it will not cast a shadow and will therefore not be taken into account in the shadow algorithm. Point $P_2$ has the same angle $\beta$ with the evaluation point as the sun $\gamma_s$, so the next step of the algorithm is to check whether it is high enough to block the sunlight.

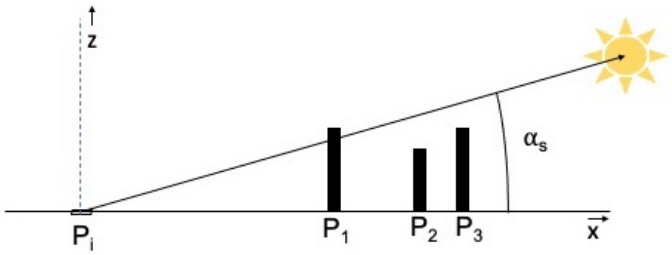


Figure 3.8: The side view for a situation where 3 points are in the same direction as the sun. $P_1$ blocks the sun, that has elevation angle $\alpha_s$. $P_1$ thus casts a shadow on point i and the shadow factor is 0. Point $P_2$ is not high enough to cast a shadow. Point $P_3$ is equally high as $P_1$ but because it is too far away it does not cast a shadow.

Shortly summarized, the SF for a data point P is computed as follows: The solar azimuth and solar elevation angle are computed based on the latitude and longitude of our model domain and the UTC and date. For each data point on our domain, all points that have a top view (horizontal) angle with the point equal to the azimuth of the sun are selected. For all these points the side view (vertical) angle that the top of the object has with the evaluation point is compared to the solar elevation angle. If the side view angle is larger than the elevation angle the point receives no direct SW radiation and the SF is set to 0.

### 3.2.3. SF for Wall Surfaces

To compute the SF for wall surfaces we proceed in the same way as for the SVF. Points on the AHN are split into ground and roof surfaces based on their elevation. From the equations for an infinite canyon geometry the average SFs for wall surfaces are estimated. This is a pragmatic and novel approach, but based on the equations of the SF (eq.(13) - eq.(15)) for the UCM by Masson and Kusaka et al..

The shadow factors for the walls and roads of an infinite canyon are dependent on the height-over-width ratio and the solar position.

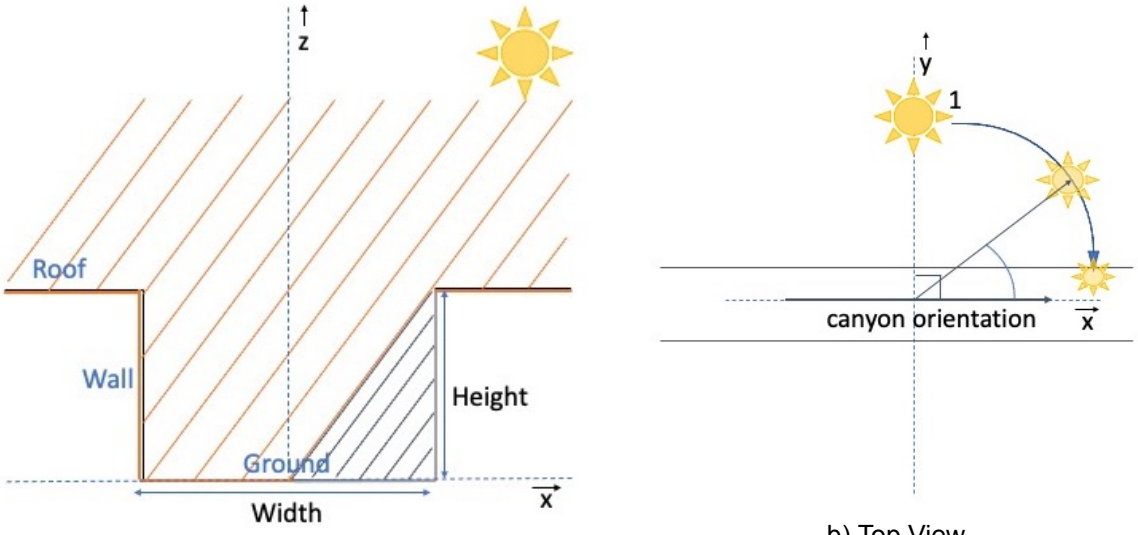


Figure 3.9: a) The side view of an infinite canyon with the sun perpendicular to the canyon direction. Part of the road is shaded and part is sunlit. b) Top view of an infinite canyon. If the sun is in position 1 the solar azimuth is perpendicular to the direction of the canyon. The equations for the SVF and SF are integrated over an azimuthal angle of 360° to account for the different directions of the streets relative to the sun.

When the solar azimuth is perpendicular to the direction of the canyon, indicated as position 1 in figure 3.9b, the SFs are calculated using eqs. 3.25-3.27. The angle $\theta_0$ is then defined as the zenith angle for which the sun begins to illuminate the road.

$$\theta_0 = tan^{-1}\left(\frac{w}{h}\right) \tag{3.24}$$

If the zenith angle is larger than $\theta_0$, $SF_{ground}$ is thus 0. The wall is partly illuminated as shown in figure 3.9a, and $SF_{wall}$ is then defined by eq. 3.25.

$$SF_{wall} = \frac{1}{2}\frac{w}{h} \tag{3.25}$$

If the zenith angle is smaller than $\theta_0$ the sun is high in the sky and the shadow factors are defined by eqs. 3.26 and 3.27

$$SF_{wall} = \frac{1}{2}tan(\theta_z) \tag{3.26}$$

$$SF_{ground} = 1 - \frac{h}{w}tan(\theta_z) \tag{3.27}$$

To calculate $SW_{net}$ in the SEB by Masson, the orientation of all roads and buildings is distributed equally around all directions, and the SF equations are integrated over 360°, to account for the different directions of city streets relative to the sun as shown in figure 3.9b. This results in a new $\theta_0$, which reads:

$$\theta_0 = sin^{-1}\left(min\left[\frac{w}{h}\frac{1}{tan(\theta_z)}, 1\right]\right) \tag{3.28}$$

With this new $\theta_z$, the final SF equations are formed (Eq (13) and Eq. (14) from Masson).

$$SF_{ground} = \frac{2\theta_0}{\pi} - \frac{2}{\pi}\frac{h}{w}tan(\theta_z)(1 - cos(\theta_0)) \tag{3.29}$$

$$SF_{wall} = \frac{w}{h}\left(\frac{1}{2} - \frac{\theta_0}{\pi}\right) + \frac{tan(\theta_z)}{\pi}(1 - cos(\theta_0)) \tag{3.30}$$

In this research a shadow casting algorithm is used on a more complex geometry. Roof and road surfaces are then separated, and the idea is to deduce the wall SF in the same way from the road SF. In this method we thus treat the urban geometry as a distribution of canyons. To relate the SF for wall and ground surfaces we use eqs. 3.28-3.30.

## 3.3. Components of the Surface Energy Balance Equation

The Earth emits, absorbs and reflects radiation. The energy entering and leaving the Earth and its atmosphere are part of the Earth's radiation budget shown in figure 3.1. The largest contribution to the Earth's surface energy balance is SW radiation from the sun. The Earth reflects part of this, based on its surface albedo. The Earth absorbs LW radiation emitted by the atmosphere and emits LW radiation itself. The SW and LW fluxes are influenced by the SF and SVF calculated in the previous section.

### 3.3.1. SW Radiation Budget

The SW radiation budget can be divided into diffuse and direct solar radiation. Diffuse radiation makes up a larger part of SW radiation when the sky is clouded, at higher latitudes, or when the sun is lower in the sky. Moreover, pollution can increase the diffuse radiation percentage. In general, a higher diffuse radiation percentage means a lower total SW irradiance. A radiative transfer model computes the direct and diffuse components of SW radiation, which then serve as inputs to the SEB model.

The reflected SW radiation depends on the albedo $a$ of a surface. The albedo is defined as the reflected SW radiation over the received SW radiation:

$$a = \frac{SW_{out}}{SW_{in}} \tag{3.31}$$

The absorbed SW radiation constitutes the remaining $(1-a)$ of the received SW radiation. If the albedo of the surface material is 0 all radiation is absorbed, and no reflection of SW radiation among the different surfaces occurs. Diffuse received SW radiation is lower for a surface with a lower SVF, since the diffuse radiation is intercepted by the buildings that block the sky view. Only direct radiation gets blocked completely by buildings, shadows are therefore caused only by direct radiation, which effect is captured by the SF.

Part of the diffuse and direct solar radiation gets reflected by other surfaces and then reaches the surface as shown in figure 1.2. At every reflection, part of the radiation gets absorbed, and after multiple reflections the amount of reflected radiation becomes negligibly small. For surface materials with low albedo, the assumption of only first-order reflections can simplify the calculation of the SW radiation budget. The equation for the SW radiation budget, without taking into account reflected fluxes, reads:

$$SW_{net} = SW_{dir}(1 - a)SF + SW_{dif}(1 - a)SVF \tag{3.32}$$

Figure 3.10 shows all processes that occur in the net SW equations presented in eqs. 3.33-3.35. Each surface receives direct SW radiation and diffuse radiation, and a reflected component from the other surfaces.

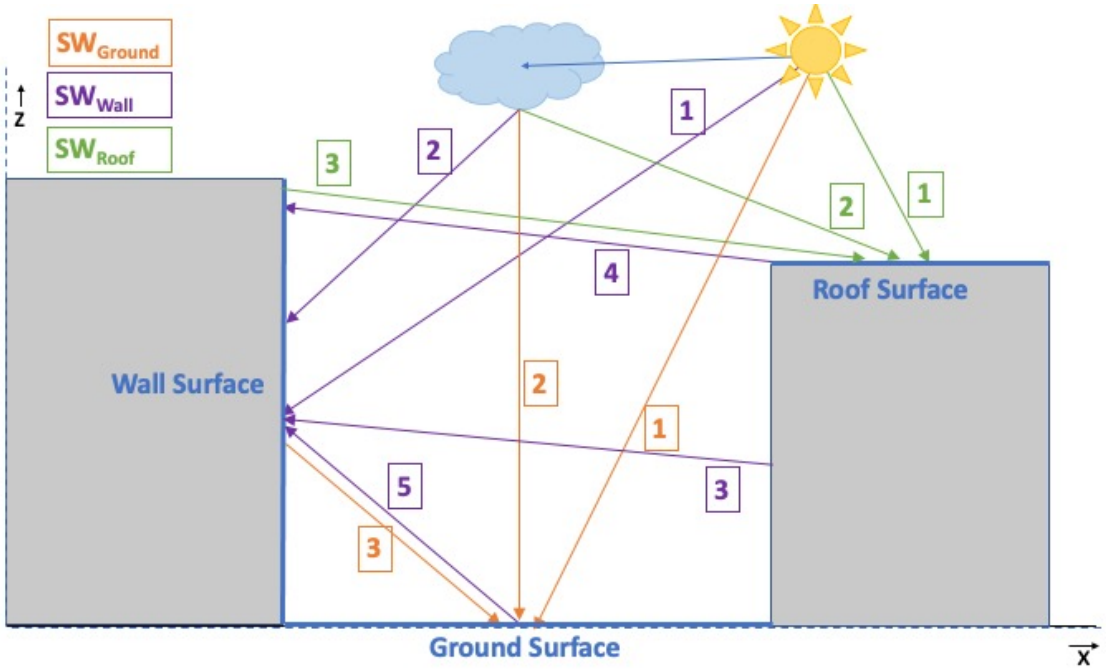


Figure 3.10: Reflection terms of the shortwave equations 3.33, 3.34 and 3.35 visualized and numbered

| Nr. | **Roof** | **Wall** | **Ground** |
|---|---|---|---|
| 1 | Direct SW from the sun | Direct SW from the sun | Direct SW from the sun |
| 2 | Diffuse SW from sky | Diffuse SW from sky | Diffuse SW from sky |
| 3 | Reflected SW from wall | Reflected SW from wall | Reflected SW from wall |
| 4 | | Reflected SW from roof | |
| 5 | | Reflected SW from ground | |

Table 3.1: Legend of figure 3.10

The equations for net SW 3.33-3.35 are based on eqs.(18) - (20) from Masson, but differ in that in this research only first-order reflections are considered. The first-order reflections are deduced from the assumptions stated in section 3.4 and eq. 3.32. An additional term added to Masson's equations is that due to building height variability, roof and wall surfaces can reflect radiation onto each other as shown in figure 3.10 (roof process 3 and wall process 4). In the infinite canyon approach, all roof surfaces have an SVF equal to 1, so these two terms do not occur. In a real city building height can vary a lot and this effect can therefore be taken into account.

These equations are used in the model to determine the net SW for each surface.
In eq. 3.33 the first term is the SW radiation from the sky absorbed by the roof surface. This depends on the albedo of the roof surface, the SVF determining the diffuse radiation, and the SF determining the direct solar radiation. Reflected radiation is diffuse, therefore the distinction between direct and diffuse solar radiation vanishes after the first reflection. The only surfaces that can reflect on the roof surfaces are the wall surfaces of higher surrounding buildings. The second term accounts for that, by determining the fraction of first-order reflected radiation for wall surfaces, proportional to $(1 - \text{albedo}_{\text{wall}})$, and the view factor of wall surfaces to roof surfaces $\text{WVF}_{\text{roof}}$.

The net SW for wall surfaces, eq. 3.34, is similar. The first term accounts for the SW radiation absorbed directly for wall surfaces. The second term is for the absorbed radiation reflected by the other wall surfaces. The third term accounts for the absorbed SW radiation that was reflected by roof surfaces of surrounding buildings that are lower than the current wall surface. This fraction can be neglected to simplify view factor calculations, since this factor is very small if height variations are not large. The last term is for radiation that is reflected from the ground surface.

For ground surfaces, eq. 3.35, the SW radiation balance again starts with the first term determining the absorbed SW radiation from the sky. Ground surfaces can only receive reflected radiation from wall surfaces, represented in the second term.

$$SW_{roof} = (1 - a_{roof}) \cdot (SW_{dir} \cdot SF_{roof} + SW_{dif} \cdot SVF_{roof}) + a_{wall} \cdot (SW_{dir} \cdot SF_{wall} + SW_{dif} \cdot SVF_{wall}) \cdot (WVF_{roof}) \cdot (1 - a_{roof}) \quad (3.33)$$

$$SW_{wall} = (1 - a_{wall}) \cdot (SW_{dir} \cdot SF_{wall} + SW_{dif} \cdot SVF_{wall}) + a_{wall} \cdot (SW_{dir} \cdot SF_{wall} + SW_{dif} \cdot SVF_{wall}) \cdot WVF_{wall} \cdot (1 - a_{wall}) + a_{roof} \cdot (SW_{dir} \cdot SF_{roof} + SW_{dif} \cdot SVF_{roof}) \cdot RVF_{wall} \cdot (1 - a_{wall}) + a_{ground} \cdot (SW_{dir} \cdot SF_{ground} + SW_{dif} \cdot SVF_{ground}) \cdot GVF_{wall} \cdot (1 - a_{wall}) \quad (3.34)$$

$$SW_{ground} = (1 - a_{ground}) \cdot (SW_{dir} \cdot SF_{ground} + SW_{dif} \cdot SVF_{ground}) + a_{wall} \cdot (SW_{dir} \cdot SF_{wall} + SW_{dif} \cdot SVF_{wall}) \cdot (WVF_{ground}) \cdot (1 - a_{ground}) \quad (3.35)$$

### 3.3.2. LW Radiation Budget

Part of the LW radiation emitted by the atmosphere gets absorbed by the earth's surface, based on the material properties of the surface material. The emitted LW radiation is greybody radiation depending on the surface temperature of the earth and linear with the Stephan-Boltzman constant $\sigma$= 5.67e$^{-8}$Wm$^{-2}$K$^{-4}$.

The LW radiation budget, not considering reflections, reads:

$$LW_{net} = LW_{down} \cdot \epsilon \cdot SVF - \sigma \cdot \epsilon \cdot T_{surf}^4 \quad (3.36)$$

For the LW radiation, the first-order reflections are formed the same way as with the SW radiation reflections. We start from the LW equations (eqs. (11) and (12)) from Masson, and combine the assumptions stated in section 3.4. All LW radiation is diffuse and the SF therefore does not occur in the LW radiation budget equations. The net LW equations read:

$$LW_{roof} = \epsilon_{roof} \cdot LW \cdot SVF_{roof} - \sigma \cdot \epsilon \cdot T_{roof}^4 + ((1 - \epsilon_{wall}) \cdot LW \cdot SVF_{wall} + \sigma \cdot \epsilon_{wall} \cdot T_{wall}^4) \cdot WVF_{roof} \cdot \epsilon_{roof}) \quad (3.37)$$

$$LW_{wall} = \epsilon_{wall} \cdot LW \cdot SVF_{wall} - \sigma \cdot \epsilon_{wall} \cdot T_{wall}^4 + ((1 - \epsilon_{wall}) \cdot LW \cdot SVF_{wall} + \sigma \cdot \epsilon_{wall} \cdot T_{wall}^4) \cdot WVF_{wall} \cdot \epsilon_{wall} + ((1 - \epsilon_{roof}) \cdot LW \cdot SVF_{roof} + \sigma \cdot \epsilon_{roof} \cdot T_{roof}^4) \cdot RVF_{wall} \cdot \epsilon_{wall} + ((1 - \epsilon_{ground}) \cdot LW \cdot SVF_{ground} + \sigma \cdot \epsilon_{ground} \cdot T_{ground}^4) \cdot GVF_{wall} \cdot \epsilon_{wall} \quad (3.38)$$

$$LW_{ground} = \epsilon_{ground} \cdot LW \cdot SVF_{ground} - \sigma \cdot \epsilon_{ground} \cdot T_{ground}^4 + ((1 - \epsilon_{wall}) \cdot LW \cdot SVF_{wall} + \sigma \cdot \epsilon_{wall} \cdot T_{wall}^4) \cdot WVF_{ground} \cdot \epsilon_{ground} \quad (3.39)$$

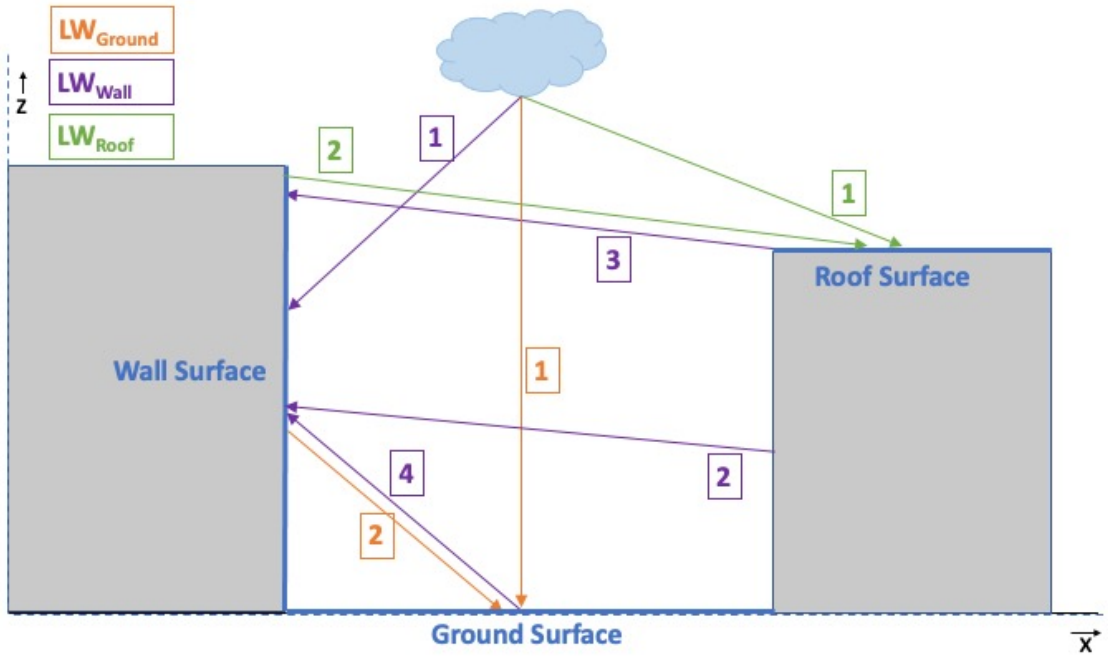


Figure 3.11: Reflection terms of the longwave equations 3.37, 3.38 and 3.39 visualized and numbered

| Nr | Roof | Wall | Ground |
|---|---|---|---|
| 1 | LW from sky | LW from sky | LW from sky |
| 2 | LW emitted by wall | LW emitted by wall | LW emitted by wall |
| 3 | | LW emitted by roof | |
| 4 | | LW emitted by ground | |

Table 3.2: Legend of figure 3.11

The first term of the LW equations is the absorbed LW from the sky. The second is the amount of grey body radiation emitted by that surface. All following terms account for the grey body radiation absorbed by the surface, that was emitted by the other surfaces. The ratio of absorbed radiation versus the radiation that is received by a surface is equal to the emissivity $\epsilon$, according to Kirchoff's law. When the emissivity is equal to 1 all radiation is absorbed, and all blackbody radiation is emitted. For regular building materials, $\epsilon$ is generally close to unity (Suter et al., 2022).

The LW radiation received by the Earth's surface is the radiation emitted by greenhouse gasses. In DALES the downwelling LW radiation is computed by the RRTMG. In this research a simplified LW is used, based on eq. 3.40, to have a realistic forcing for simulations. Many basic empirical methods exist to estimate atmospheric emissivity (K. Wang & Dickinson, 2013), but this is not the goal of this research. Here the emissivity, in eq. 3.41, is adopted from (Schrijvers et al., 2015). This is based on the water vapour pressure $e_a$, the constant c = 46.5 K/hPa and the free stream air temperature $T_a$.

$$LW_{down} = \sigma \cdot \epsilon_{air} \cdot T_{air}^4 \tag{3.40}$$

$$\epsilon_{atm} = 1 - \left(1 + c\frac{e_a}{T_a}\right) \cdot exp\left(-\sqrt{1.2 + 3.0 \cdot c\frac{e_a}{T_a}}\right) \tag{3.41}$$

### 3.3.3. Latent and Sensible Heat Fluxes

The LHF is the energy flux from the surface into the atmosphere originating from water evaporating from or condensing on the surface. Surfaces of artificial materials have different water retention properties than vegetated and unaffected surfaces. Cities therefore drastically alter the water balance and LHFs

are often measured instead of estimated because of the large variety and complexity of structures. In this model only a latent heat flux from water surfaces is considered.

The SHF is the heat flux between the surface and atmosphere due to the turbulent motion of the air above the surface. The increase in total surface area in the city increases the sensible-heat flux per unit plan area. This increase is, however, offset by the reduced efficiency of turbulent transport, which occurs because buildings act as bluff bodies which remove momentum from the airflow through pressure drag (Harman & Belcher, 2006). The SHF is governed by the aerodynamic resistance of the surface and the difference in temperature between the surface and atmosphere.

In the case of a turbulence model, the turbulence model computes the temperature, windspeed, and computes a drag coefficient and aerodynamic resistance. These are input to the surface energy balance model to calculate sensible and latent heat fluxes. The equation for the sensible and latent heat fluxes respectively read

$$SHF = \rho_{air} C_p \frac{\theta_{surf} - \theta_{air}}{R_h} \tag{3.42}$$

$$LHF = \rho_{air} L_v \frac{q_{surf} - q_{air}}{R_l} \tag{3.43}$$

Where $\rho_{air}$[kg/m$^3$] is the air density, $L_v$[J/kg] is the latent heat of vaporization, $C_p$[J/kgK] is the heat capacity of air. The fluxes are induced by a difference in potential temperature $\theta$ and specific humidity q respectively, between the surface and the air above surface. $R_h$ and $R_l$ are the aerodynamic resistances to heat and moisture.
Since the SEB is not coupled to a building-resolving turbulence model, the aerodynamic resistances are not computed but are parameters, used to simulate and evaluate the influence of the LHF and SHF on the SEB.

### 3.3.4. Conductive Heat Flux

Underneath the surface, only a net conductive heat flux causes temperature change. Suppose the ground surface is split in horizontal layers as indicated in figure 3.1, numbered $l = 1, 2, \ldots L$ with $L$ the bottom layer. The temperature of layer $l$ is thus dependent on the conductive flux from or to the two layers $l-1$ and $l+1$ surrounding that layer. This flux is directed outwards of layer $l$ if the temperature is higher in layer $l$ compared to the two surrounding layers.

$$C \frac{\delta T_l}{\delta t} = \frac{1}{d_l}(G_{l-1,l} - G_{l,l+1}) \tag{3.44}$$

The conductive heat flux depends on the heat conductivity $\lambda$[W/mK] of the material.

$$G = \lambda \nabla T = \lambda \frac{\delta T}{\delta z} \tag{3.45}$$

In this model the surface is assumed isothermal in x and y direction, such that the gradient reduces to a derivative in z-direction.

## 3.4. Assumptions

To simulate the urban energy balance some assumptions are necessary. For heat exchange the following assumptions are made, which are customary in SEB models found in literature.

- There is no wavelength dependency except the separation into SW and LW.
- Absorptivity equals emissivity in the LW regime, greybody radiation is thus also emitted proportional to $\epsilon$ (Kirchoff's law).
- Surfaces are isothermal and Lambertian: reflections are diffuse, emitted radiation is diffuse, and the radiosity (leaving radiant flux) is uniform across the facet (Suter et al., 2022). There is therefore no necessity to separately calculate beam reflection and diffuse reflection. (Löwe & Helbig, 2012)
- Facets are either horizontal or vertical ($90^o$ with the ground), but not tilted in between.

Also for the reflections among buildings and when separating the urban surface into roof, ground and wall surfaces, there are some simplifications and assumptions to calculate the view factors. When calculating the view factors for all three surfaces, the following assumptions are made:

- Ground and roof surfaces are horizontal. Ground surfaces can therefore not reflect light to other ground surfaces and the same holds for roof surfaces. Ground surfaces and roof surfaces can not reflect onto eachother.
- Walls are vertical, and the amount of northern, eastern, western and southern facing walls are approximately equal. This is under the assumption we have a large enough domain such that there are many walls and every building has a wall on every side. A wall can therefore see half of the other walls: A southern-facing wall reflects onto northern-facing walls, and half onto eastern or western facing walls.
- all view factors must add up to one

This emphasizes the big role that wall surfaces have in the urban energy balance. Walls are able to reflect and emit radiation onto ground surfaces, and even roof surfaces when the height difference between buildings is large. This causes trapping of radiation between the urban surfaces.

# 4

# Methods

This chapter presents an overview of the model's structure. The model employs a column-based approach to simulate urban energy transfer and simulate the impact of surfaces on turbulence above the city. The AHN is used to identify roof, ground, and wall surfaces, and these surfaces are further divided into horizontal layers. The temperature is calculated for all three surface types, for each layer, and at each timestep.
The column based-approach enables the assignment of different material properties and boundary conditions to different locations. In the simulation results, presented in the next chapter, the roof, wall and ground surfaces have the same material properties and experience the same temperature boundary condition for all grid cells of the domain, and only the SVF and SF are different for every grid cell. The temperatures and fluxes shown in the results are the averaged temperatures and fluxes over the entire domain.

To combine the SEB with a turbulence-resolving model, the high-resolution AHN is transformed into a larger grid cell-size grid, and the averaging procedure for this transformation is discussed in section 4.1. The influence of the grids on the SEB is determined by changes in the SVF and SF, which are discussed in section 4.2. Other parameters affecting the SVF are also examined, and the SVF and SF algorithms are verified. The layers of surfaces and materials are discussed in subsequent sections. The environment is simulated through forcing parameters based on theory and data. The SEB is then simulated under different circumstances, and the results are presented in the Results chapter.

## 4.1. The Grid

The grid is determined from the 0.5m AHN. All heights below a certain minimum height are filtered out. The construction of the AHN and the final grid used is shown in figure 4.1.

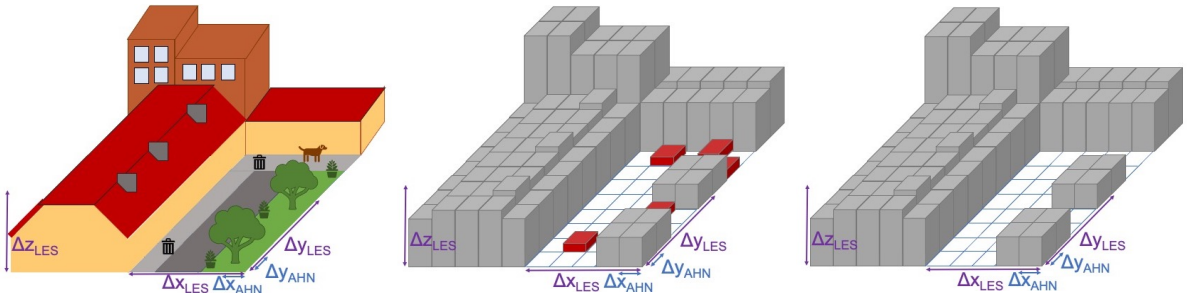


a) Area b) Area in AHN c) 0.5m AHN Grid

Figure 4.1: a) a small block of houses, streets and trees is shown, which is measured by the AHN. b) the data as measured by the AHN, where all detected obstacles are now blocks with length $\Delta x_{AHN}$. The small obstacles such as the dog and trash cans are small heights indicated in red. c) Obstacles below a minimum height are deleted from the data, this results in the final grid.

### 4.1.1. Larger Resolution Grids

The AHN provides free downloads of the height data, called DSM data, in two resolutions: 0.5m and 5m. The 5m resolution AHN is constructed by averaging the 0.5m resolution AHN over 10 grid cells in the x-direction and 10 grid cells in the y-direction. The height thus gets smeared out over the larger grid cell. However, this averaging procedure can be done for every desired grid cell size.

Figure 4.2 illustrates the influence of averaging the building height for a repeating infinite canyon in 2D. The height and width of the building are 20m, and the street width is 10m. On the right of figure 4.2, the same repeating canyon is shown for a 20m resolution grid.

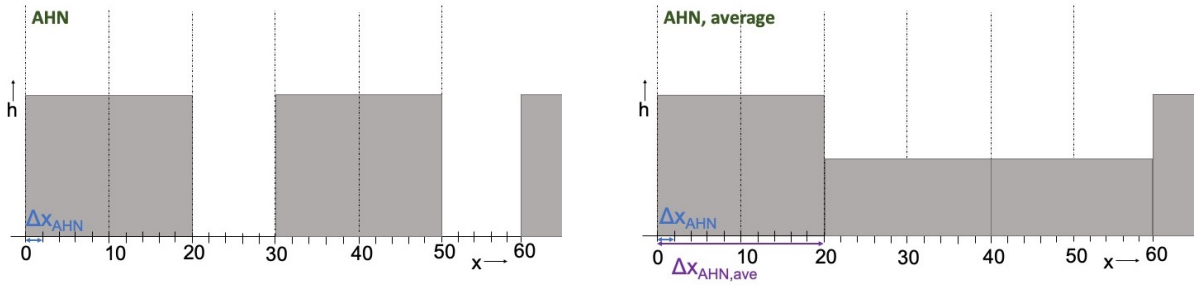


a) Repeating Canyon b) Averaged Repeating Canyon

Figure 4.2: a) 2D schematic of a repeating canyon. b) The repeating canyon averaged over 20m. The second and third grid cell, between 20 and 40m and 40 and 60m, now both have half the height of the canyon over the entire length. The repeating canyon thus has halved in height and doubled in width for the larger grid cell.

In figure 4.2 the building wall is exactly at 20m and thus corresponds to the border of the larger grid cell. However in reality, building edges do not often correspond to grid cell borders. Figure 4.4a shows an example where the buildings are not aligned with the grid of the averaged cells. This causes the averaging procedure to flatten out the grid differently compared to the situation in 4.2.

### 4.1.2. LES Averaging

In turbulence models such as LES, the grid cells are three-dimensional with dimensions of $\Delta x_{LES}$, $\Delta y_{LES}$, $\Delta z_{LES}$, which do not have to be equal. These dimensions are typically much larger than the $\Delta x_{AHN}$ of 0.5m. To represent the irregular shapes of the urban geometry with these rectangular cells, an averaging method is used. If a box is more than half full, it is considered as part of a building, while if it is less than half full, it is considered empty, as shown in figure 4.3.

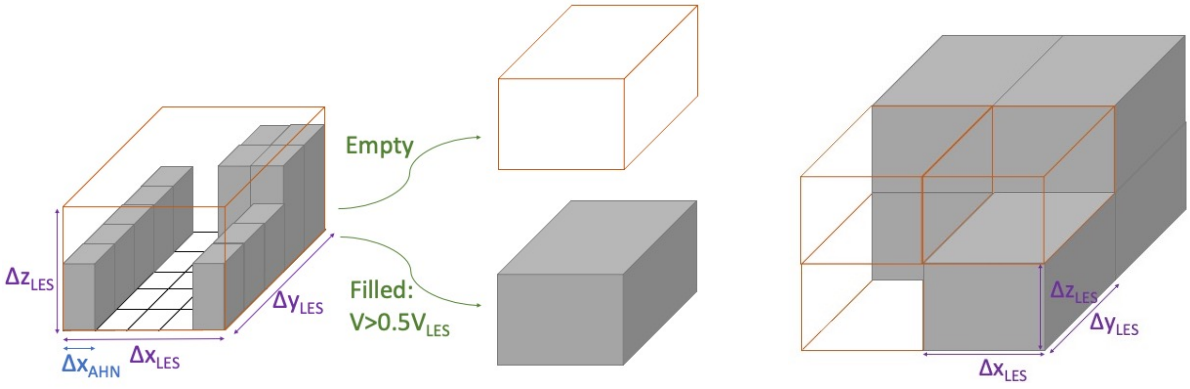


a) LES building resolving method b) Multiple LES cells

Figure 4.3: Averaging Method in LES. a) An LES grid cell, which is partly filled and partly empty, constructed from an AHN grid. The LES grid cell is classified as part of a building if the filled volume V is larger than half the total volume of the LES grid cell $V_{LES}$. b) Multiple LES grid cells on top of each other.

Suppose we take the repeating canyon as shown in figure 4.4a, and apply the LES averaging procedure in 2D, this results in the repeating canyon shown in figure 4.4b.

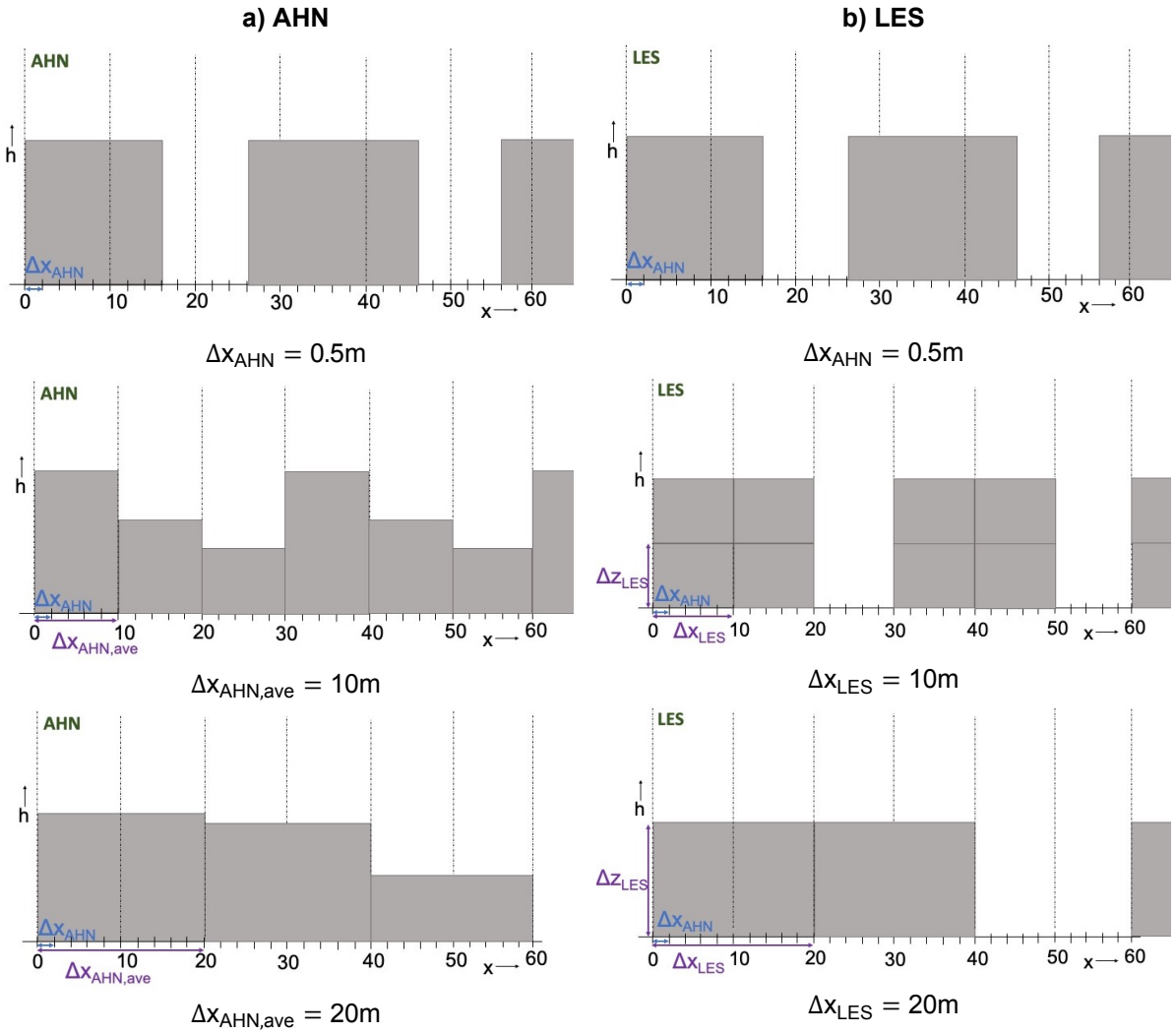


Figure 4.4: In the top figures we see a repeating canyon, where the building wall is not aligned with the larger grid cell. In the middle row the grid is averaged over a new grid length of 10m with both the AHN method (a) and the LES method (b). The wall of the canyon now falls in the middle of a grid cell, causing the grid to be flattened out differently compared to when the wall was aligned with the new grid cells as in 4.2. On the bottom row: The grid is averaged over new grid length of 20m. In a we see that the height differences between neighbouring cells are even smaller. In b we see that, since the original canyon height is not an exact multiple of $\Delta z_{LES}$, the canyon is slightly less deep, and the canyon is twice as wide as the initial repeating canyon.

The grid produced from the same block of houses as seen in figure 4.1 is processed with both the averaging technique used in the larger resolution AHN domains, and the LES averaging procedure, the difference is shown in figure 4.5.

### 4.1.3. Grid Comparison

In figure 4.5 the google maps area and the colourmaps of the grids are shown for 3 domains in Rotterdam. Domain 1, figure 4.5b is a residential area in Rotterdam-West near the Vierambachtsstraat. The main street on domain 2, shown in 4.5c is the 's Gravendijckwal. Domain 3, shown in figure 4.5d, is the area in the city centre between Museumplein and Westblaak.

Domain 1 is the domain used in the results chapter for SEB simulations. The first three grids are grids with a different resolution of the AHN, averaged with the same method as shown in the middle figure of 4.5. Figures 4.2 and 4.4 show in 2D how averaging over larger grid cells reduces the height

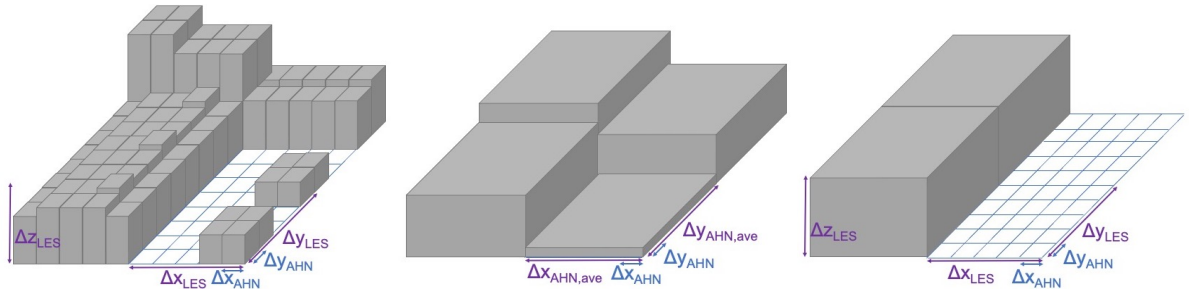


a) 0.5m AHN grid b) AHN averaged grid c) LES grid

Figure 4.5: a) the 0.5m grid determined from the AHN, where heights below the minimum height are filtered out. b) AHN grid averaged over larger resolution grid cell, heights get smeared out over the larger grid cell and height variations become smaller. c) LES grid determined from the 0.5m AHN grid averaged over the same size larger grid cells, only the left row of houses now form two equally sized blocks, the smaller houses on the right side of the domain and the trees have disappeared.

variability, this is also visible from figure 4.5a, where grid 2 and 3 are more blurry compared to the 0.5m resolution grid.

The grids 4-7 are grids processed with LES averaging, thus only heights which are a multiple of $\Delta z_{LES}$ are possible, as in the right figure of figure 4.5. $\Delta x_{LES}$ and $\Delta y_{LES}$ are increased up to 50m, however $\Delta z_{LES}$ is kept at 10m. When increasing $\Delta z_{LES}$ more, the entire grid would disappear, since buildings are not that high in this area. The LES averaging results in more contrast between neighbouring grid cells and a blocky grid. In grid 6 and 7 only large open spaces and the main streets are still recognizable.

**a) 3 Domains on Maps**


**b) Domain 1**

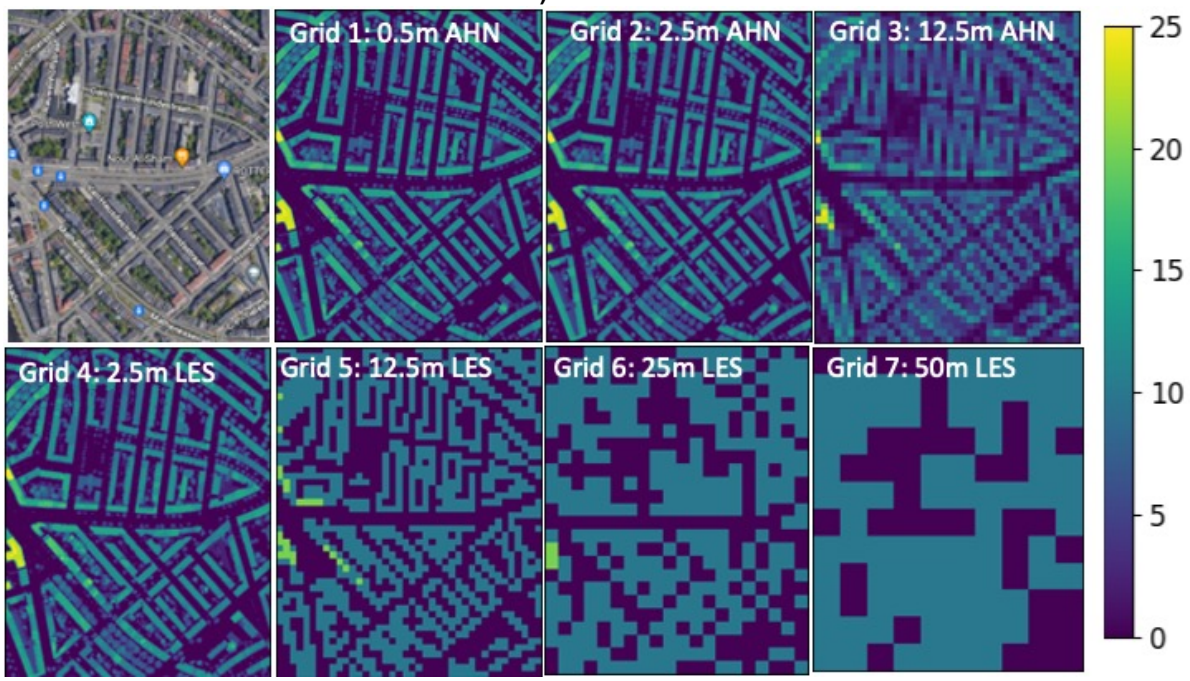

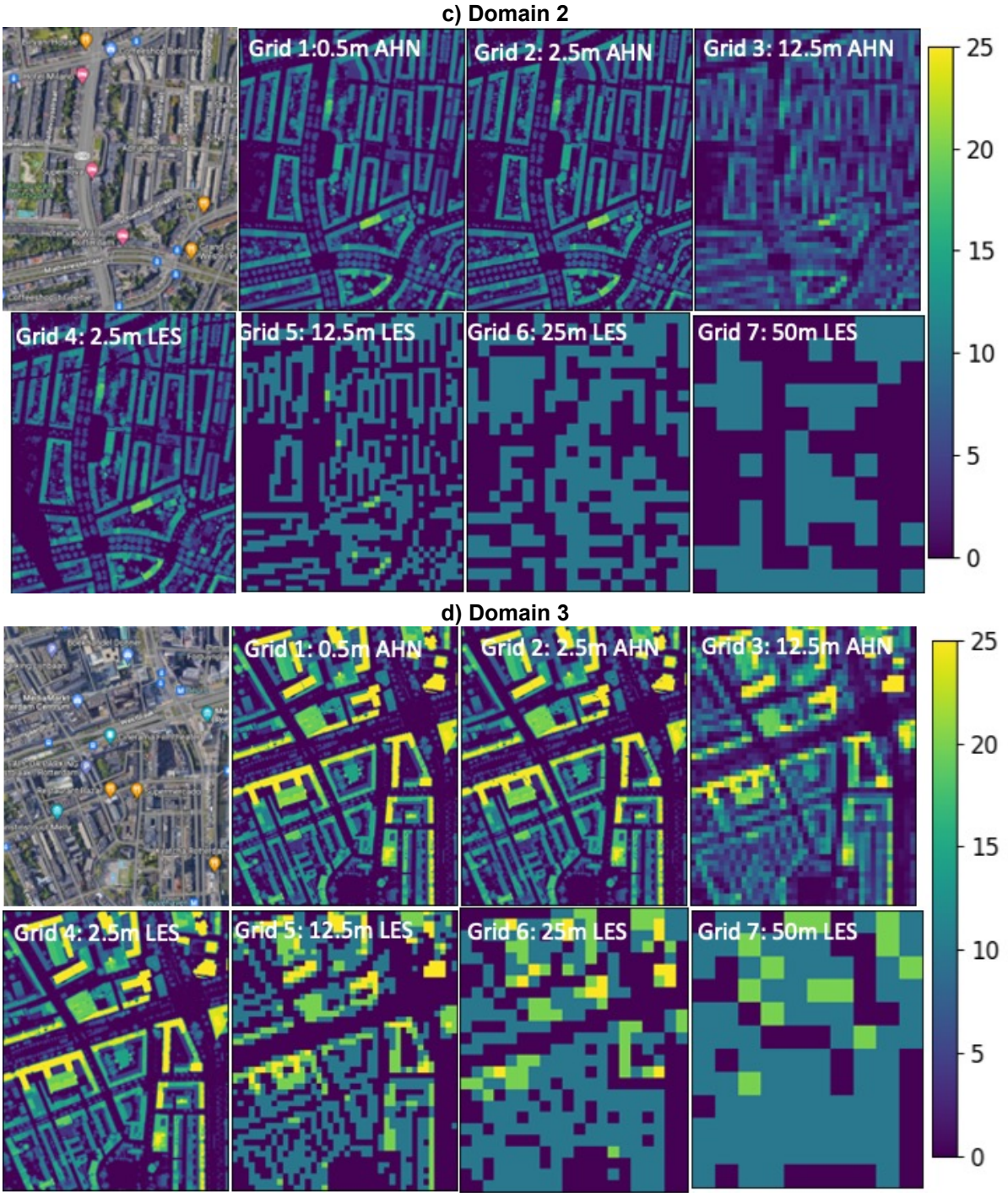


Figure 4.5: a) The three grids shown on the map of Rotterdam, Domain 1 (b) is in a residential area Rotterdam-West, 2 (c) is in the centre near the Nieuwe Binnenweg, and 3 (d) is near Museumplein. For the following three figures, for all 3 domains 7 grids are shown: the first grid is the 0.5m AHN. Grids 2 and 3 are the AHN with resolutions of 2.5 and 12.5m. Grids 4-7 are grids averaged with the method described in section 4.1, where in grid 4 $\Delta x_{LES}$, $\Delta y_{LES}$ and $\Delta z_{LES}$ are all 2.5m. In grid 5 $\Delta x_{LES}$=12.5m, $\Delta y_{LES}$=12.5m and $\Delta z_{LES}$=10m. In grid 6 $\Delta x_{LES}$=25m, $\Delta y_{LES}$=25m and $\Delta z_{LES}$=10m. In grid 7 $\Delta x_{LES}$=50m, $\Delta y_{LES}$=50m and $\Delta z_{LES}$=10m. For all grids the colour bar goes from 0 to 25m.

## 4.2. Sensitivity Analysis of the SVF

The geometry is used to compute the SVF, which determines the absorbed radiation of the surface. Changing the geometry can therefore lead to a difference in the absorbed radiation and can lead to a significant temperature change.

Besides the grid, the SVF algorithm requires several parameters, such as the maximum search radius and angular steps in the horizontal direction, which is called $steps_\beta$. To determine these parameters a sensitivity analysis is performed where the influence of a certain parameter on the SVF can be calculated explicitly, or for a sample of points the parameter is increased in steps and the SVF is computed for each step. To do this for all data points would be computationally expensive and since a sensitivity analysis is not the main goal of this project, this approach is chosen.

### 4.2.1. Grid Resolution

The grid resolution is the most important parameter for calculating the SVF. The KNMI provides a map of SVFs based on the 0.5m raster size AHN of the Netherlands. Dirksen et al. found that at least a 1m resolution is necessary for applications within forests or cities. A larger grid size causes the SVF to be underestimated and flattened out. For example, when using the 5m resolution data, the height gets averaged over a 5m grid, resulting in decreased height differences between different grid points. This causes the SVF to be underestimated, as fewer surrounding points get included in the calculation, and the height difference between the included points is smaller.

We refer back to figures 4.2 and 4.4, which showed a repeating canyon before and after averaging over a 20m. In figure 4.2, the canyon wall was aligned with the grid cell, where in figure 4.4 the canyon wall was not aligned with the grid cell.
After averaging, the height of the canyon is halved and width of the canyon is doubled, resulting in a 4 times lower height-over-width ratio. Calculating the SVF on the 20m resolution grid in the rightmost figure of 4.2 would more than double the SVF, according to the relation between the SVF and height-over-width ratio for an infinite canyon shown in 4.6.

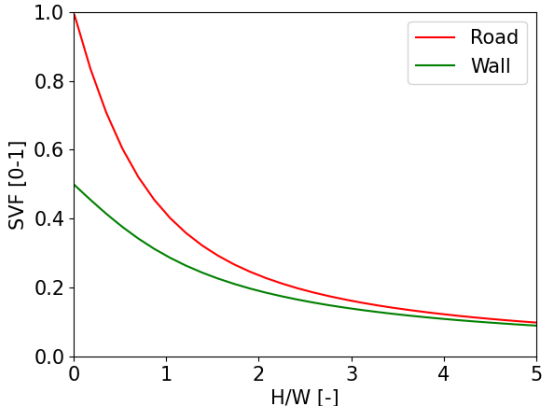


Figure 4.6: SVF for road and wall surfaces for an infinite canyon versus the height-over-width ratio. This figure shows that the SVFs for both road and wall surfaces decreases rapidly with increasing height-over-width ratio.

Figure 4.7 clarifies the effect of the lower grid resolution on the SVF with a 2D example. For multiple locations, the SVF is computed, where a larger angle means a larger SVF. In the left figure of 4.7 the SVF is computed on a 0.5m grid. The 5m grid AHN is computed by averaging the height over the grid cell. The height differences are a lot smaller. This corresponds with the computation in this research of the SVF on the 5m grid size, which has a higher overall average compared to the SVF computed by the KNMI, and the values of neighboring data points show less variation.

However, using a higher grid resolution has a large downside, as computational times and costs increase rapidly. Halving the gridsize quadruples the data-set size (since the data-set is 2D), and more

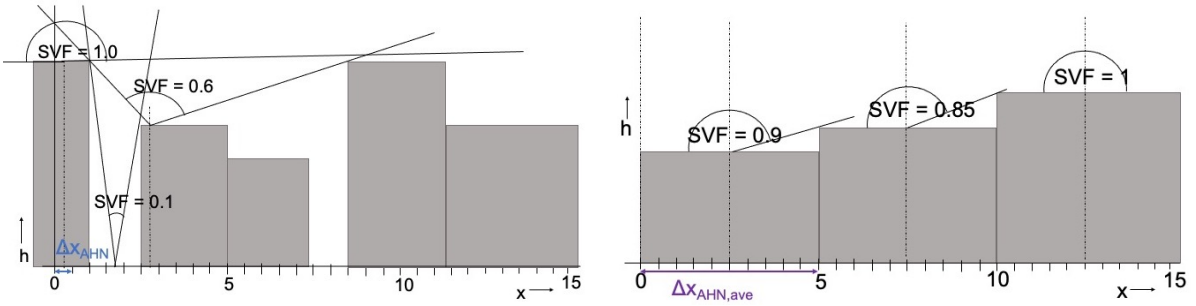


a) SVF on $\Delta x_{AHN}$ = 0.5m b) SVF on $\Delta x_{AHN,ave}$ = 5m

Figure 4.7: a) The SVF is computed for several locations on the 0.5m AHN grid. For three points on the AHN domain the SVF is shown, The SVFs from left to right are 1.0, 0.1 and 0.6. When the SVF would be computed on a larger grid cell of for example 5m, the SVF would be the average of the SVFs on x=0 to x=5m. This would result in a calculation of approximately: 2*1.0 (for the first two grid cells) + 3* 0.1 (for the three grid cells on the ground) + 5*0.6 (for the last 4 grid cells) / 10 = 0.53. b) However, if one first averages the height, the grid shown in figure b would arise. The SVF for the first grid cell of x=0 to x=5m is 0.9 as shown in the figure, which is much larger.

points are included in the SVF calculation due to larger height differences and a larger number of points falling within the maximum radius. Therefore, the maximum radius is tuned to balance computational efficiency and accuracy.

### 4.2.2. Maximum Search Radius

The computation of the SVF involves setting a maximum radius, $R_{max}$, beyond which points are assumed to have a negligible influence on the SVF. In order to choose $R_{max}$, first the influence of a single building on the SVF is computed. Buildings with a width of 20m and a height of 20, 40, 60, and 80m are used to evaluate their explicit effect on the SVF when there is only one building in the area. Figure 4.8a plots the SVF, and figure 4.8b plots the contribution of one building to the SVF, when the distance to the building is increased to 150m. The SVFs for the smaller buildings are larger and increase to 1 faster compared to the taller buildings when increasing the distance to the building.

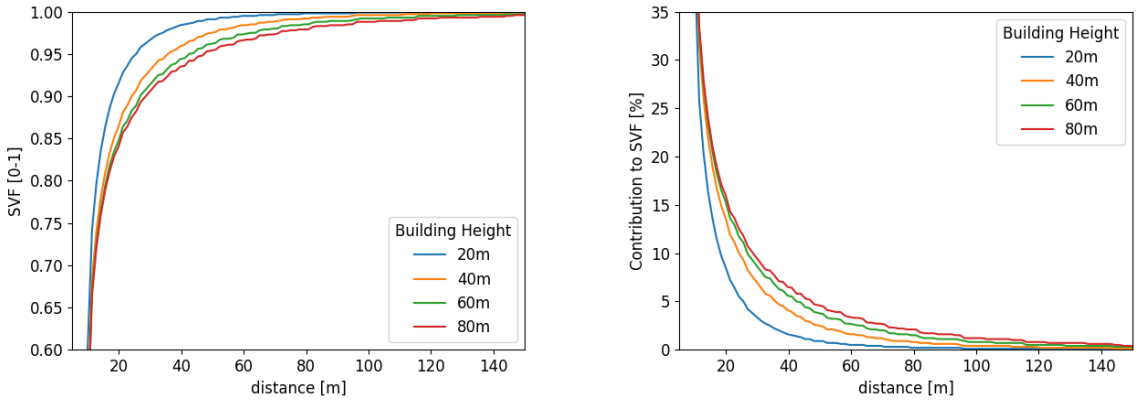


a) SVF b) Contribution of building to SVF

Figure 4.8: In a we see the SVF, and in b we see the contribution of 1 building to the SVF, of a point on an area with 1 building when increasing the distance, for 4 building heights and 20m building width

Figure 4.8 already shows that the influence of a building on the SVF decreases rapidly with distance. However, this does not account for the probability that in an urban context, there may be another building between the observer and the building in question, thereby further decreasing the influence of the building on the SVF with distance. To demonstrate this effect, the change in SVF relative to the maximum range is plotted for three points on the AHN domain, as indicated in Figure 4.9.

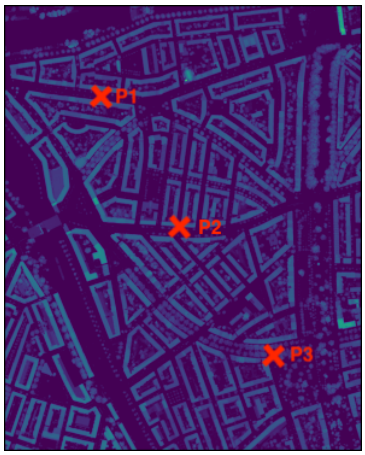


Figure 4.9: Part of the AHN area. 3 points for which the SVF versus the maximum search radius,$R_{max}$, and the steps in horizontal direction, $steps_{\beta}$, have been compared are indicated with a red cross

Figure 4.10a shows that increasing the maximum radius beyond 100 meters has little influence on the SVF. Therefore, SVF simulations are conducted with a maximum search radius of 100m.

### 4.2.3. Steps in the Horizontal Angle

The SVF is calculated by detecting the highest obstruction in every direction, where the directions are discretized by dividing the 360° in a certain amount of steps called $steps_{\beta}$. This amount of steps therefore influences the accuracy of the SVF and another sensitivity analysis is performed on $steps_{\beta}$. $steps_{\beta}$ ranges between 60 and 720 steps, which corresponds to 6° per step to 0.5° per step respectively. The influence is very small in general, and the change does not increase or decrease monotonously due to rounding. From 360 steps the amount of change is within 0.5%, simulations have therefore been proceeded with 360 steps.

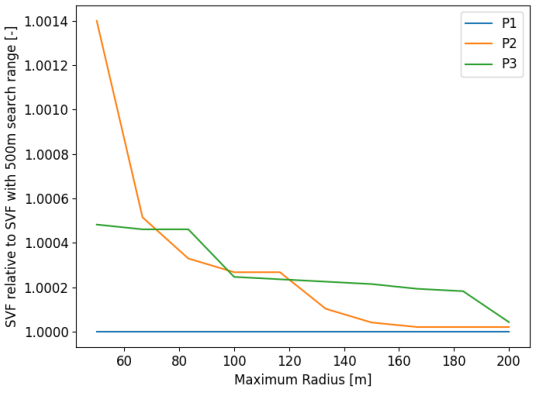


a) Max Radius

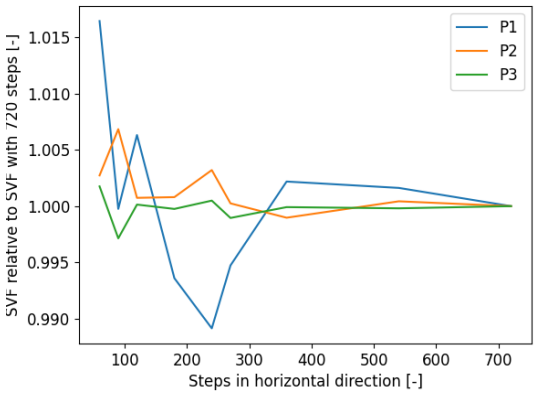


b) $steps_{\beta}$

Figure 4.10: a) SVF relative to SVF with 500m search range for three points indicated in 4.9, where the maximum radius is increased in steps. The relative SVF is calculated as SVF/SVF($R_{max}$=500m), This simulation was done with $steps_{\beta}$=360.
b) SVF relative to SVF with 720 angular horizontal steps for three points indicated in 4.9, where $steps_{\beta}$ is incremented in steps. The relative SVF is calculated as SVF/SVF($steps_{\beta}$=720). This simulation was done with $R_{max}$=100m

## 4.3. Verification of the SVF

### 4.3.1. Infinite Canyon

In order to validate the SVF algorithm, an 'infinite' canyon geometry is created for which analytic SVF solutions, presented in section 3.1.1, exist. These analytic solutions are computed with the SVFs computed by our algorithm. A domain larger than the maximum search radius in length is used and the height and width of the canyon are varied. The SVF for the canyon is computed for every grid cell in the middle strip in the canyon shown in orange in figure 4.11a, and the average SVF of the orange strip is compared to the infinite canyon SVF in eq. 3.6. Although there is a slight overestimation by the algorithm, due to the canyon geometry not being infinite, the SVF is very close to the infinite canyon SVF, as shown in figure 4.11b.

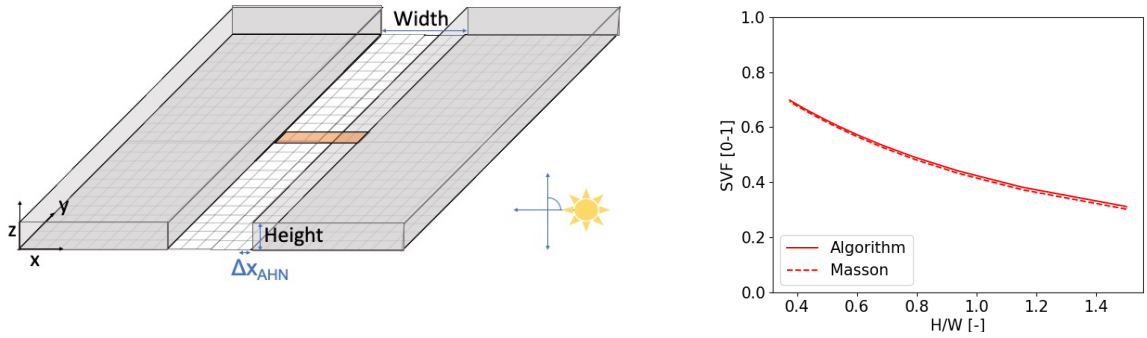


a) Canyon Domain b) Numerical vs Masson

Figure 4.11: a) Schematical, of 'infinite' canyon grid, where the solar azimuth is perpendicular to the canyon direction. The grid cells for which the SVF and SF are computed with the algorithm to compare to the analytical solution are indicated in orange. b) Numerical SVF, calculated with our algorithm, and analytical SVF, according to Masson's equation 3.6, for road surface in infinite canyon

### 4.3.2. KNMI SVF Map

Our calculations were compared with the SVF map provided by KNMI (KNMI - Data Services, 2019). The KNMI uses a SVF algorithm similar to ours, based on Dozier (1990). The difference in approach is that the algorithm used by the KNMI does not iterate over all the obstructions within the maximum radius, but instead chooses a certain amount of angles in the horizontal direction, and calculates the height of the horizon in those directions. The KNMI uses the same maximum range of 100m. The amount of horizontal directions in which the horizon height is calculated, thus determines the accuracy of the SVF, this parameter was set to 16 in the map of the KNMI.

The two SVF maps are compared on domain 1, shown in figure 4.5b. The SVF map of the KNMI is based on the DSM and DTM data of the Netherlands with gridsize $\Delta x_{AHN}$ = 0.5m. To ensure a valid comparison between the values, the SVF was computed using the same grid resolution as the KNMI. This grid is shown on grid 4 (left bottom) of figure 4.5b.

The computed SVF has an average difference of 10% when compared to the KNMI SVF. Besides the use of a different algorithm, several reasons can be pointed out that influence the result, such as the use of AHN2 instead of AHN3, the exclusion of unknown values, and setting of a minimum obstacle height. The AHN2 for Rotterdam was measured in 2008 while AHN3 was measured between 2014 and 2017. Newer buildings are therefore not represented by the KNMI.
Additionally, the KNMI did not filter out below a minimum height, while we chose a minimum height to exclude small or temporary obstacles (e.g., a passing dog), as shown in figure 4.1.
Figure 4.12 shows the maps on domain 1 of the SVF computed by our study and the SVF computed by the KNMI. The KNMI does not provide an SVF value for a substantial amount of the values; 6.2% of all values on domain 1. These are the black spots in figure 4.12 and contribute to the difference in SVF distribution and mean values.

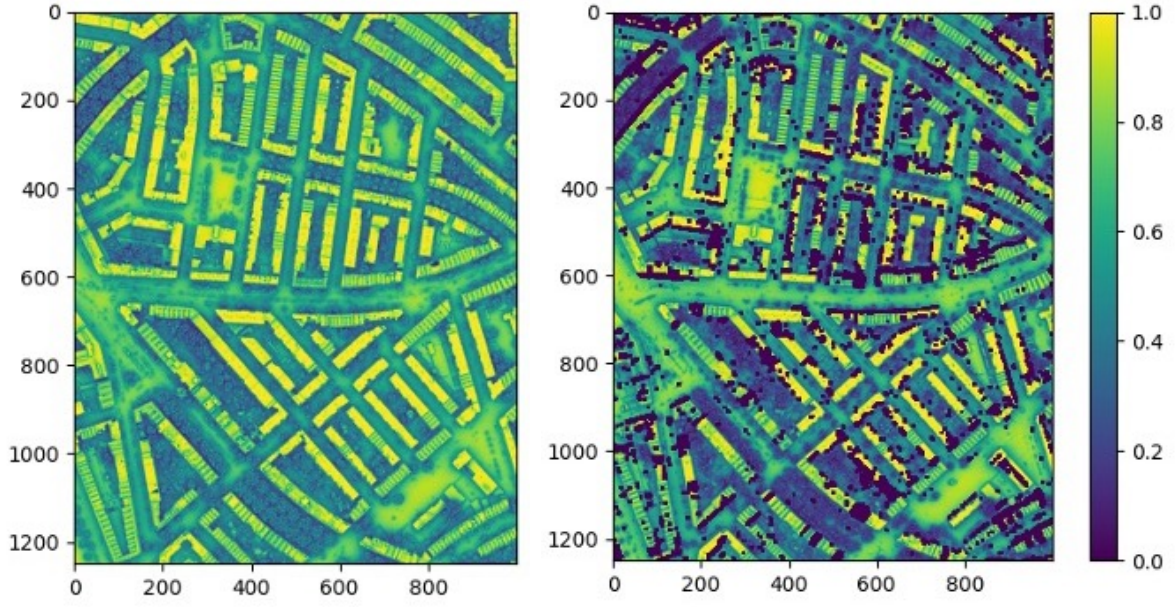


a) Our Algorithm b) KNMI

Figure 4.12: Comparison of the SVF-colourmaps. Figure a shows the SVFs computed by our algorithm and figure b the map of the KNMI. On the KNMI map dark spots are visible, these are data-points for which the KNMI provides no value. The domain consists of 1250 by 1000 data-points, which corresponds to an area of 625 by 500m. The amount of unknown values, shown as dark spots in the KNMI map, for this neighbourhood consists of 6.2% of the data-points, therefore the influence on the average is significant.

### 4.3.3. SVF Distributions

The computed SVFs form a distribution, from which a probability density function (PDF) can be deduced. The PDF is shown in figure 4.13. The same figure show the PDF of the KNMI SVF map. The datapoints for which no SVF value is determined, which are the black dots in figure 4.12, are left out of the distribution. The PDF of SVFs computed with our algorithm and the PDF from the KNMI are close together. The distribution shows a curve with a high peak in the highest column.

When splitting the SVF distribution in two separate distributions for roof surfaces and road surfaces, shown in figure 4.14, the curve can be allocated to the road surfaces while the roof surfaces are responsible for the high peak on the right of the PDF.

The area is a residential neighbourhood with houses of similar height. Because of this low variability in building-height the roof SVF is high for most roof surfaces. With the relation between ground and wall SVFs of eq. 3.9, plotted in figure 4.6, a $SVF_{wall}$ PDF is deduced from the $SVF_{ground}$ PDF, shown in figure 4.15. The city is thus seen as a distribution of infinite canyons with varying height-over-width ratios.

To determine the wall SVF for a grid cell bigger than $\Delta x_{AHN}$, the average SVF for roof and ground surfaces is determined for that cell, and the $SVF_{wall}$ for that cell is then determined from the $SVF_{ground}$. This procedure is clarified in figure 4.16.

To point out the influence grid resolution has on SVF accuracy, PDFs are computed for the same area but where the AHN has a resolution of 2.5m instead of 0.5m, these PDFs are indicated in green in figures 4.13-4.15. Noticeable is that in this case only 21.3% of horizontal surfaces are classified as road surfaces, where this was 43.3% for the 0.5m resolution dataset if the minimum separation height is equal.

As explained in section 4.1, in LES modelling grid cells with fixed dimensions are used, and therefore a different procedure than height averaging is necessary to create an urban surface geometry from

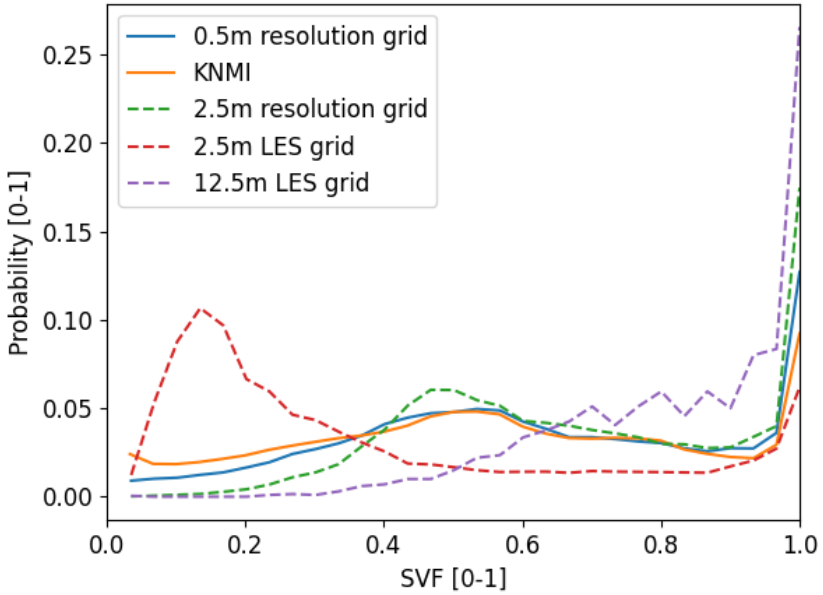


Figure 4.13: PDF for SVFs, on two grid resolutions, for the KNMI, and on 2 grids averaged with LES averaging, all larger grid cell size SVFs are indicated with dashed lines.

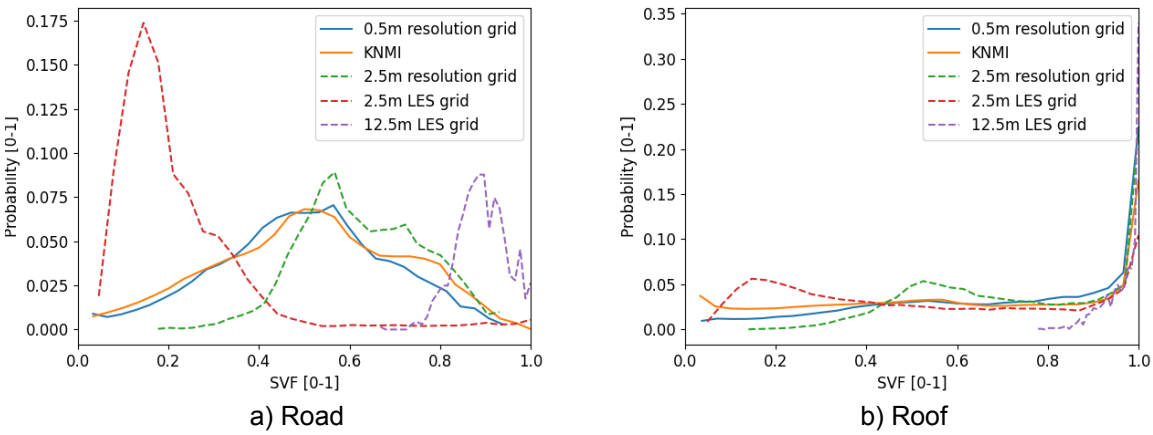


Figure 4.14: PDF for SVF split in ground (a) and roof (b) surfaces, based on the height of the datapoints for which the SVF is computed

the AHN. The SVF can also be computed based on a grid averaged with the method described in section 4.1. These PDFs are indicated in red and purple for two different LES cell sizes in figures 4.13-4.15.

While the SVF on 0.5m grid and the one computed by the KNMI are similarly shaped, the PDF for the other grids show a discrepancy with the 0.5m grid. The PDFs for the two LES grids do not agree with the other PDFs. While for the 2.5m LES size the SVFs are lower compared to the 0.5m AHN grid, for the 12.5m LES the SVF values are much higher.

### 4.3.4. SVF Map

In figure 4.17 the SVF map shows less contrast and the picture is overall lighter for the lower grid resolution map, figure 4.17b. For the SVF computed on the LES averaged grids, 4.17c shows more contrast but is overall much darker, while 4.17d and e are much lighter.

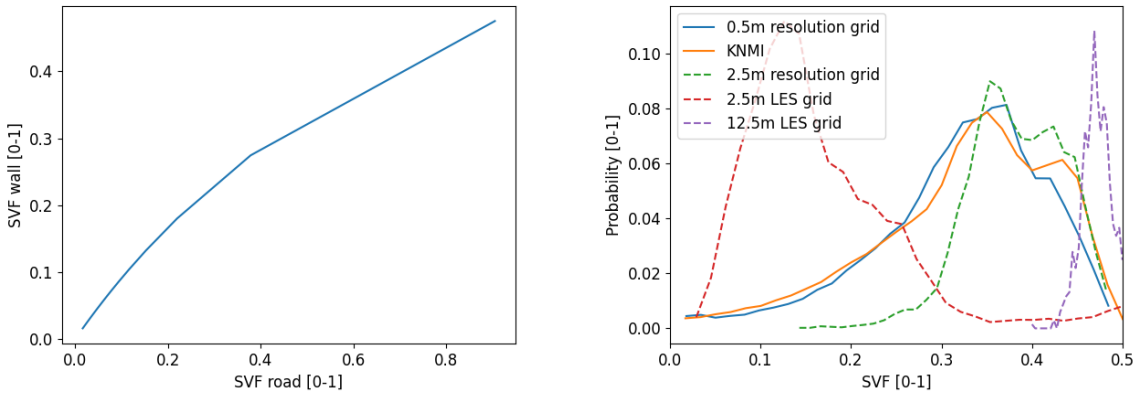


Figure 4.15: PDF for wall surfaces (a), deduced from the relation of wall and road SVFs for infinite canyons (b)

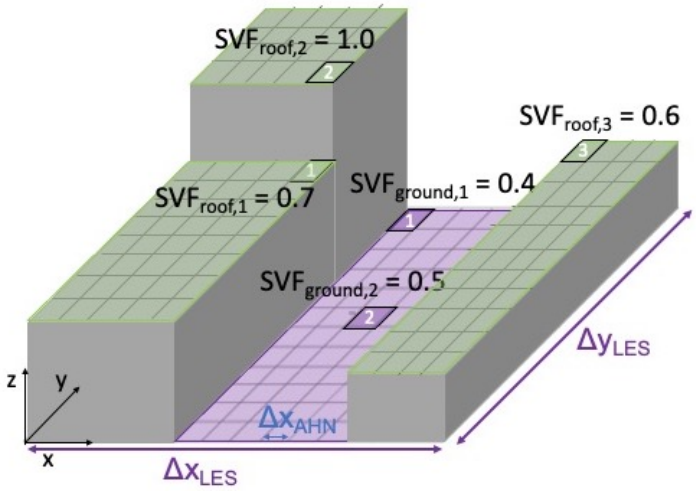


Figure 4.16: The averaging procedure to determine the wall SVF for a grid cell in the SEB model, where the grid cell size is larger than the AHN grid cell size. SVF$_{roof,1}$, SVF$_{roof,2}$ and SVF$_{roof,3}$ are examples of SVFs for AHN grid cells classified as roof surfaces, which are indicated in green, and SVF$_{ground,1}$ and SVF$_{ground,2}$ are examples of SVFs for AHN grid cells classified as ground surfaces, which are indicated in purple. The SVF$_{roof,LES}$ is the average of all SVFs for roof surfaces and the SVF$_{ground,LES}$ is the average of all SVFs for ground surfaces.

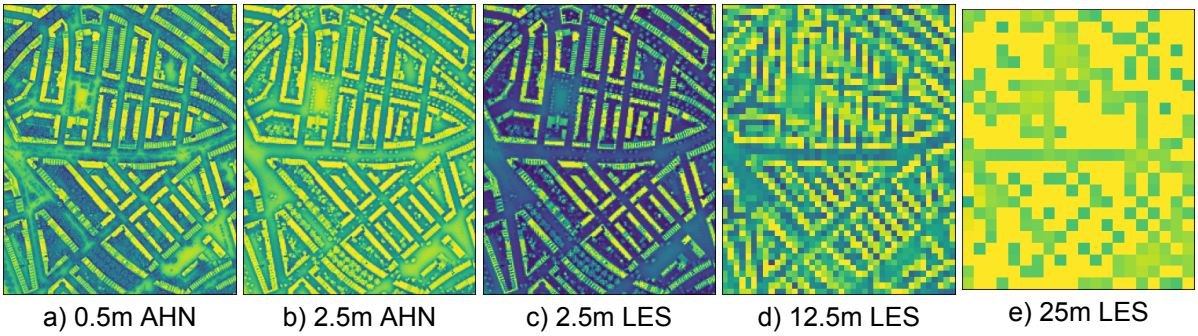


Figure 4.17: Colourmaps of computed SVFs. a) For data over 0.5m resolution AHN b) Over 2.5m resolution AHN. c) LES averaged Δx$_{LES}$, Δy$_{LES}$, Δz$_{LES}$= 2.5m. d) LES averaged grid with Δx$_{LES}$=12.5m, Δy$_{LES}$=12.5m and Δz$_{LES}$=10m. e) LES averaged grid with Δx$_{LES}$=25m, Δy$_{LES}$=25m and Δz$_{LES}$=10m

### 4.3.5. Mean SVF Comparison

For two other neighbourhoods the SVF is computed as well, for which distributions and colour-maps can be found in Appendix B. Figure 4.5b and c show grids of domain 2 and domain 3. Distributions

have similar shapes but due to different building-densities and heights the distributions vary in height and width.

The mean SVFs for all three domains, shown on google maps in 4.5a, for different grid resolutions and for LES averaged grids, are represented in table 4.1.
Domain 1 is the domain shown in figure 4.5b. The grids of domain 1 are the grids used in the results chapter for the surface energy balance simulations.

The surface specific mean SVFs and deduced wall SVFs show that the difference between roof and road SVFs is reduced when data is averaged over larger gridsizes. When using the 0.5m AHN SVF as the baseline, the other SVFs can be over- or underestimated by a factor 1.5, resulting in large differences for absorbed SW and LW radiation.

| | **Dataset 1** | | | | | **Dataset 2** | | | **Dataset 3** | | | | |
|---|---|---|---|---|---|---|---|---|---|---|---|---|---|
| | **AHN Grid resolution** | | | **LES Averaged** | | **AHN Grid resolution** | | | **AHN Grid resolution** | | | **LES Averaged** | |
| | **0.5m** | **2.5m** | **12.5m** | **2.5m** | **12.5m** | **0.5m** | **2.5m** | **12.5m** | **0.5m** | **2.5m** | **12.5m** | **2.5m** | **12.5m** |
| **Average SVF** | 0.60 | 0.7 | 0.94 | 0.38 | 0.67 | 0.61 | 0.73 | 0.95 | 0.56 | 0.64 | 0.87 | 0.31 | 0.56 |
| **Average Roof SVF** | 0.68 | 0.73 | 0.94 | 0.46 | 0.73 | 0.68 | 0.75 | 0.95 | 0.63 | 0.66 | 0.88 | 0.30 | 0.54 |
| **Average Road SVF** | 0.48 | 0.61 | 0.94 | 0.18 | 0.42 | 0.51 | 0.65 | 0.93 | 0.48 | 0.57 | 0.87 | 0.28 | 0.49 |
| **Average Wall SVF** | 0.31 | 0.38 | 0.48 | 0.15 | 0.29 | 0.33 | 0.39 | 0.48 | 0.31 | 0.36 | 0.47 | 0.20 | 0.32 |

Table 4.1: Mean SVF for different surfacetypes, for grid resolutions of 0.5m, 2.5m and 12.5m, and averaged with the LES method over 2.5m and 12.5m LES cell sizes. The different grids for the three domains / datasets can be found in figure 4.5b for domain 1, figure 4.5c for domain 2 and figure 4.5d for domain 3. Dataset 1 is the dataset used in simulations of the results chapter. PDFs and colourmaps of the SVFs on Dataset 2 and 3 can be found in Appendix B.

## 4.4. Verification of The Shadow Casting Algorithm

To verify the shadow casting algorithm the solar position algorithm is compared to data of the solar position for Rotterdam. Next the SF can be compared for an 'infinite' canyon geometry to the analytical solution of Masson. To save computational expenses it is advised to compute the SFs for only one day per week instead of every day. To justify this, solar positions for different days of the week are compared.

### 4.4.1. Solar Position Calculator

To verify the shadow casting algorithm first the solar position calculation should be compared to data. There exists multiple websites that calculate the azimuth and zenith angle for specific locations, where results vary slightly. The azimuth and elevation angle were verified using (Keisan Casio, 2022), and are very close to our calculated values. The solar elevation angle and the solar azimuth angles during daytime, which is defined as the hours between sunrise and sunset, on May 1st, are plotted together with measured angles in figure 4.18.

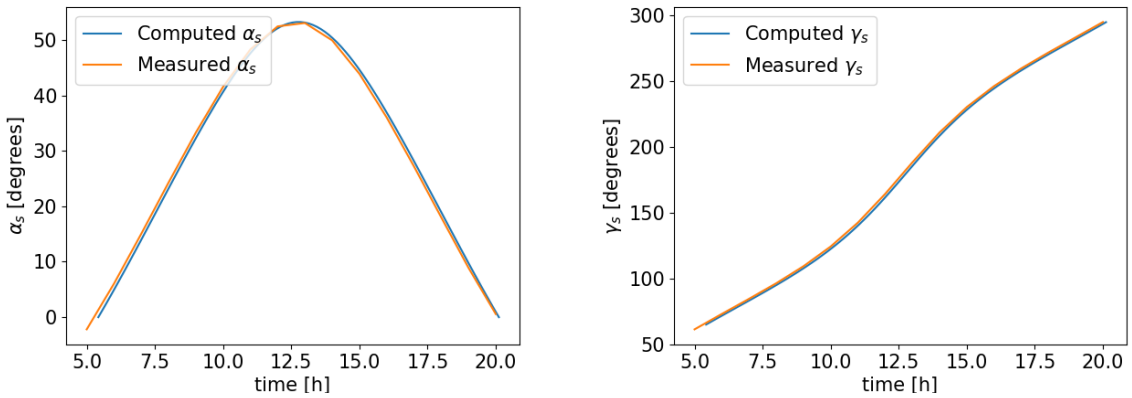


a) Elevation Angle b) Azimuth Angle

Figure 4.18: Elevation (a) and azimuth (b) angle during daytime on May 1st in Rotterdam, calculated values and from (Keisan Casio, 2022)

The variation of azimuth and solar elevation angle throughout the year is the reason that the shadow factor for a point changes throughout the day and from day to day throughout the year. This unfortunately means that this computationally expensive calculation can not just be done once and reused. However, the difference between consecutive days is reasonably small.

In figures 4.19a and b the elevation and azimuth angle is plotted for 7 consecutive days in the start of May. Since the elevation angle and azimuth angle are only defined during daytime, i.e. when the elevation angle is higher than 0, this is plotted only between sunrise and sunset. Figures 4.19c and d shows the difference in angle with day 1.

From the figure 4.19 it is clear that the difference is minimal, within a few degrees in a week. Though one would maybe expect a linearly growing difference this is also not visible from the figures; due to the different complex orbits of the sun and the Earth, which are not completely circular, the differences vary during the day and during the week. In Appendix C the same azimuth and elevation angle comparison can be found for the first week in November, to show that the differences are also very different at different times of the year.

A solution to save computational expenses is to take the middle day of the week and use that for the entire week, or take an average of the hourly solar elevation and azimuth angle for some amount of consecutive days. Taking for example a weekly average results in a 7-fold decrease in computational expenses. A lookup table can then be created that gives the SF for a location, given the time, and day of the year.

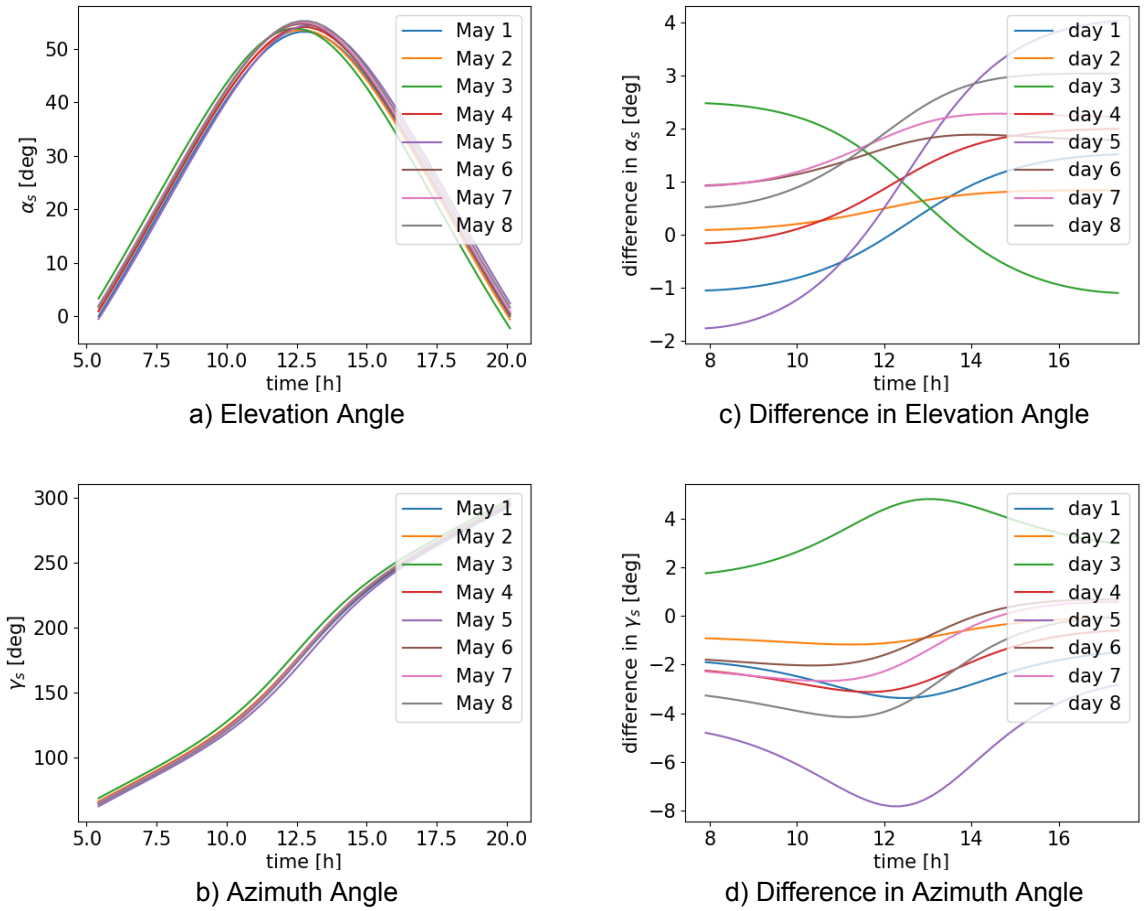


Figure 4.19: On the left we see the elevation angle (a) and azimuth angle (b), during 7 consecutive days in May. On the right we see the difference with day 1 in elevation angle (c) and azimuth angle (d) during the same 7 consecutive days

### 4.4.2. SF Validation for an Infinite Canyon

To validate the algorithm for computing the shadow factor, it is compared to the analytical solution for an infinite canyon. Specifically, the comparison is performed for a scenario where the azimuth is 90$^o$ from North, such that one wall is sunlit and one fully shaded wall. The SF is computed for every grid cell in the middle canyon strip, as depicted in figure 4.11a, and the average is compared to the SF calculated using eqs. 3.25 and 3.27 for the corresponding height-over-width ratio.

If direct sunlight is assumed a collimated lightbeam, the direct sunlight that does not reach the roof and road surfaces must be intercepted by wall surfaces. In this scenario, the SF for wall elements can be determined by using the conservation relation 4.1, proposed by Masson. This relation is used to deduce the SF for walls in the canyon geometry from the SF for roads and the height-over-width ratio.

$$SF_{roof} = SF_{road} + 2\frac{h}{w}SF_{wall} \tag{4.1}$$

The factor 2 in eq. 4.1 accounts for the fact that there are two walls, of which one is fully shaded for an azimuth of 90$^o$ from north. The equations to decribe the SFs for an infinite canyon are described in section 3.2.3 and the algorithm to compute them numerically in section 3.2.2.

The SF for roads (figure 4.20a) and sunlit walls (figure 4.20b) is calculated numerically and com-

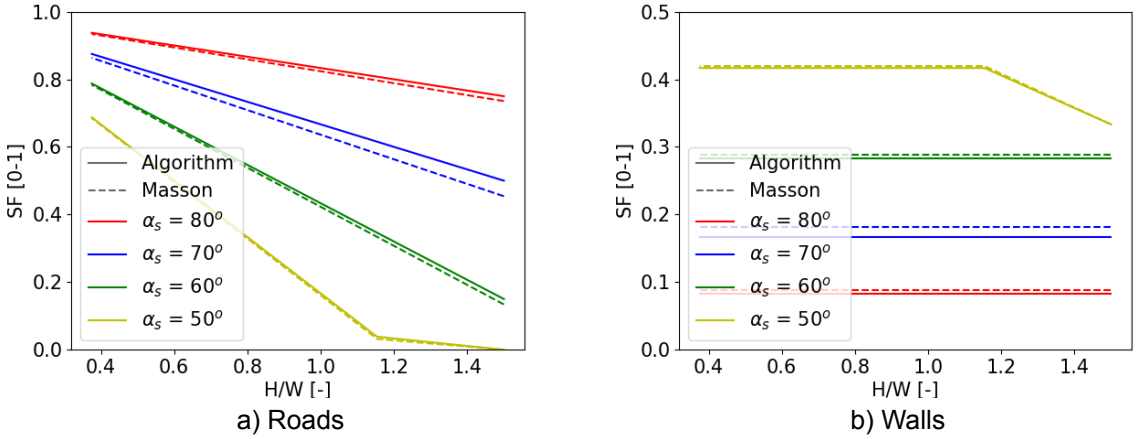


Figure 4.20: The SF versus the height-over-width ratio, for 3 elevation angles, for a road (a) and wall (b) in an infinite canyon. The SFs computed with our algorithm are the solid lines, and the dotted lines are the SFs calculated with Masson's equations

pared to Masson's analytical solutions. The SF is highest for roads at an elevation angle of 75$^o$ when the sun is at its highest, for example during midday in summer. For roads, the SF decreases as the height-over-width ratio increases.

For the highest elevation angle the entire wall is sunlit for all height-over-width ratios and therefore there is no decrease for higher height-over-width ratios. Due to the high angle, the fraction of absorbed direct sunlight, which is normal to the wall, is relatively low. At lower elevation angles, the absorbed fractions are higher because the normal component increases with a larger zenith angle. At an elevation angle of 50$^o$, the wall becomes partially shaded for higher height-over-width ratios.

### 4.4.3. SF Distributions

The SF for every $x_{AHN}, y_{AHN}$ is binary. The shadow is averaged over LES grid cells for roof and ground surfaces separately, resulting in a factor between 0 and 1 for a LES grid cell for both surface types, as shown in figure 4.21.

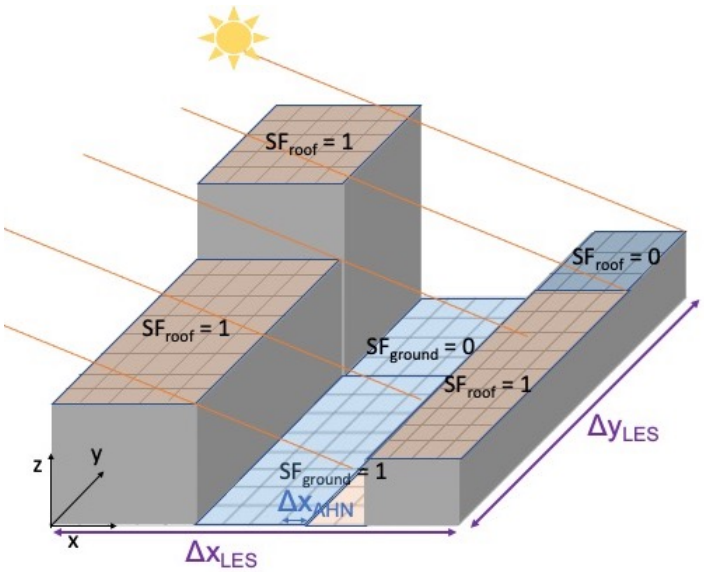


Figure 4.21: In this figure the AHN grid is shown for one LES cell. There is one building blocking the direct sun rays for a part of the other building and part of the ground. The blue grid cells do not receive direct solar radiation, the orange grid cells do. This results in a $SF_{ground,LES}$ and $SF_{roof,LES}$ between 0 and 1. From the $SF_{ground,LES}$ the $SF_{wall,LES}$ is determined

The relation between $SF_{ground}$ and $SF_{wall}$ is not solely determined from the height-over-width ratio, as was the case for the SVF in eq. 3.9, but is time-dependent because of its dependence on zenith angle. In figure 4.22a the $SF_{ground}$ and $SF_{wall}$ are plotted, with solid lines for $SF_{ground}$ and dotted lines for $SF_{wall}$, for different zenith angles.

A Least Squares-fit is used to determine the relationship between the SF for wall and road surfaces for various times, calculated using the equations for an infinite canyon, 3.29 and 3.30. In figure 4.22b, $SF_{wall}$ is plotted with dashed lines against $SF_{ground}$ for different zenith angles. These curves resemble tanh-functions, and thus, the trial fit used is of the form $a \cdot x^b \cdot tanh(cx)$ with fitted parameters a, b, and c. Solid lines in figure 4.22b show the curves plotted using these parameters.

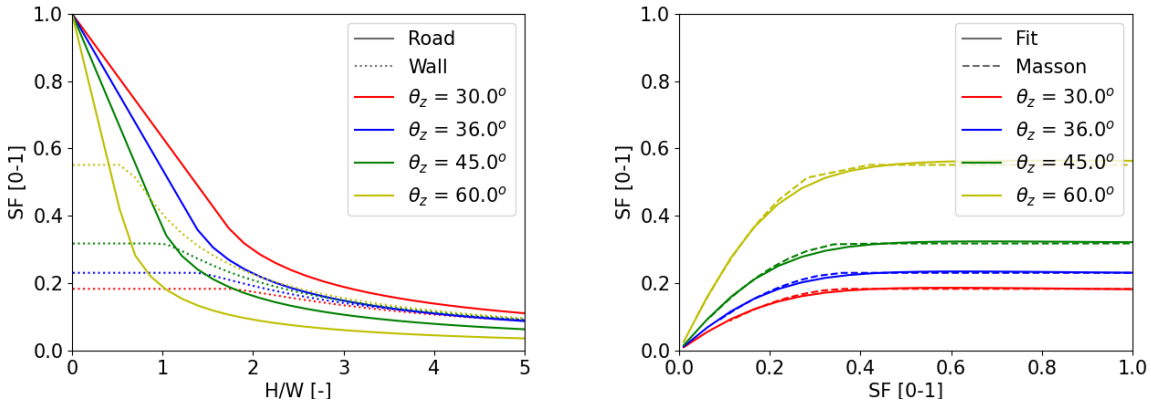


a) SF vs h/w (Masson) b) $SF_{wall}$ vs $SF_{road}$

Figure 4.22: a) $SF_{wall}$ (dotted lines) and $SF_{road}$ (solid lines) in an infinite canyon versus the height-over-width ratio, for different times / Zenith angles, and averaged over all canyon orientations. b) $SF_{wall}$ versus $SF_{road}$ in an infinite canyon, the exact equations of Masson (dashed lines) and the fit used in our model (solid lines)

When $\Delta x_{LES}$ equals $\Delta x_{AHN}$, the SF is binary for the LES cell and the distribution is just a division of 0 and 1's. When the size of $\Delta x_{LES}$ is increased, resulting in averaging over a greater number of cells, the SF grows towards a uniform distribution. Further increasing $\Delta x_{LES}$ results in growing towards one average SF for the entire domain. The $x_{AHN}, y_{AHN}$ coordinates with SF = 0 are not randomly distributed; they tend to be adjacent, given that buildings cast shadows larger than $\Delta x_{AHN}$, and roofs, which are typically unshaded, are larger than $\Delta x_{AHN}$. The distribution of the shadow factors is therefore dependent on the chosen $\Delta x_{LES}$ size.

The distribution of wall SFs depends on the relation between $SF_{ground}$ and $SF_{wall}$ for the zenith angle and the size of $\Delta x_{LES}$. Figure 4.23 shows the distributions of SFs for road, roof, and wall surfaces at three different times, with a grid cell size of $\Delta x_{LES} = 10\Delta x_{AHN}$. In Appendix D the distributions for larger grid ratios can be found to demonstrate the difference in distributions.

In the morning, when the sun is low in the sky, most walls are sunlit, resulting in a relatively high average wall SF. As the day progresses, roof and ground surfaces tend to receive more sunlight, leading to a decrease in the maximum wall SF.

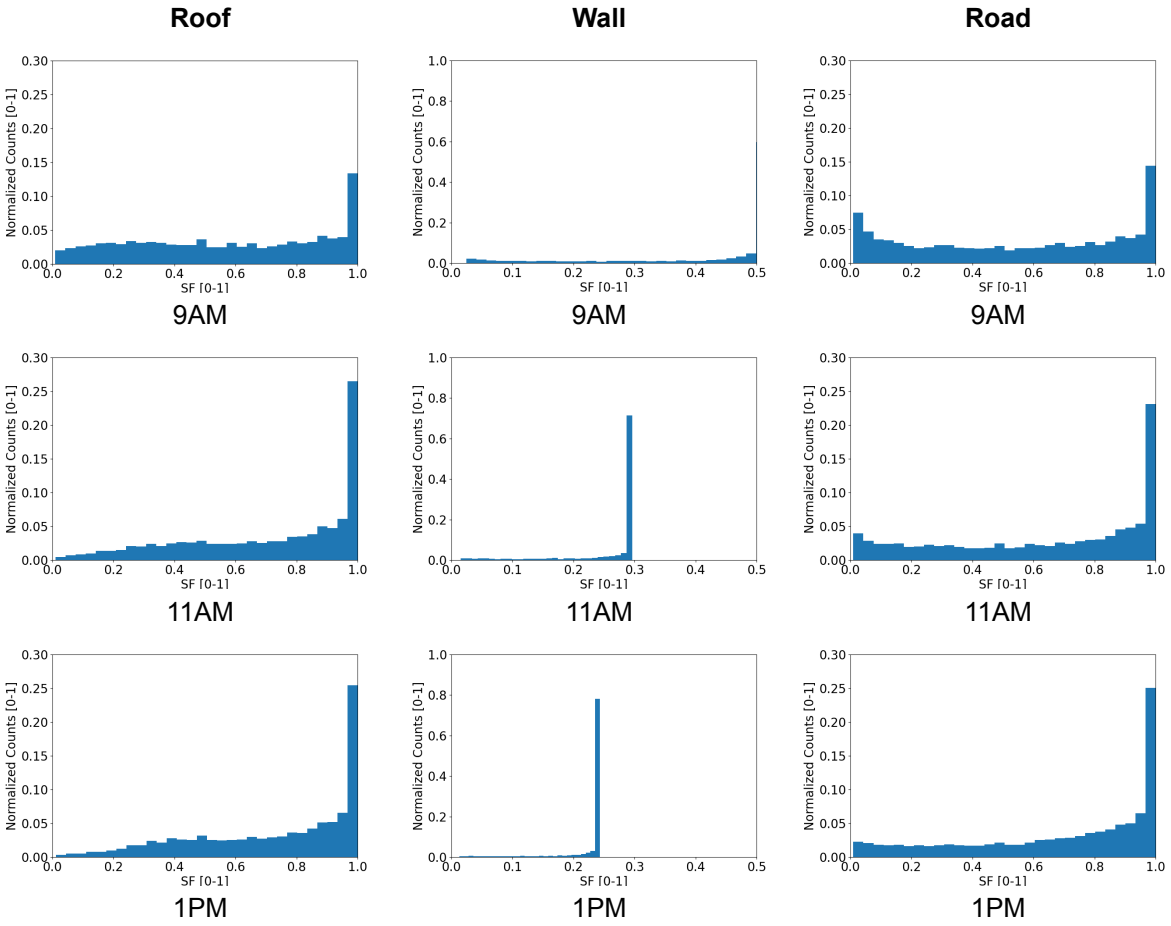


Figure 4.23: SF distributions for roof (left), wall (middle) and road (right) surfaces, at 9AM (top), 11AM (middle) and 1PM (bottom), with a gridsize of 5m

### 4.4.4. Shadow Factor Map

The SF is computed for the first dataset with the algorithm described in section 3.2 with a timestep of 1 hour during daylight, on May 1st. In figure 4.24 the SF is pictured for every hour, showing that the buildings, streets and trees are clearly distinguishable because of their shadows. The only information used is the height of buildings, longitude and latitude of Rotterdam, and the date and time.

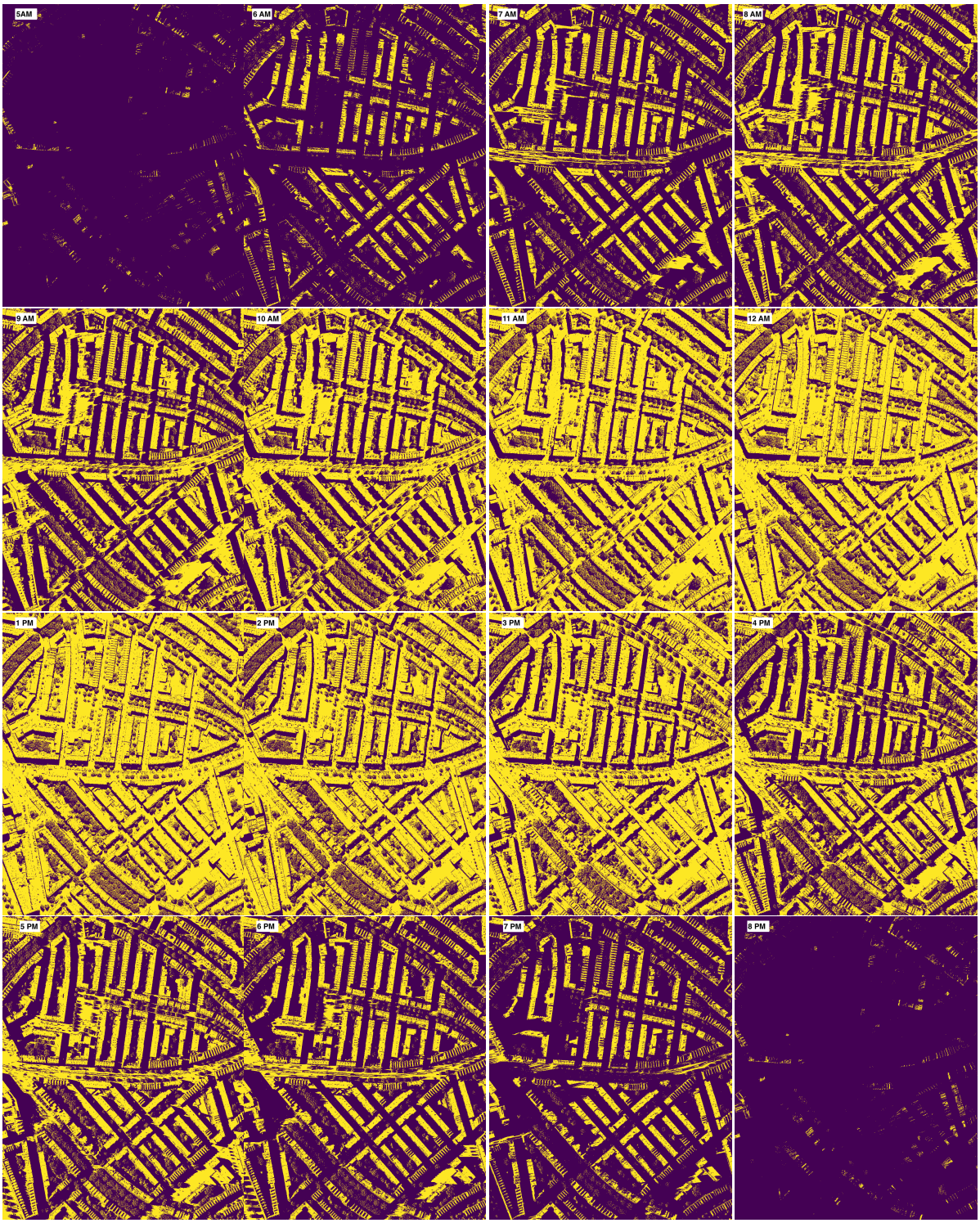


Figure 4.24: SFs for every hour during one day, May 1st 2022

### 4.4.5. SF for LES Averaged Grid

Once again, the SF can be calculated on a grid averaged using the LES method outlined in section 4.1. The mean SF on the domain for different grids differs greatly, which has a significant impact on the absorbed direct SW radiation. As depicted in figure 4.25, when using a grid size of $\Delta x_{LES}$, $\Delta y_{LES}$ and $\Delta z_{LES}$=2.5m, the mean shadow factor is reduced by nearly half. Using a much larger grid size of $\Delta x_{LES}$=12.5m, $\Delta y_{LES}$=12.5m and $\Delta z_{LES}$=10m through the same averaging process, removes nearly all building height variations. Consequently, temporal variation disappears: Surfaces that receive radiation (mostly roofs) do so throughout the entire day, while surfaces that do not receive radiation (mostly ground surfaces) remain unexposed. As shown in figure 4.26, ground surfaces appear black at 12AM due to this lack of radiation.

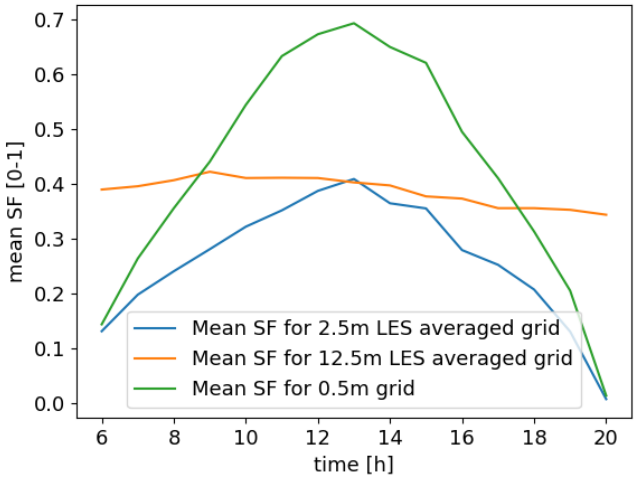


Figure 4.25: Mean SF over domain 1, during May 1st for grid of 0.5m AHN grid, versus LES averaged grid with $\Delta x_{LES}$, $\Delta y_{LES}$ and $\Delta z_{LES}$=2.5m, and LES grid with $\Delta x_{LES}$=12.5m, $\Delta y_{LES}$=12.5m and $\Delta z_{LES}$=10m.

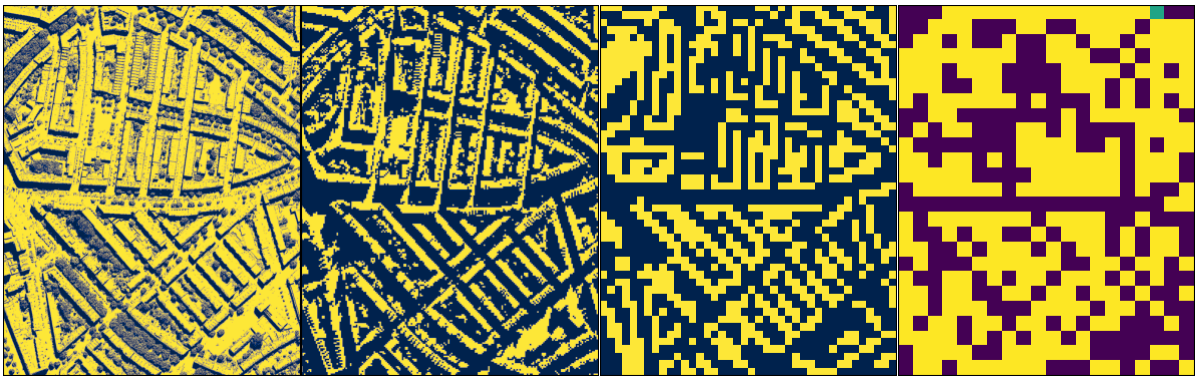


Figure 4.26: The shadow factors at 12AM on domain 1. a) 0.5m AHN grid. b) LES averaged grid with $\Delta x_{LES}$, $\Delta y_{LES}$ and $\Delta z_{LES}$=2.5m. c) LES grid with $\Delta x_{LES}$=12.5m, $\Delta y_{LES}$=12.5m and $\Delta z_{LES}$=10m. d) LES grid with $\Delta x_{LES}$=25m, $\Delta y_{LES}$=25m and $\Delta z_{LES}$=10m

## 4.5. The Three Different Surfaces

The urban surface is divided into three surface types: roof, ground, and wall surface. This allows for different materials and boundary conditions to be set for each surface type, and for temperature evolution to be evaluated separately.

### 4.5.1. Separating Surface Types

The roof area of each cell of size $\Delta x_{LES}\Delta y_{LES}$ is calculated by counting all roof elements, i.e. all AHN points that have a height>0, and multiplying them with the area of one AHN grid cell: $\Delta x^2_{AHN}$. The same is done for the ground elements and water elements.

In the Netherlands there is a lot of inland water, almost 10% of the total land use, which is even higher in the port city of Rotterdam, where it is over 20% (CBS, 2021). Moreover, Heusinkveld et al. (2014), found that large water bodies, such as the Rotterdam' rivers, can significantly influence the urban temperature. In the AHN3 water surfaces are indicated and therefore easily separable from road surfaces, therefore the splitting of ground surface into road and water surface has been included in the model.

The exterior wall surface is calculated by evaluating the height difference between each point and its surrounding points, and the wall surface area for each building is determined by summing up the wall surface on each of its four sides.

$$a_{roof} = \sum^{x,y_{AHN}(h>0)} (\Delta x_{AHN})^2 \tag{4.2}$$

$$a_{ground} = \sum^{x,y_{AHN}(h=0)} (\Delta x_{AHN})^2 \tag{4.3}$$

$$a_{wall} = \sum^{x,y_{AHN}} \sum^{4sides} max(\Delta h, 0) \cdot \Delta x_{AHN} \tag{4.4}$$

From this, the fractions of roof, ground (split into road and water), and wall surface areas can be computed as the area of one surface type divided by the total area of all surfaces, $a_{total} = a_{roof} + a_{wall} + a_{ground}$.

For all ground surfaces, the fraction of water and road surfaces are calculated, and two energy balance equations are solved for different material properties. The ground surface temperature is a weighted average of road and water temperatures, and ground surface fluxes are calculated separately for road and water and added up proportionally to the surface fractions.

$$T_{ground} = \frac{\alpha_{road}}{\alpha_{road} + \alpha_{water}} \cdot T_{road} + \frac{\alpha_{water}}{\alpha_{road} + \alpha_{water}} \cdot T_{water} \tag{4.5}$$

The average surface temperature for the entire urban surface can then be calculated with the surface fractions and temperatures for each surface type with eq. 4.6.

$$T_s = \frac{a_{roof}}{a_{total}} \cdot T_{roof} + \frac{a_{wall}}{a_{total}} \cdot T_{wall} + \frac{a_{ground}}{a_{total}} \cdot T_{ground} \tag{4.6}$$

### 4.5.2. Influence of the Grid on Surface Fractions

The fractions of surface area classified as roof, wall, and ground surfaces are influenced by the grid averaging procedures. To show the influence of the averaging procedures, mean area fractions over domain 1 and 3 are calculated for both the AHN grid and 2 grids averaged with LES averaging. Domain 1 is a residential area with low height-variability, and domain 3 has higher buildings but also more open spaces. Results are summarized in table 4.2.

When using smaller grid sizes, the area fractions are similar to those of the unaveraged grid, but for larger grid sizes, more surfaces are classified as ground surfaces, leading to a decrease in both

| Area Fractions | Gridsize | Roof | Wall | Ground | | |
|---|---|---|---|---|---|---|
| | | | | Total | Water | Road |
| Domain 1 | **0.5m** | 0.408 | 0.212 | 0.380 | 0.043 | 0.337 |
| | **2.5m** | 0.468 | 0.150 | 0.382 | 0.042 | 0.340 |
| | **12.5m** | 0.300 | 0.112 | 0.588 | 0.040 | 0.548 |
| Domain 3 | **0.5m** | 0.357 | 0.217 | 0.426 | 0.043 | 0.383 |
| | **2.5m** | 0.402 | 0.160 | 0.438 | 0.041 | 0.397 |
| | **12.5m** | 0.312 | 0.118 | 0.570 | 0.039 | 0.531 |

Table 4.2: The mean area fractions over domain 1 and domain 3, shown in figures 4.5a and 4.5c, computed for a 0.5m AHN grid, versus LES averaged grid with $\Delta x_{LES}$, $\Delta y_{LES}$ and $\Delta z_{LES}$=2.5m, and LES grid with $\Delta x_{LES}$=12.5m, $\Delta y_{LES}$=12.5m and $\Delta z_{LES}$=10m.

roof and wall area fractions. In dataset 1, which has a high building density with low-rise buildings, the decrease in roof areas and increase in ground areas is greater compared to dataset 3, which has taller buildings (max 132m) but is less densely built.

The grid averaging procedure strongly affects the SVF and the shadow factor, and results in different temperatures for the surfaces of the two grids. Different area fractions will influence the surface average temperatures.

## 4.6. Number of Layers

The surface energy balance equation is solved numerically on our domain by dividing the surfaces into layers as shown in figure 3.1. The top layer experiences all the fluxes of eq. 3.1, and the resulting net heat flux penetrates deeper into the ground through a conduction. The conductive heat flux from one layer to the next depends on layer thickness and the number of layers, and is calculated with eqs. 3.44 and 3.45. The analytical solution exists for a flat ground surface with homogeneous material, and is used to verify the conductive heat fluxes simulated in the model. For this purpose, a sinusoidal temperature forcing at the surface is used instead of a net radiation flux, with a period of 1 day around an average temperature.

The temperature evolution depends on its material properties and the boundary conditions applied to it. Assuming a constant soil thermal diffusivity, uniform soil texture, and a boundary condition of 0 flux out of the last layer, the temperature in the soil is dampened exponentially with depth.

$$T(0,t) = T_{ave,forcing} + T_{amp,forcing} sin(\omega t \Delta_t) \tag{4.7}$$

where $\omega$ is the frequency, converted from hours to seconds

$$\omega = \frac{2\pi}{24} \cdot 3600 \tag{4.8}$$

The dampening depends on the damping coefficient $d$, which is calculated from the volumetric heat capacity $C$[J/m$^3$K], and the heat conductivity $\lambda$[W/mK], which are also used in the layer heat transfer equations in our model.

$$d = \sqrt{\frac{2\lambda}{C\omega}} \tag{4.9}$$

The analytical temperature equation at a depth z, where z is positive downwards, reads:

$$T(z,t) = T_{ave,forcing} + T_{amp,forcing} exp(-z/d) sin(\omega t \Delta_t - z/d) \tag{4.10}$$

Deep into the ground the diurnal variations are flattened out, and even deeper seasonal variations are flattened out as well resulting in a constant temperature throughout the year.

The analytical solution is compared to the numerical solution for different layer thicknesses and amounts of layers, as shown in figure 4.27a. The numerical solution converges to the analytical solution, and the time and accuracy of convergence for different layer thicknesses and amounts of layers can

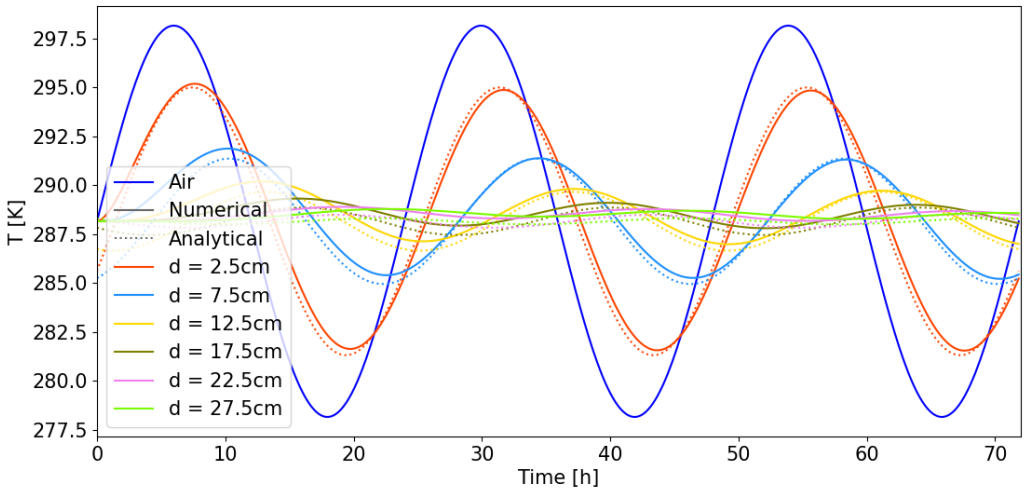


a) Analytical vs Numerical

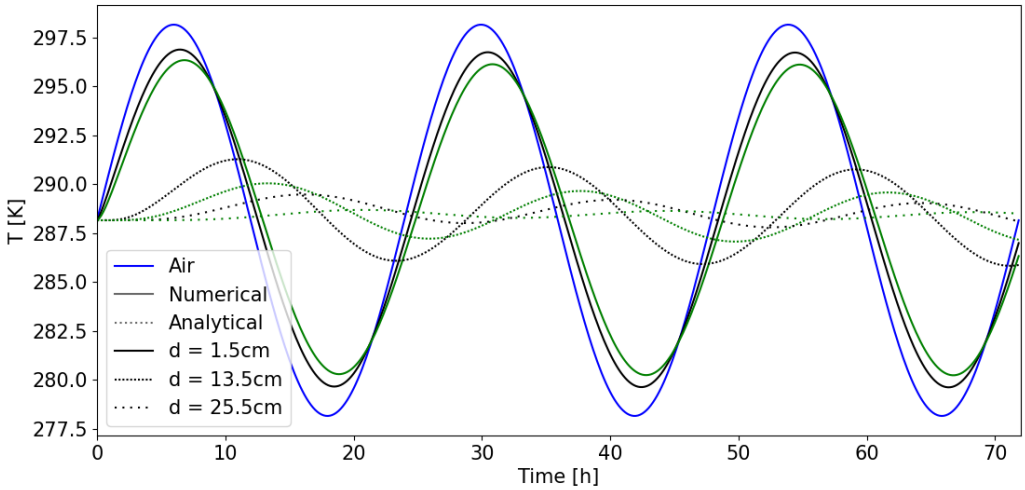


b) Asphalt vs Soil (Numerical)

Figure 4.27: Temperature into the ground at depth d, measured from the top of the surface. A constant thermal diffusivity and uniform texture, and a boundary condition of 0 flux out of the last layer are assumed. The simulation time step is 10 minutes. An air temperature signal is used with a 15 K average and 10 K amplitude.
a) Numerical (solid lines) and analytical (dotted lines) simulation of temperature in 6 layers of soil. The layer thickness is 5cm. This is layer thickness as used in the results chapter.
b) Numerical simulation of temperature in every layer, for soil (green) and asphalt (black) material properties. The layer thickness is 3 cm and the temperature of every 4th layer is plotted. The more densely dotted lines are the lines closer to the surface.

be weighed up against the computational expense.

Figure 4.27b displays a simulation of the temperatures of an asphalt and soil surface using the material properties listed in table 5.1. The simulation solely includes a temperature forcing, thus the net flux consists only of a conductive heat flux.

The influence of artificial materials on heat retention is evident, as the asphalt surface layers shows less variation in surface temperature and retain their heat. These heat-retaining properties of surface materials contribute to the UHI effect.

Once the model has been tested with the simplified geometry and homogeneous material properties,

the layers can be assigned different materials or thicknesses to resemble real-life constructions. For example, roof surfaces can be modeled with a top layer of bitumen followed by wood or concrete, and roads can be simulated as soil with a top layer of asphalt.

### 4.6.1. Material Properties

The net long and short wave radiation is calculated by creating a matrix, equally sized to the SVF and SF matrices, with albedos and emissivities. Different surface types are assigned different materials. The SEB equation is solved for all surfaces on the domain. The matrix approach has the advantage of allowing material types to be altered per grid cell. For example, by coupling the model to a turbulence-resolving model, the effect of replacing conventional rooftops with green rooftops can be investigated at specific locations (Suter et al., 2022).
Various commonly used building materials are used in the simulations to evaluate the influence of different materials, layers, thicknesses, and other parameters on the evolution of surface temperatures over the day.

## 4.7. Boundary Conditions

A boundary condition for the inner temperature is imposed on buildings since the indoor temperature is usually regulated to a comfortable level using heating or cooling systems, and is not allowed to evolve naturally. For ground surfaces, a zero outflow boundary condition is set for the bottom layer. Table 4.3 provides a summary of the initial and boundary conditions used in the simulations.

| | **Initial Conditions** | **Boundary Conditions** |
|---|---|---|
| **Roof** | All Layers: $T_{air}(0)$ | Bottom Layer: $T_{building}$ |
| **Wall** | All Layers: $T_{air}(0)$ | Bottom Layer: $T_{building}$ |
| **Ground** | All Layers: $T_{air}(0)$ | 0 flux out of bottom layer |

Table 4.3: Initial and Boundary Conditions for the three different surfaces

The model allows the building heating temperature to be adjusted as a tunable parameter, and the impact of various heating temperatures on the surface energy balance under different outside temperature scenarios is presented in the results chapter. The impact of building heating temperature on UHI can be examined by setting different inner boundary conditions for buildings and coupling the model to a turbulence model.

## 4.8. Model Forcings

To simulate the surface energy balance, realistic forcing data for downwelling LW and SW radiation fluxes are generated. SW flux data that is measured at cabau for one year is used to generate the SW flux in our model. The SW flux is estimated by fitting the measured SW flux against the Zenith angle over a year, which results in a SW radiation function of the Zenith angle during daytime and zero otherwise. The SW flux data is measured at the ground and therefore the average cloud formation is included in the generated SW flux. The SW radiation is split into direct and diffuse SW radiation, based on the Zenith angle.

$$SW_{dir} = cos(\theta_z) \cdot SW_{down} \tag{4.11}$$

$$SW_{dif} = \left(1 - cos(\theta_z)\right) \cdot SW_{down} \tag{4.12}$$

As for the LW radiation flux, a simple approximation assumes that the air temperature follows a sinusoidal pattern throughout the day, with the peak occurring in the afternoon and the lowest point at night, and the LW radiation evolves accordingly with the air temperature through equation 3.40.

However, in reality temperature and downwelling radiation fluxes are not perfect sinusoidal signals. To account for the surface temperatures' response to rapid changes, a noise signal with a normal distribution and variable standard deviation is added to the temperature and the downwelling SW flux.

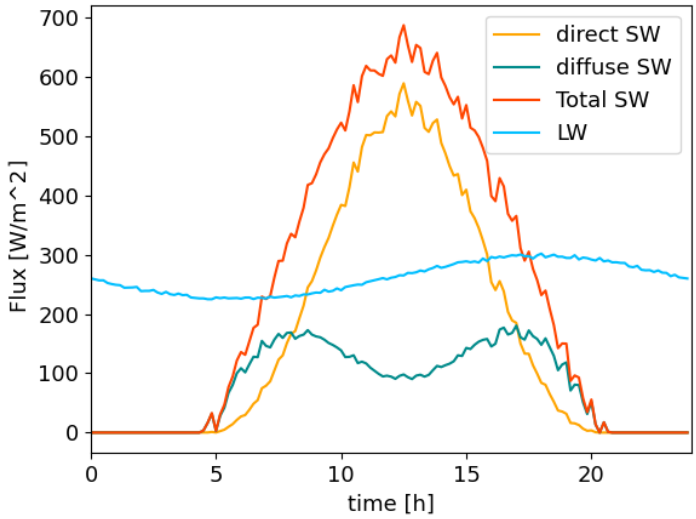


Figure 4.28: Forcings used in the simulations: LW radiation based on air temperature, and SW radiation flux based on data. The SW flux is split into diffuse and direct SW radiation using the zenith angle. The temperature is 288K on average with a 10K amplitude. The standard variation for the temperature and SW radiation noise signals are 0.5 and 20 respectively.

# 5

# Results

The objective of this thesis is to improve the understanding of how various factors affect the temperature behavior of urban surface areas, where a horizontal domain is considered. The focus is on the urban geometry and grid averaging techniques. Other parameters under investigation are the resistance to heat of the surface, and the building temperatures. By analyzing the results of the study, recommendations can be made to improve urban surface energy balance models for building-resolving turbulence models. Simulation parameters are listed in table 5.1.

| | | | | | |
|---|---|---|---|---|---|
| $\Delta t$ | | 10 min | | | |
| $N_{steps}$ | | 288 (2 days) | | | |
| $N_{layers}$ | | 7 | | | |
| d | | 5 cm | | | |
| $R_h$ | | 100 s/m | | | |
| $R_{l,water}$ | | 200 s/m | | | |
| $T_{air,average}$ | | 273.15 + 15 K | | | |
| $T_{air,amplitude}$ | | 5 K | | | |
| $T_{building}$ | | 20 K | | | |
| **Standard Deviation SW** | | 20 W | | | |
| **Standard Deviation Tair** | | 0.5 K | | | |
| **Wall Set up** | | **Walls** | **Roofs** | **Road** | **Water** |
| | **Top Layer** | Brick | Bitumen | Asphalt | Water |
| | **Lower Layers** | Brick | Brick | Soil | Water |
| | | **Albedo** | **Emissivity** | **C** [kJ/m$^3$K] | $\lambda$[W/mK] |
| **Grass** | | 0.3 | 0.88 | 2000 | 1.1 |
| **Soil** | | - | - | 1900 | 0.3 |
| **Brick** | | 0.3 | 0.9 | 2081 | 1.31 |
| **Bitumen** | | 0.12 | 0.97 | 2000 | 0.8 |
| **Asphalt** | | 0.12 | 0.88 | 2251 | 0.75 |
| **Water** | | 0.009 | 0.95 | 4200 | 0.598 |

Table 5.1: Simulation Parameters

## 5.1. Comparison of Two Geometries

The surface fluxes are influenced by the sky view factor and shadow factor, which are determined by the surface geometry. The temperature and fluxes are computed for two grids: The first grid is the 0.5m AHN grid, a colourmap of this grid is shown in grid 1 of figure 4.5b. This grid is most detailed and closest to actual geometry, and SVFs computed on this grid are therefore assumed to be the most realistic.

The second grid is the 2.5m LES grid, which is a grid averaged with the method described in figure 4.3 from the 0.5m AHN grid, where $\Delta x_{LES}$, $\Delta y_{LES}$ and $\Delta z_{LES}$ are all 2.5m. This grid is indicated with dashed lines in all figures and a colourmap of the grid is shown in the 4th grid of figure 4.5b.

### 5.1.1. SVF and SF Differences

Table 4.1 presents the mean SVF values, which indicate an underestimation on the second grid, which is the 2.5m LES grid or grid 4 in figure 4.5b, with a mean SVF of 0.38 compared to 0.6 on the 0.5m grid. For ground surfaces the decrease is relatively the largest, with 0.18 versus 0.48. The roof SVF has a decrease of 0.46 versus 0.68 and the wall SVF has a decrease of 0.15 versus 0.31.

The SF varies throughout the day and is computed with the zenith and azimuth angle for every hour of May 1st, shown in figure 4.24 for the 0.5m grid. Figure 4.25 illustrates the significant differences in SFs, where the mean SF value throughout the day is underestimated for the 2.5m LES grid compared to the 0.5m AHN grid. The latter has a maximum mean SF value of 0.69, while the former has a maximum mean SF value of 0.41.

The influence of the grid on the different components of the surface energy balance is studied, by evaluating surface fluxes and temperatures for the roof, wall and ground surfaces for both grids. The fluxes and temperatures plotted are the averages, as explained in chapter 4, over domain 1.

### 5.1.2. SEB Differences

The net LW and SW radiation are directly affected by the geometry. The difference in SW and LW reflections between the roof, wall, and ground surfaces of the grids is explored in section 5.2. A difference in net LW and SW fluxes affects the net radiation and causes the surface temperatures to evolve differently throughout the day for the two grids, which is discussed in section 5.3. The surface temperature forms the boundary condition for the sensible heat flux, which is investigated in section 5.4. The results depend on the temperature boundary conditions prescribed for roof and wall surfaces, and forcing used in the simulations. The impact of outside weather conditions and indoor building temperature is discussed in the final section 5.5 of the Results chapter.

Appendix E provides a comparison of the LW and SW fluxes for a grid averaged with the same method but a much larger grid cell of $\Delta x_{LES}$=12.5m, $\Delta y_{LES}$=12.5m and $\Delta z_{LES}$=10m. This grid is shown in grid 5 of figure 4.5b.

## 5.2. LW and SW Budget Components

SIn this section we specifically explore the different LW and SW budget components, where the absorbed SW radiation from the sky is split into direct and diffuse parts, determined by the SF and SVF, respectively. The fraction of received radiation that is reflected or emitted by other surfaces depends on the geometry and is captured by view factors. The reflection terms become smaller with each reflection, and in this study, only first-order reflections are considered. The first-order reflections are represented by incorporating the view factors and material properties of the other surfaces, as the different terms in the net LW eqs. 3.37-3.39 and net SW eqs. 3.33-3.35. The reflection from roof to wall surfaces is neglected.

Each component of the net SW and LW radiation is shown in figure 5.1, with the LES-averaged grid plotted with dashed lines and the AHN-grid with solid lines. The surfaces of the LES-averaged grid, having smaller SVFs, absorb less heat during the day. Note that the axes for the plots for the different surfaces are scaled differently, to make the difference in absorbed flux between the two grids visible.

### 5.2.1. Shortwave Radiation

The difference in absorbed flux between the two grids is most visible for SW radiation, since the SW flux received from the sky is much larger than the LW flux received from the sky.
The net SW radiation is shown in red in the right column of 5.1, and peak values occur at midday for all three surfaces. For ground surfaces the difference in net absorbed SW radiation is the greatest because the $SVF_{ground}$ differs relatively most for the two grids, with peak values around midday of 373 $W/m^2$ for the 0.5m grid and only 121 $W/m^2$ for the 2.5m grid, a factor 3 difference. For roof surfaces the maximum net SW values are 465 $W/m^2$ versus 348 $W/m^2$, and for wall surfaces the maximum net SW are 138 $W/m^2$ versus 71 $W/m^2$ for the 0.5m and 2.5m grid respectively.

### 5.2.2. Longwave Radiation

The peak of grey body emission, indicated in lightgreen in the left column of figure 5.1, occurs in the afternoon for all surfaces due to the highest surface temperature at that time. All three surfaces emit less LW radiation for the 2.5m LES-grid because of the smaller SVFs. The largest difference in emitted LW radiation is for ground surfaces. The mean difference is 10 $W/m^2$ for ground surfaces, and 3 $W/m^2$ for both wall and roof surfaces.
Notice that for all three surfaces, the absorbed LW flux reflected from wall surfaces, represented by the pink lines in the left column of figure 5.1, is much larger for the 2.5m LES-grid, compared to the 0.5m AHN grid. This means that the 2.5m grid predicts a larger LW trapping effect, whereas the 0.5m AHN grid predicts a larger contribution from the sky.
This difference in reflected flux is caused by the fact that the WVF is calculated as WVF=(1-SVF), which follows from the fact that all view factors must add up to one. The SVF is smaller for the 2.5m grid, therefore the WVF is larger. For wall surfaces the GVF is assumed equal to the SVF, and the WVF is therefore (1-2 SVF). For wall surfaces, the effect of increased LW trapping is therefor greatest, with a mean difference of 101 $W/m^2$ between the two grids for LW reflected from wall surfaces to wall surfaces, compared to 58 $W/m^2$ for roof surfaces and 84 $W/m^2$ for ground surfaces.

For all three surfaces, the net LW radiation, indicated in red in the left column of figure 5.1, is negative, meaning it is emitted, and highest for the 0.5m AHN grid. The use of the 2.5m LES grid in simulations would result in smaller emitted LW fluxes and the retention of more heat during the night, with smaller differences between day and nighttime temperatures. This decline in temporal variation is largest for ground surfaces, where the 0.5m AHN grid has a minimum and maximum value of -99 $W/m^2$ and -61 $W/m^2$ of net emitted LW radiation, while the 2.5m LES grid has a minimum and maximum value of -51 $W/m^2$ and -40 $W/m^2$ of net LW radiation; a 38 $W/m^2$ versus 11 $W/m^2$ difference between minimum and maximum net LW. The peak net LW radiation is emitted at midday for both roof and ground surfaces, while for wall surfaces, the net LW emission is more constant throughout the day and lowest at midday due to the LW trapping effect from road and other wall surfaces.

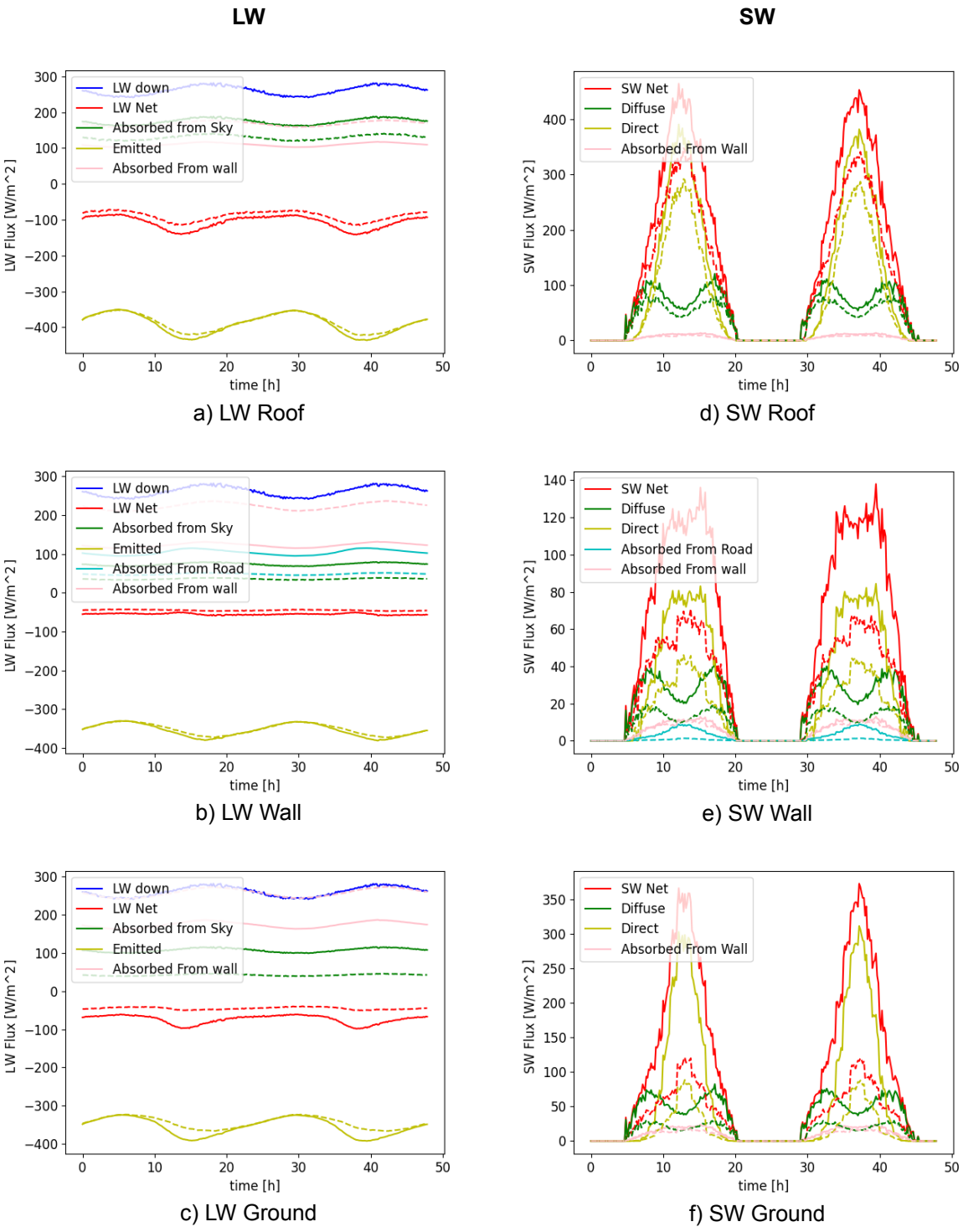


Figure 5.1: The net LW (left, a-c) and SW (right, d-f) radiation of roof (top), wall (middle) and ground (bottom) surfaces, split into the different components, where solid lines are for the 0.5m grid and dashed lines for the 2.5m LES grid

## 5.3. Surface Temperature Evolution

The net surface radiation comprises the net LW and SW fluxes, and the net radiation dictates the temperature changes of surfaces. Figure 5.2 illustrates the impact of SW and LW reflections on surface temperature. The albedos for all three surfaces are either those in table 5.1 or 0, so no SW reflections occur, and the emissivities are either those in table 5.1 or 1, so no LW reflections occur. The SEB is simulated for both grids, and is compared to air temperature as a reference, where the SW and LW reflections are either incorporated or omitted, to demonstrate their influence on the surface temperature.

### 5.3.1. Including versus Excluding all Reflections

The figures 5.2a-c show the temperatures for two situations: one without any reflections, indicated in orange, and one including both SW and LW reflections, indicated in green. The dashed lines are again for the 2.5m LES grid and the solid lines are for the 0.5m AHN grid. A surface with an emissivity of 1 absorbs more LW radiation from the sky but emits perfectly as a blackbody, while a surface with an albedo of 0 absorbs more SW radiation from the sun and the sky, thus warming up more during the day.

Excluding reflections results in higher temperatures for both grids. This difference is however smaller for ground surfaces compared to roof surfaces. This occurs because when reflections are excluded, all radiation received from the sky is absorbed, but no radiation is reflected from other surfaces. For ground and wall surfaces, reflected fluxes constitute a larger fraction of the net radiation than for roof surfaces, where radiation from the sky is the most significant.

The difference in peak temperature between excluding and including both SW and LW reflections is 1.8 K for the 0.5m AHN grid and 1.7 K for the 2.5m LES grid for roof surfaces (figure 5.2a). For wall surfaces (figure 5.2b), the differences are 1.6 and 1.5 K for the 0.5m AHN and 2.5m grids, respectively. For ground surfaces (figure 5.2c), the differences are 1.0 and 1.1 K for the 0.5m AHN and 2.5m grids, respectively. For all three surfaces, the temperature difference between including and excluding reflections is similar for both grids, indicating that the difference in absorbed SW and LW radiation from the sky is the primary cause of the temperature difference between the two grids, rather than reflections.

### 5.3.2. Including Shortwave or Longwave Reflections

The figures 5.2d-f are used to assess whether excluding SW reflections, indicated with purple lines, or excluding LW reflections, indicated with yellow lines, has a greater impact on temperature rise. Excluding SW reflections but including LW reflections results in a greater temperature rise, especially during the daytime due to the significant difference in absorbed SW radiation, indicated in figures 5.1d-f. During the night, the temperature difference decreases as the LES averaged grid has lower SVFs, resulting in smaller emitted LW fluxes.

### 5.3.3. Main Take-Away

For the 2.5m grid, the peak temperatures are considerably lower; the averaging method results in an underestimation of the surface temperature during the daytime. The largest temperature difference between the two grids, when both SW and LW reflections are included, occurs for ground surfaces, with a maximum temperature difference of 5.84 K (figure 5.2c). For roof surfaces, the maximum temperature difference is 2.58 K (figure 5.2a), and for wall surfaces, it is 2 K (figure 5.2b).

However, this outcome depends on the weather situation and selected boundary conditions. By increasing the building temperature, the emitted LW radiation by roof and wall surfaces rises, and the relative contribution of the SW and LW fluxes changes. In Section 5.5, the impact of the boundary condition $T_{building}$ on the surface temperatures is examined for various weather conditions.

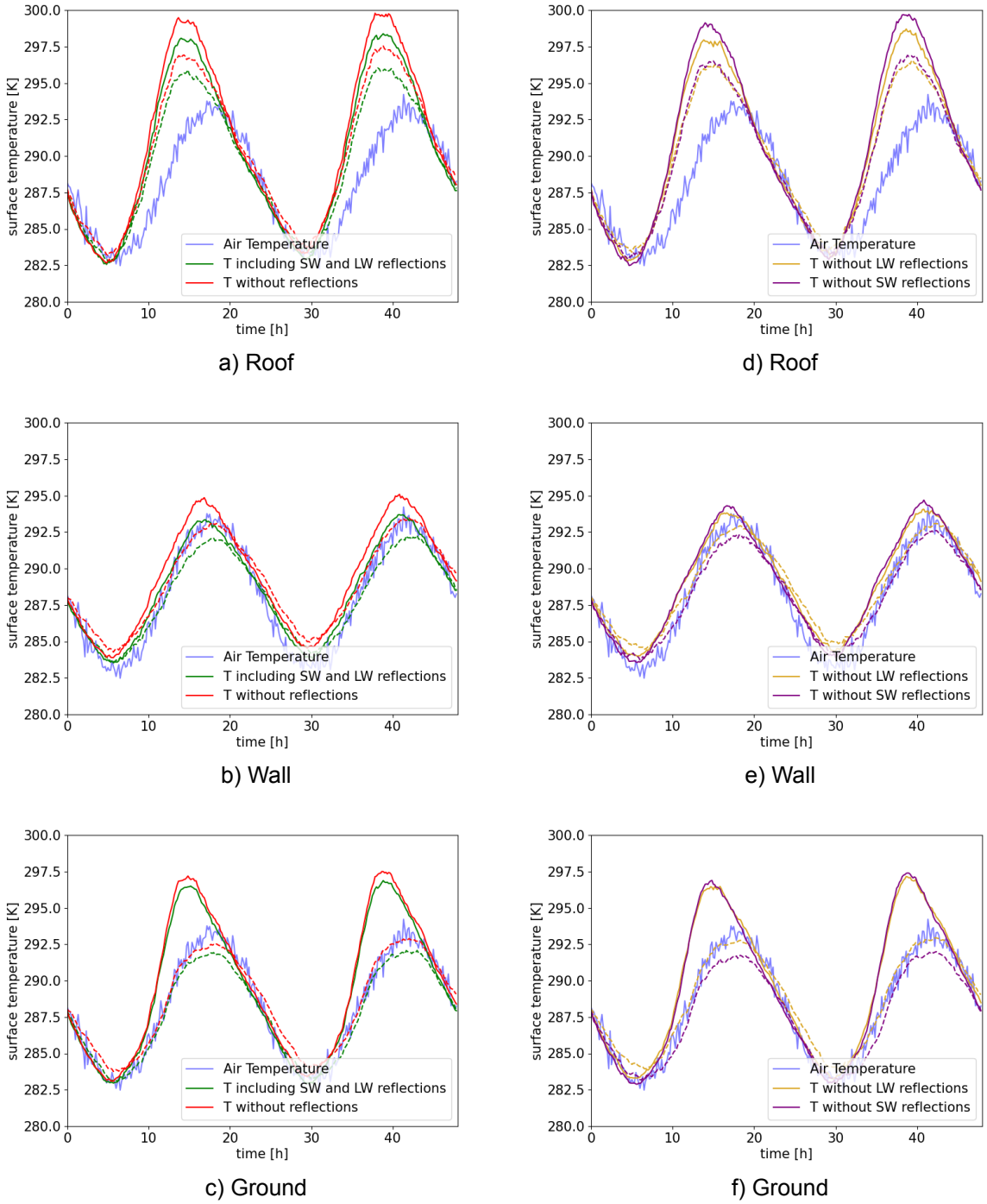


Figure 5.2: The roof (top), wall (middle) and ground (bottom) surface temperatures for 0.5m AHN (solid lines) and LES averaged grid (dashed lines), with the air temperature for reference, for all versus no reflections on the left (a-c), and for only SW or only LW reflections on the right (d-f).

## 5.4. Sensible Heat Fluxes

The sensible heat fluxes are proportional to the temperature difference between the surface and the air. The LW and SW flux differences caused by the different geometries, influence the surface temperatures, which in turn form the boundary conditions for the sensible heat fluxes. The building materials are assumed impermeable to water and therefore no latent heat fluxes are taken into account in the model except at the water surfaces. For water surfaces the aerodynamic resistance to moisture $R_l$ is assumed constant.

The aerodynamic resistances to heat, $R_h$, needed to calculate the SHF fluxes, depends on many parameters unknown in our model. In the simulations, $R_h$ is held constant, but in reality, it is geometry-dependent and would differ between the two grids. The impact of the SHF on the Surface Energy Balance (SEB) is evaluated by varying the unknown $R_h$ and assessing the resulting surface temperature for both grids.

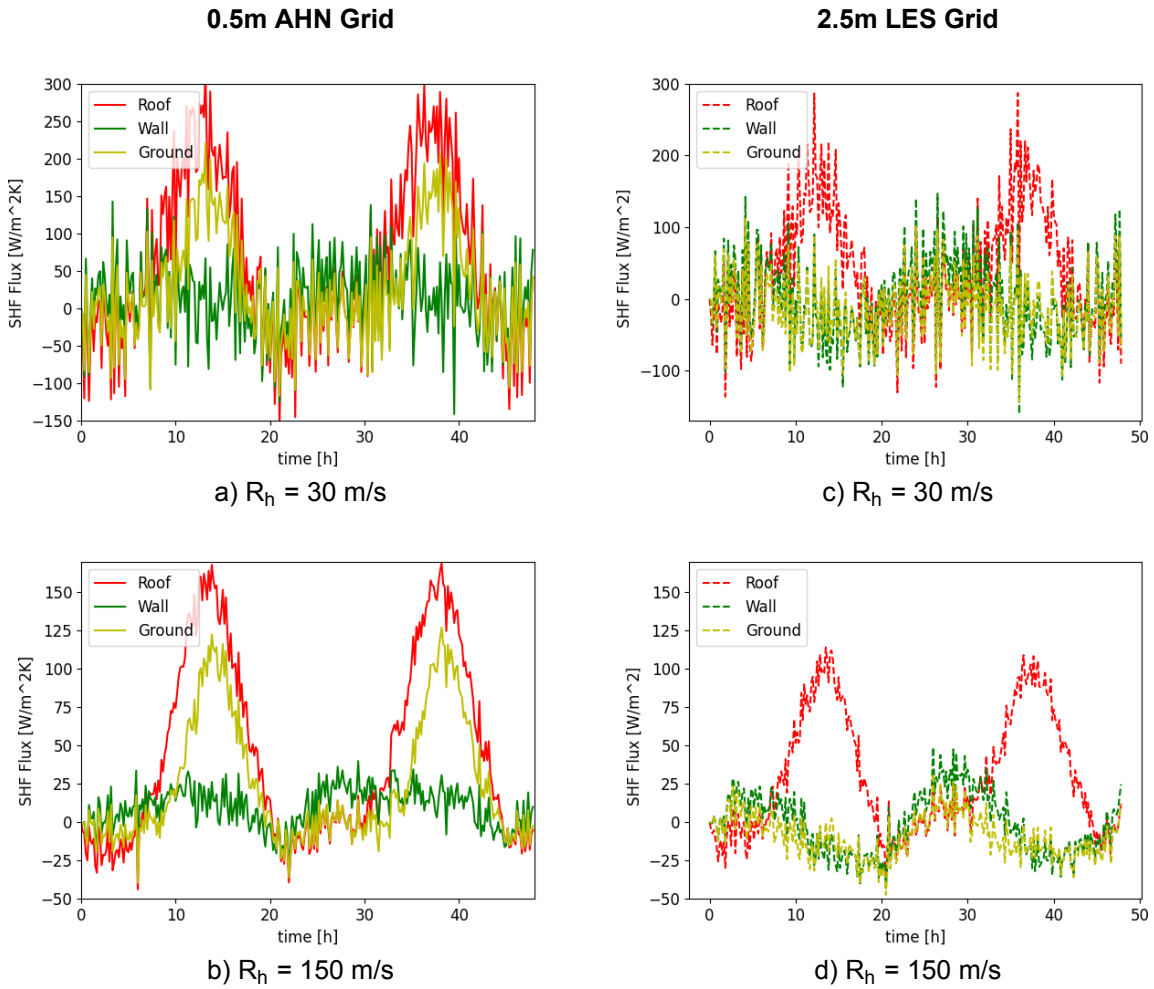


Figure 5.3: The SHF fluxes for the three surfaces for an Aerodynamic Resistance of 30 s/m (top) and 150 m/s (bottom), for the 0.5m AHN grid (left), and for the 2.5m LES grid (right)

### 5.4.1. Comparison of the Aerodynamic Resistances for Both Grids

The magnitude of the SHF is inversely proportional to $R_h$, and a higher $R_h$ results in a greater difference between surface and air temperature. Additionally, high $R_h$ values make the heat fluxes less sensitive to small and rapid changes in air temperature: When $R_h$ is increased from 30 s/m to 150 s/m, the variations in all SHFs decrease considerably, as demonstrated in figures 5.20-5.22 for the 0.5m grid.

Roof surfaces receive the most LW and SW radiation during the day, leading to the largest temperature differences between the surface and air, as seen in figure 5.2a. As a result, the difference between the day and night SHF are greatest for roof surfaces, for both grids, visible from the red lines in figure 5.3.

For roof surfaces the mean difference between $R_h$ of 150 s/m (bottom left) and 30 s/m (top left) for the 0.5m grid roof surfaces is 44 $W/m^2$, resulting in a 0.9 K temperature difference. For the 2.5m grid the mean difference between the $R_h$ of 150 s/m (bottom right) and 30 s/m (top right) for roof surfaces is 36 $W/m^2$, resulting in a 0.6 K temperature difference.
For wall surfaces the mean difference between the two aerodynamic resistances is 31 $W/m^2$, resulting in a 0.2 K mean temperature difference for the 0.5m grid, and 29 $W/m^2$, resulting in a 0.1 K mean temperature difference for the 2.5m grid.
For ground surfaces the mean difference between the two aerodynamic resistances is 29 $W/m^2$, resulting in a 0.4 K temperature difference for the 0.5m grid, and 25 $W/m^2$, resulting in a 0.2 K temperature difference for the 2.5m grid.

The mean temperature differences between $R_h$ values for roof, wall, and ground surfaces are relatively small, but the maximum differences can be significant: For instance, the maximum difference for roof surfaces of the 0.5m grid, between the $R_h$ of 150 s/m and 30 s/m is 113 $W/m^2$, resulting in a 6.8 K temperature difference. For the 2.5m grid the maximum difference between the $R_h$ of 150 s/m and 30 s/m for roof surfaces is 78 $W/m^2$, resulting in a 4.6 K temperature difference.

### 5.4.2. Comparison of the Grids for Both Aerodynamic Resistances

The mean SHF differences between the two grids for different surfaces vary. For roof surfaces, the mean SHF difference between the two grids is 15 $W/m^2$ for the $R_h$ of 150 s/m and 20 $W/m^2$ for the $R_h$ of 30 s/m, while for wall surfaces this is 12 $W/m^2$ and 14 $W/m^2$ for the respective $R_h$ values. The mean SHF difference for ground surfaces between the two grids is 34 $W/m^2$ for the $R_h$ of 150 s/m and 40 $W/m^2$ for the $R_h$ of 30 s/m.

Ground SVFs are affected most by the grid averaging procedures. The SHFs for the ground surfaces for the 0.5m AHN grid in figures 5.3a and 5.3b show large variations over time, but the rise in SHFs during daytime disappear for the ground surfaces for the 2.5m LES grid, in figures 5.3c and 5.3d. Where the ground surface SHF for the $R_h$ of 150 s/m reaches a maximum of 127 $W/m^2$ for the 0.5m grid, this is only 31 $W/m^2$ for the 2.5m grid. For wall surfaces the maximum difference in SHF between the two grids is only 9 $W/m^2$ for 150 s/m and 4 $W/m^2$ for 30 s/m, and for roof surfaces the maximum difference in SHF between the two grids is 55 $W/m^2$ and 29 $W/m^2$ for the two respective $R_h$ values.

The difference in surface temperature for an $R_h$ of 30 s/m and 150 s/m is shown in figure 5.4 for the two grids. The difference in surface temperature between the 0.5m and 2.5m grids is largest for ground surfaces, where the maximum temperature difference between the two grids is 6.6 K for $R_h$ = 150 s/m and 1.2 K for $R_h$ = 30 s/m. For roof surfaces, the maximum temperature difference is 3.1 K for $R_h$=150 s/m and 0.9 K for $R_h$ = 30 s/m. The maximum temperature difference for wall surfaces is minimal, with only 0.8 K for $R_h$=150 s/m and 0.03 K for $R_h$ = 30 s/m.

It is important to note that these SHF fluxes are amplified during extreme weather conditions, such as when buildings are heated to a temperature far from the outside temperature, which is explored in the next section 5.5.

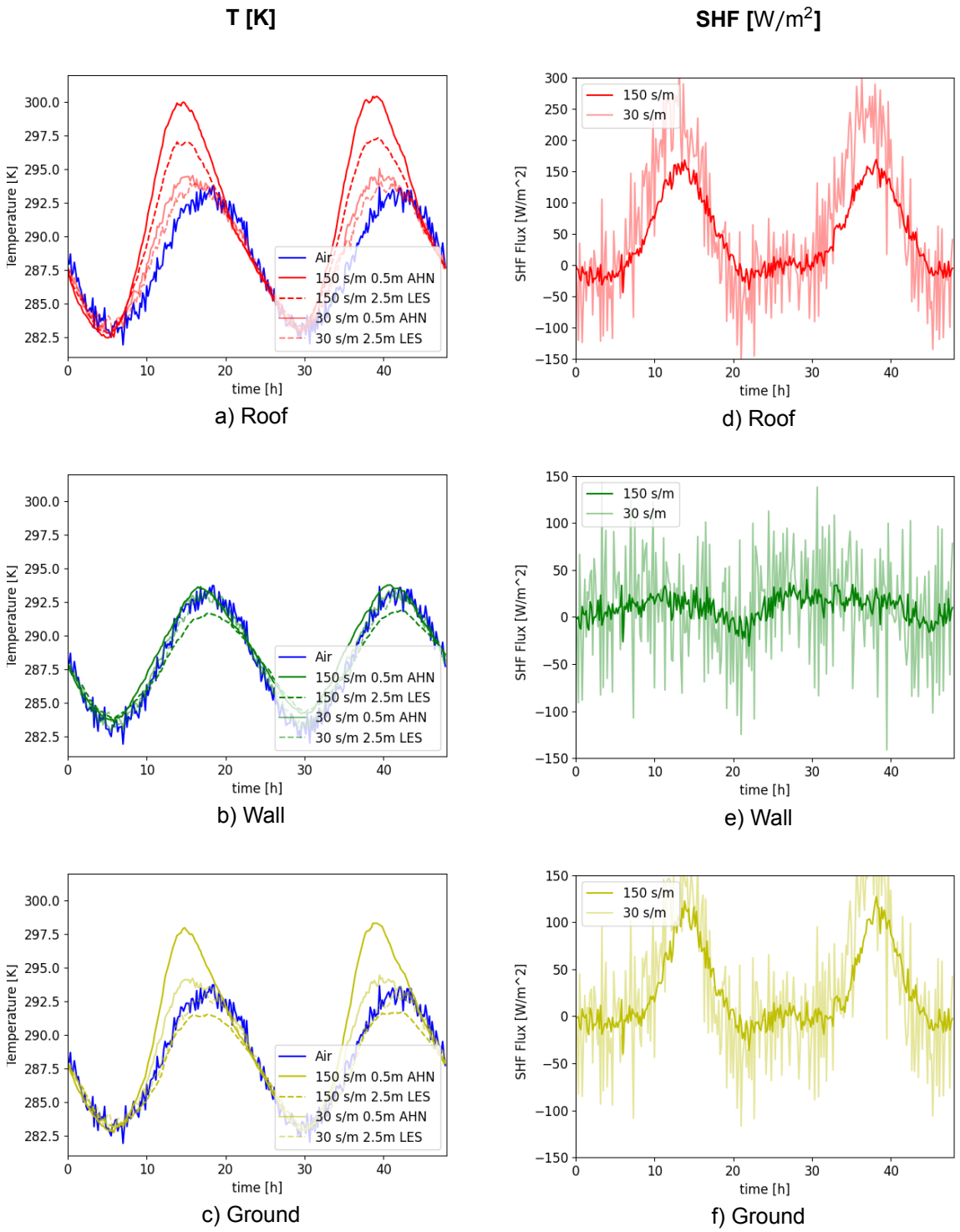


Figure 5.4: The surface temperatures on the left (a-c), and the SHF fluxes on the right (d-f), for an $R_h$ of 30 s/m and 150 s/m, for the 0.5m grid (solid lines) and the 2.5m LES grid (dashed lines)

## 5.5. Different Building Heating Temperatures

The temperature of buildings is usually kept within the range of 15-25 K for human comfort. This bottom layer boundary condition on the roof and wall surfaces changes the emitted grey body radiation and SHF. The effect of the boundary condition on the SEB is explored by varying $T_{building}$ and the outside weather conditions in table 5.2, and compare the temperature of the 7 surface layers of the two grids. Additional simulation parameters are provided in table 5.1.

| | ***Winter*** | ***Summer*** |
|---|---|---|
| $T_{air,average}$ | 273.15 K | 298.15 K |
| $T_{air,amplitude}$ | 5 K | 5 K |
| $T_{Building}$ | 20 K | 15 K |

Table 5.2: Outside temperature parameters for winter and summer. The temperature is a sinusoidal forcing as described in section 4.8

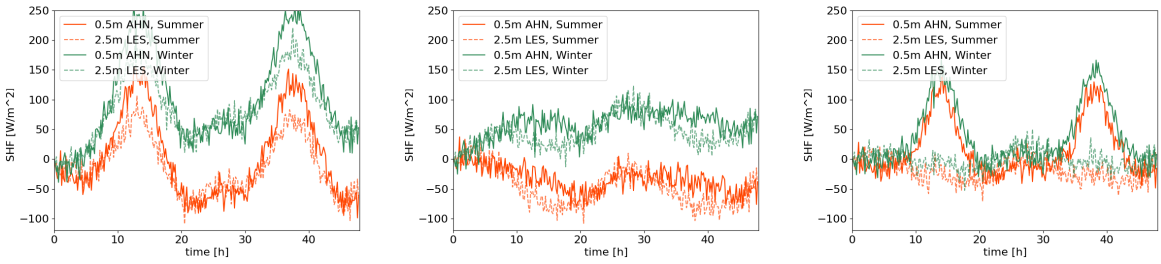


a) Roof b) Wall c) Ground

Figure 5.5: The SHFs for roof (a), wall (b) and ground (c) surfaces for winter and summer, for the 0.5m AHN grid (solid lines) and the 2.5m LES grid (dashed lines)

### 5.5.1. Sensible Heat Flux

The SHFs are compared for winter and summer for both grids in figure 5.5. In winter, roof and wall surfaces on both grids have SHF values greater than 0, indicating heat loss to the air. Ground surfaces experience less variation in SHF between winter and summer as they are not affected by the bottom layer temperature boundary condition.

The large variation between daytime and nighttime SHF disappears again for the 2.5m LES grid; The ground SHF flux for the 0.5m grid reaches a maximum of 139 $W/m^2$ in summer and a maximum of 167 $W/m^2$ in winter. For the 2.5m grid, this maximum SHF flux for ground surfaces is only 27 $W/m^2$ in summer and 51 $W/m^2$ in winter. The maximum difference between the two grids for roof surfaces is is 48 $W/m^2$ in summer and 38 $W/m^2$ in winter. The smallest difference between the two grids is found for wall surfaces, with a maximum difference of 9 $W/m^2$ in summer and 12 $W/m^2$ in winter.

### 5.5.2. Longwave Radiation

In figure 5.6 the net LW radiation is compared for both seasons and both grids. The net LW flux is affected by the outside temperature since the received LW radiation from the sky is calculated from the air temperature. Therefore, in summer (figure 5.6a), the received LW flux is higher, but surface temperatures are also higher. In both cases, the net radiative LW flux is negative, indicating that the building emits more LW radiation than it receives.

The radiative LW flux for roof and ground surfaces reaches its peak at midday, but not for wall surfaces. This is due to the LW-trapping effect, which was most prominent for wall surfaces. Regarding net LW radiation, the mean difference between the first and second grid for wall surfaces is 9 $W/m^2$ in summer and 10 $W/m^2$ in winter. For roof surfaces, the mean difference in net LW radiation between

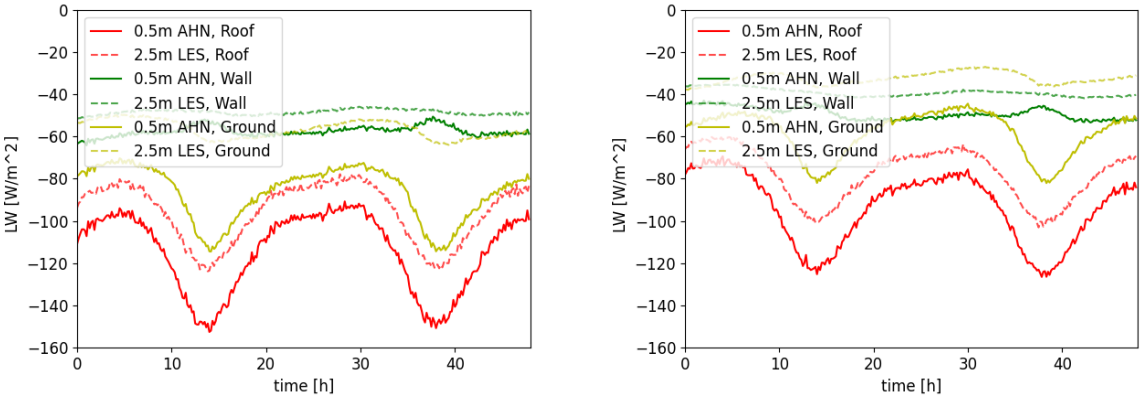


Figure 5.6: The net LW for all three surface types and the 0.5m AHN grid (solid lines) and the 2.5m LES grid (dashed lines) in summer (a) and winter (b)

the grids is 19 W/m$^2$ in summer and 16 W/m$^2$ in winter. The largest mean difference in net LW radiation between the grids is for ground surfaces, owing to the significant disparity in SVFs; 30 W/m$^2$ in summer and 26 W/m$^2$ in winter.

### 5.5.3. Surface Temperature

In figures 5.7 surface temperatures for both the winter and summer scenarios are compared. The surface consists of 7 layers, where layer 0 is the surface layer, which is in contact with the air, and layer 6 is the bottom layer, which experiences the bottom layer boundary condition.

In the winter scenario, the outside temperature is much lower than the building temperature, causing the building to heat the surroundings. In contrast, in the summer scenario, the outside temperature is higher than the inside temperature, causing the building to be heated by conduction as well as the received SW and LW radiation from the outside, while being cooled on the inside.

During summer, ground and roof surface temperatures exceed the air temperature, while the temperature for the bottom layer of walls and roofs is the lowest due to the bottom layer boundary condition. The maximum temperature difference between the two grids is highest for ground surfaces, with 5.8 K. For roof and wall surfaces, this maximum temperature difference is 2.7 and 2.2 K, respectively.

In winter, the ground surface temperature is higher than the air temperature because of the LW and SW radiation heating the ground. However, for the 2.5m LES grid, this effect is much smaller due to the lower SVFs. The maximum temperature difference in winter between the two grids is for ground surfaces, is 6.7 K. For roof surfaces, this maximum temperature difference is 2.7 K, and for wall surfaces, it is only 1.8 K.

The temperature difference between the two grids is largest for ground surfaces in both winter and summer and smallest for wall surfaces. The temperature difference between the two grids becomes smaller for every layer due to the restriction of the bottom layer boundary condition.

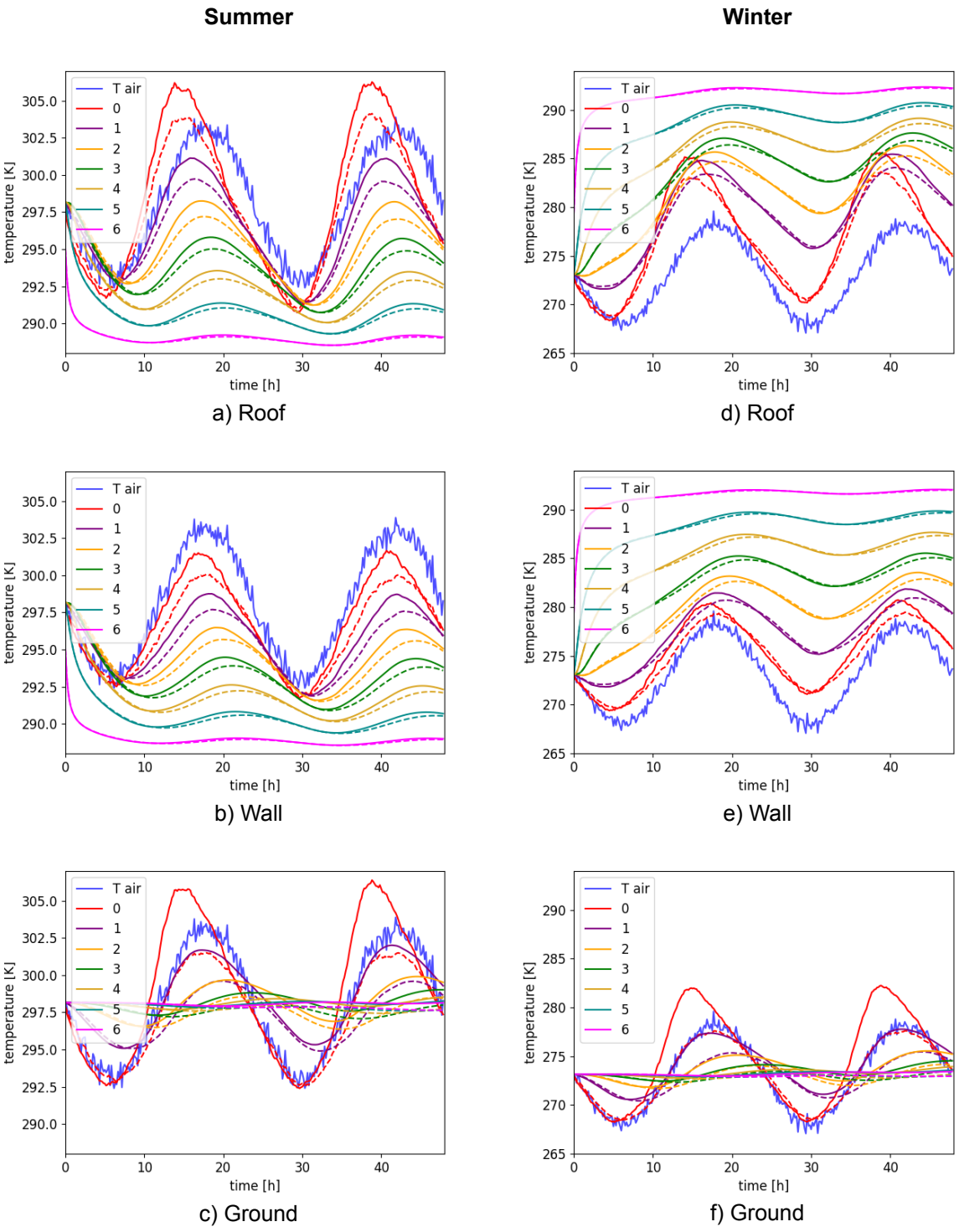


Figure 5.7: The temperature from top layer (nr. 0) to bottom (nr. 6) layer for roof (top), wall (middle) and ground (bottom) surfaces in summer (left, a-c) and winter (right, d-f), for the 0.5m AHN grid (solid lines) and 2.5m LES grid (dashed lines)

# 6

# Discussion and Recommendations

This thesis aims to investigate the impact of various parameters, including urban geometry and grid averaging techniques, on the temperature behaviour of urban surface areas. The study evaluated the influence of different components of surface energy balance, including surface fluxes and temperatures for ground, wall, and roof surfaces, for two grids: the 0.5m AHN grid and the 2.5m LES grid. For the 2.5m LES grid the SVF and SF values are much smaller, with the biggest difference of a factor 2 for ground surfaces. This results in temperature and flux differences between the two grids.

## 6.1. SVF and SF Computation

The computation of SVF and SF is based on an algorithm that uses DSM data to determine the SVF and SF for every point in the horizontal domain. The surfaces are classified into roof and ground surfaces based on their height. The exterior wall surfaces are identified by the difference in height between roof and ground surfaces, and their SVF and SF are estimated. The first step of the algorithm involves determining the SVF and SF for roof and ground surfaces, followed by the computation of SVFs and SFs for wall surfaces.

### 6.1.1. DSM Data

The data used by the algorithm to compute the SVF and SF is DSM data, which is data created with LiDAR (Light Detection and Ranging) to measure the elevation of the Earth's surface. It is important to note that no distinction is made between buildings, vegetation, and other objects such as bridges. Vegetation can affect the SVF in two ways. Firstly, the leaves of trees and low vegetation are often partially translucent, and secondly, the DSM data does not account for the larger surface area at the top of a tree compared to its trunk. These two effects result in the underestimation of the SVF.

To separate ground and roof surfaces, all surfaces with a height of 0 are categorized as ground surfaces, while those with a height greater than 0 are considered roof surfaces. However, this approach is not suitable for objects that are not considered ground surfaces or buildings, such as bus shelters, trees, lanterns, or cars. Even smaller objects, such as a passing dog or scrub, are filtered out because heights below a minimum height of 1m in the DSM data are set to 0 before the data is used in the SVF and SF algorithm.

### 6.1.2. The Discretization in SVF and SF Algorithms

In the SVF and SF algorithm, each datapoint higher than the point under evaluation obstructs the sky view and the width of this obstruction is converted to degrees, as shown in figure 3.3, where the two angles of the sides of the obstruction are called $\beta_{\text{min}}$ and $\beta_{\text{max}}$. The two angles $\beta_{\text{min}}$ and $\beta_{\text{max}}$, are calculated using $\Delta x_{\text{AHN}}$ and the distance to the point only, with equations 3.3 and 3.4. However, since we use square data boxes, the width of obstruction also depends on the location of that obstructing datapoint relative to the point under evaluation. The minimum obstruction width is exactly equal to $\Delta x_{\text{AHN}}$, if the datapoint has the same x or y coordinate as the point under evaluation, while the maximum width

occurs at an angle of 45 degrees and is equal to the diagonal of the box, $\sqrt{2\Delta x_{AHN}{}^2}$.

This discretization error also affects the SF algorithm. When a gridbox, with angle $\beta$ from the point currently under evaluation, blocks the sun, the width of the shadow that falls on the current block under evaluation varies, depending on the relative position of the building to the sun, shown in figure 6.1.

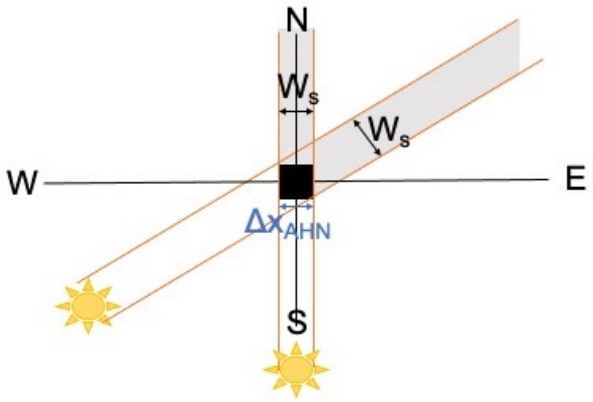


Figure 6.1: The shadow casted by a block with the sun in two different angles. The minimum width of the shadow produced by one block, named $W_s$, is the same as $\Delta x_{AHN}$. The maximum shadow width is when it would be at 45 degrees. Then it would cast a shadow with a width equal to the diagonal of the gridbox $\sqrt{2\Delta x^2_{AHN}}$

Figure 6.2 shows how the relative position of the sun, the building and the obstruction cause slightly different shadows.

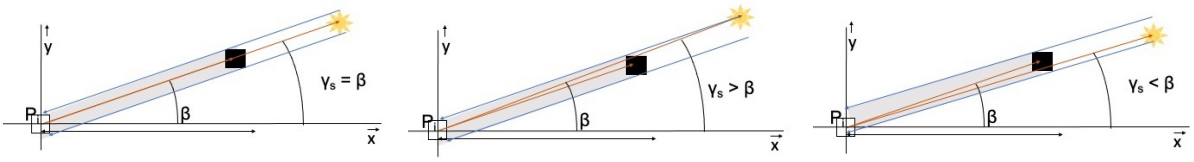


a) $\gamma_s = \beta$ b) $\gamma_s > \beta$ c) $\gamma_s < \beta$

Figure 6.2: a) The azimuth angle of the sun, $\alpha_s$, is exactly equal to the angle of the obstruction with the point under evaluation, called angle $\beta$. b) The angle is slightly smaller or larger (c). In all three scenarios the SF will be 0 for the point under consideration, though in the third scenario the box is slightly illuminated at the bottom.

The discretization error causes an overestimation of the SF and SVF, and a higher SVF and SF can lead to surfaces warming up more during the day and emitting more LW radiation during the night. For the 0.5m AHN gridsize, this effect is very small. However, when using larger grid cells this effect can become significant and contributes to the underestimation we saw for SVFs computed for larger grid cells.

### 6.1.3. Wall SVF and SF

For all points on the horizontal domain, the SVF and SF are computed using the algorithm. The vertical wall surfaces are determined from the height differences between neighbouring data points. Every building has walls on all four sides, and the SVF and SF are height dependent, thus must be integrated over the vertical walls. The computation of $SVFs_{wall}$ and $SFs_{wall}$ with an algorithm would therefore require large computational resources.
To avoid this the SVF and SF are estimated; The infinite canyon equations for $SVFs_{wall}$ and $SFs_{wall}$ are related to $SVFs_{road}$ and $SFs_{road}$. This is a simplified approach that has the benefit of reducing computations significantly.

We assume that for sky view and shadowing the relation between roads and walls is similar to an infinite canyon. The assumption that roads resemble infinite canyons is similar to the assumption on which the Urban Canopy Model of Masson is built. The difference in approach, is that Masson assumes a canyon with a fixed height-over-width ratio. By integrating the equations for the SF and SVF over all azimuthal angles, the variation of directions in streets is taken into account. In this model we do not assume one height-over-width ratio, but SVFs are computed with an algorithm, resulting in a more accurate and detailed SVF for every location, based on height data. From that location-specific SVF for road surfaces, a height-over-width ratio is deduced. This approach therefore improves the representation of the variability of different street widths and buildings heights that occurs in a realistic city.

The roads in cities are however not infinite, and cities are composed of multiple streets that cross each other. Due to lack of data for the SVFs of wall surfaces, the error of the computed SVFs for wall surfaces could not be found. This is left as a recommendation for further studies, if measurements of wall surface SVFs would be performed.

In a real city some walls are radiated during the entire day and reach high temperatures compared to for example northern-facing walls, which do not receive direct sunlight. The equation used for $SF_{wall}$ is integrated over $360^{o}$ in the azimuthal direction; it is averaged over sunlit and shadowed walls. Emitted and absorbed LW are not linear with surface temperature. Not taking the differences in wall temperature into account could therefore influence the average surface temperature.

## 6.2. Reflections

In the model used in this study, not only are the SVF and SF for wall surfaces adopted from Masson's model, but also the view factors needed to calculate the SW and LW reflections are adopted. This approach provides simplicity and guarantees that all view factors add up to one, which is necessary for energy conservation. When the view factors would have been calculated with an algorithm that uses the DSM data, this may not necessarily be true.

The height variability in a city with varying building heights can complicate the calculation of view factors of wall surfaces since the roof surfaces of low buildings can also reflect on the wall surfaces of higher buildings, resulting in two unknowns. To avoid this, the reflection from roof to wall surfaces is neglected, and the wall view factor (WVF) for wall surfaces can be computed as the remainder of 1 minus $SVF_{wall}$ and $GVF_{wall}$, as shown in eq. 3.12. This simplification affects the results since the study shows that the SVF for roof surfaces is well below 1, meaning that the amount of walls that are higher than certain roof surfaces is substantial.

In the model, only first-order reflections are taken into account, and the accuracy of the model depends on several factors, such as the assumptions made about the material properties of the surfaces and the radiation. The simulations in this study used building materials with certain albedos and emissivities, for which the reflected fluxes among surfaces were not substantial, which supports the negligence of further reflections. However, this result is dependent on the material properties used in the simulations. To further investigate the effect of reflections, other materials should be evaluated, and the possibilities and necessity of incorporating additional reflections could be explored.

The assumption of diffuse reflection may not be valid in all cases, and it may be necessary to use a more detailed reflection model to accurately capture the behavior of the system. Another assumption is that LW irradiation is uniform, though in reality temperatures may be different near ground surfaces compared to roof surfaces, causing the LW radiation emitted by air particles to vary with location (Schrijvers et al., 2015).

## 6.3. Simulation Parameters

The two different grids result in large difference in SVF and SF values, which result in temperature differences op to around 6 K for the simulations run in this study. The simulations are affected by all simulation parameters, of which only some, such as aerodynamic resistance, outside temperature and building temperature, were discussed. Other parameters that influence the surface energy balance

which were not discussed are the material properties and the inclusion of vegetation. The material properties of soil, grass and other vegetation is different from that of artificial building materials. Secondly, vegetated surfaces experience a latent heat flux, which is not taken into account in the model.

In all simulations the materials of the layers of the surfaces are the same. Different materials retain heat differently, which would result in a different temperature evolution. Future studies could perform a sensitivity analysis to explore how material properties affect the SEB and which parameters are the most critical to accurately simulate urban energy balance.

## 6.4. Aerodynamic Resistance to Heat

The impact of variations in SVF and SF on the temperature evolution are investigated, with the simulation parameters listed in table 5.1 being a key factor in determining the results. Among these parameters is the Aerodynamic Resistance to heat ( $R_h$), which is kept constant and identical for both simulations. However, $R_h$ is geometry-dependent in reality, and would therefore differ between the two grids. This would impact the Surface Heat Flux (SHF) and net radiation at the top layer, as described in section 5.4. The results indicate that $R_h$ has a significant effect on the difference in SHF flux and temperature. Investigating the influence of grid geometry on the aerodynamic resistance of the surface would be advisable, but is beyond the scope of this research.

Overall, the result highlight the importance of considering urban geometry and grid averaging techniques in understanding the temperature behavior of urban surface areas. The findings suggest that more detailed grids, such as the 0.5m AHN grid, provide very different results compared to LES-averaged grids.

# 7

# Conclusion

A surface energy balance model is developed to simulate heat fluxes and temperatures in urban context. The main goal is to better understand the influence of urban geometry on surface temperatures. To this end, two grids were created with different building-resolving methods, which results in different geometries. The first grid is the 0.5m resolution height grid. A second grid is averaged over the 0.5m grid with a method used in LES modelling, where 3D grid cells are considered. An LES grid cell is considered part of a building if the volume of the grid cell is more than half filled, and empty if it is less than half filled. The grid cell dimensions of the second grid are 2.5m in x-,y- and z-direction.

## SVF and SF Differences

To capture the geometry differences the sky view factor (SVF) and shadow factor (SF) are computed using two algorithms. This study compares the SVF maps to the maps provided by the KNMI, which used data that was at least 6 years older, and has missing values for 5-10% of the datapoints. Moreover, the KNMI calculates the height of the horizon in 16 directions, instead of taking all obstacles within the maximum radius into account. The average difference is around 10% with the KNMI.

The SVF and SF are heavily influenced by using different grids; The mean SVF is 0.38 for the 2.5m grid versus 0.6 for the 0.5m grid. These differences are the largest for ground surfaces with 0.18 versus 0.48. The roof SVF has a decrease of 0.46 versus 0.68 and the wall SVF has a decrease of 0.15 versus 0.31. For the mean SF the peak throughout the day disappears for larger grid cells, resulting in less shortwave (SW) radiation being absorbed during the daytime.

## Shortwave Radiation

For ground surfaces the difference in net absorbed SW radiation is the greatest because the $SVF_{ground}$ differs relatively most for the two grids, with maximum values of 373 $W/m^2$ for the 0.5m grid and 121 $W/m^2$ for the 2.5m grid. For roof surfaces the maximum net SW values are 465 $W/m^2$ versus 348 $W/m^2$, and for wall surfaces the maximum net SW are 138 $W/m^2$ versus 71 $W/m^2$ for the 0.5m and 2.5m grid respectively. The difference in absorbed SW is mainly caused by the radiation absorbed from the sky.

## Longwave Radiation

Surfaces with higher SVFs absorb more SW radiation during the day, but lose that heat by emitting more longwave (LW) radiation during the night. Surfaces with lower SVFs retain their heat at night, and the difference between daytime and nighttime LW emission decreases. This increased nightly heat retainment indicates a higher urban heat island effect for the 2.5m grid. This effect is the largest for ground surfaces, where the difference between minimum and maximum net LW radiation is only 11 $W/m^2$ for the 2.5m grid but 38 $W/m^2$ for the 0.5m grid. The 2.5m grid predicts a larger LW contribution from other surfaces, indicating a larger LW-trapping effect, whereas the 0.5m AHN grid predicts a larger LW contribution from the sky.

## Surface Temperatures

The net radiation differences, cause a difference in predicted surface temperature. The received SW fluxes from the sky are larger than the received LW fluxes. The peak surface temperature and the temporal fluctuations in temperature are shown to be underestimated when using the 2.5m grid. The biggest difference in peak temperature between the grids is for ground surfaces, with a difference of 5.84 K. The maximum temperature difference for roof surfaces is 2.58 K and for wall surfaces is 2 K.

## Conclusion

In conclusion, the choice of the grid can have a significant impact on surface temperature and energy fluxes. Surfaces with smaller SVFs absorb less SW radiation, which is the largest contribution to the net radiation during the day. Peak temperatures are therefore underestimated. Surfaces with smaller SVF values emit less LW radiation and have higher view factors, leading to a larger LW-trapping effect. The SHF is also affected by the choice of grid size. The building temperature, outside weather conditions and material properties, influence the simulation results, and should therefore be varied in simulation to gain insight into the quantitative differences.

Overall, the result highlights the importance of considering urban geometry and grid averaging techniques in understanding the temperature behaviour of urban surface areas. The findings suggest that a more detailed grid, such as the 0.5m AHN grid, and coarser grids, such as the LES grid, provide very different results in SEB simulations of the city.

# A

# Appendix: Visualisation of the SVF

As discussed in the introduction another way of computing the SVF is by using fish eye images. This is however not realisable for large areas due to lack of the required images on a small enough grid size. The fish eye images do provide a good visualisation of the SVF of a point. To convert the computed SVF to a fish eye image one can plot the array of maximum blocking heights versus the horizontal angle as a circular histogram. In the three figures below the SVF is visualized in this way. The grey planes are obstructions and the blue space in between is the sky.

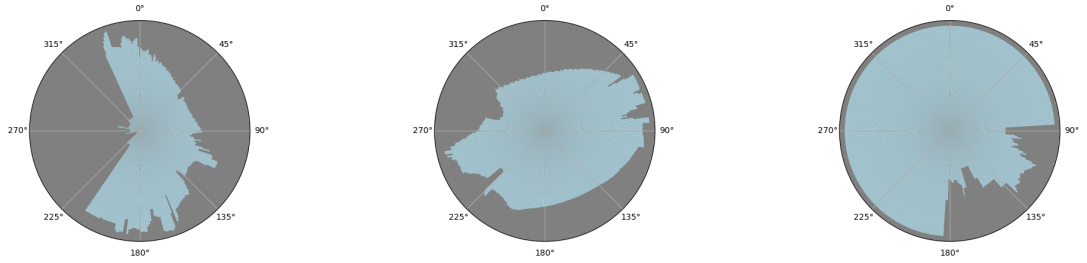


a) Point 1: SVF = 0.486 b) Point 2: SVF = 0.633 c) Point 3: SVF = 0.898

Figure A.1: Visualisation of the SVF for 3 points on the AHN. a) The SVF is 0.486. Looking at the large blocking and its sharp edges east ward of the point this is presumably very close to and to the right of a large building. b) The SVF is 0.633. This looks like a point in a street from west to east with buildings on each side of similar height. c) The SVF is 0.898. This point is most presumably in a park or large open space, or at the top of a high building.

# B

# Appendix: SVFs for 2 more neighbourhoods

## B.1. 2nd Neighbourhood

For a second neighbourhood in Rotterdam, shown in B.1a, distributions and SVF maps are again calculated.
Figures B.1b and B.1c again show that the SVF map based on a 2.5m grid resolution is overall much lighter, indicating a higher SVF, and less contrast is visible.

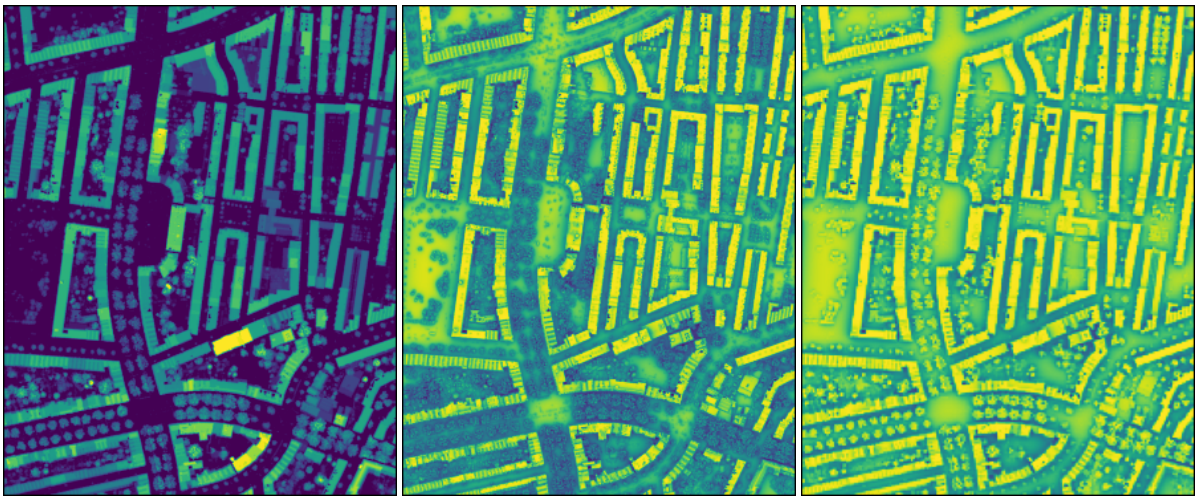

a) Height b) SVF 0.5m c) SVF 2.5m

Figure B.1: a) Height of data set 2. b) SVF for dataset 2 on 0.5m grid. c) SVF for dataset 2 averaged over 2.5m.

### B.1.1. SVF PDFs

The distributions for 0.5m and 2.5m resolution are similarly shaped as in the first neighbourhood. Again the amount of horizontal surfaces classified as road surfaces, is smaller for the 2.5m resolution dataset, with a difference of 22.4% versus 44%.

## B.2. 3rd Neighbourhood

The third neighbourhood has more open spaces, but higher buildings. This results in a larger variability in height, a much higher maximum height, but a lower building density.

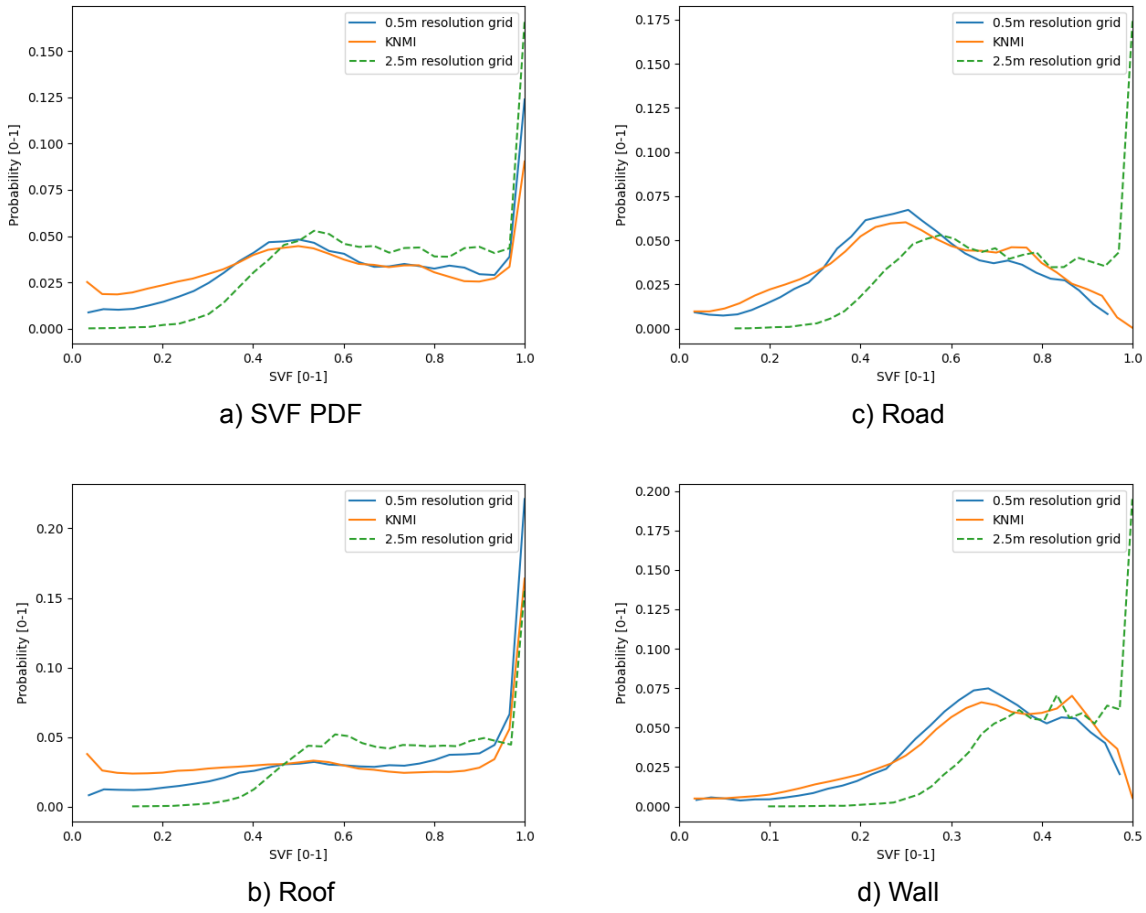


Figure B.2: a) SVF PDF for dataset 2, Split in roof (b) and road (c) surfaces. d) From the road SVF the wall SVF is deduced

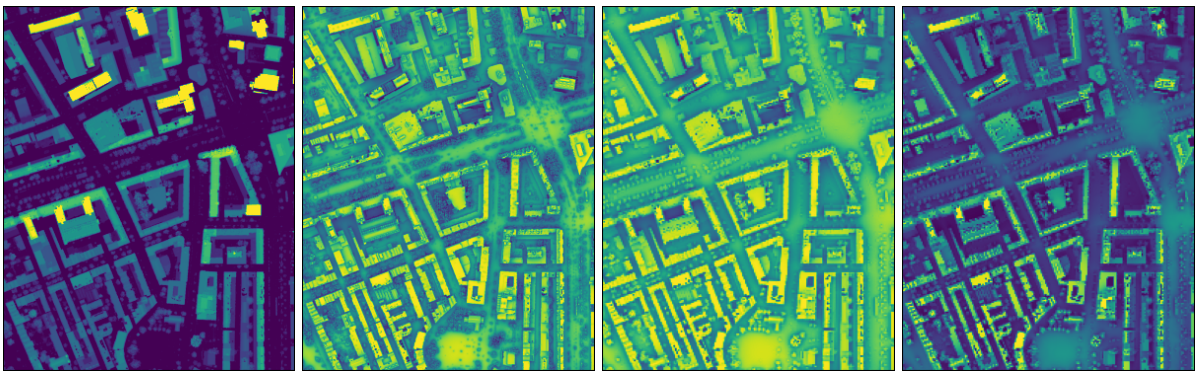


Figure B.3: a) Height of data set 3. b) SVF for dataset 3 on 0.5m grid. c) SVF for dataset averaged over 2.5m. d) SVF calculated with LES method over 2.5m

### B.2.1. SVF PDFs

There are more road surfaces, which shows in the bigger bump in the SVF distribution. A larger variability in height causes that the SVF for roof surfaces is more spread out instead of concentrated in the highest columns, but the shape of the third distribution is still similar to the first two. Using a 2.5m grid resolution again gives a decrease in the fraction of surfaces classified as road surfaces, of 25.6% vs 45%.

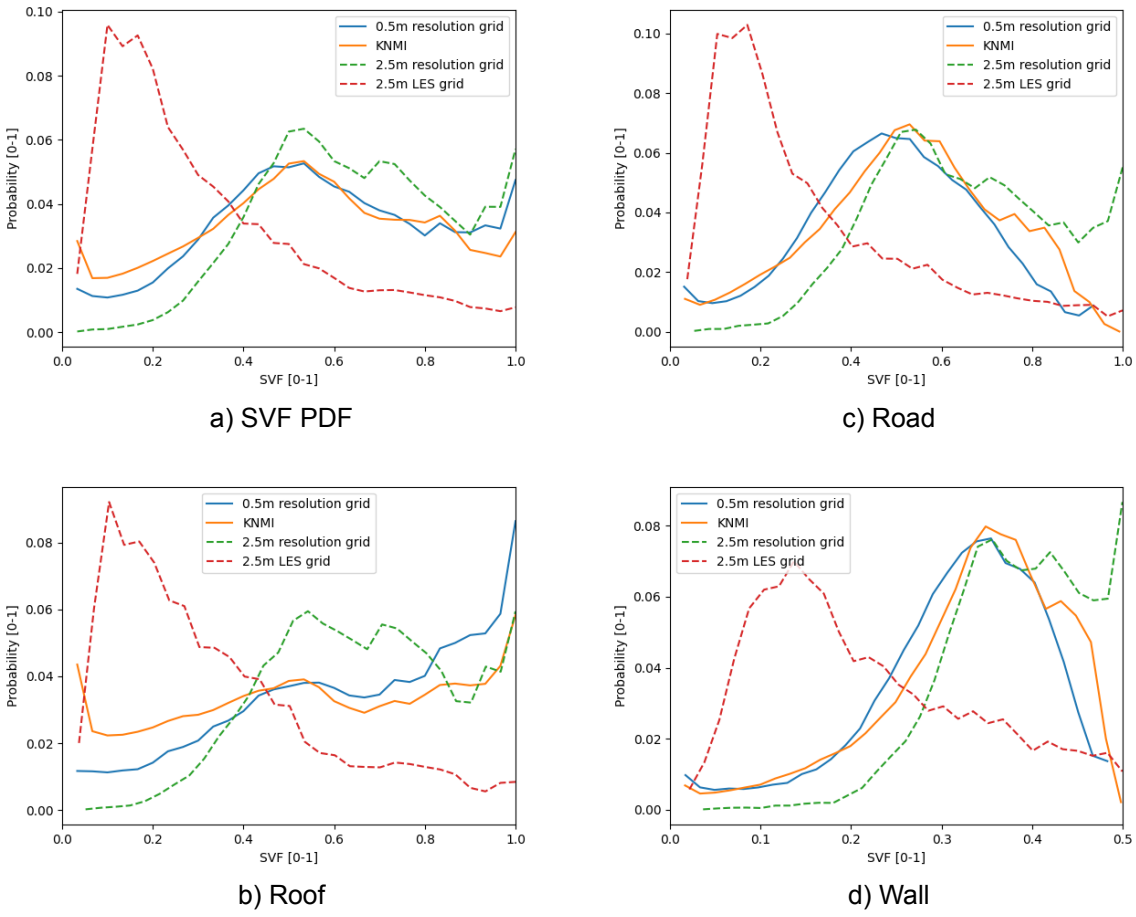


Figure B.4: a) SVF PDF for dataset 3, split in roof (b) and road (c) surfaces. d) From the road SVF the wall SVF is deduced (bottom right)

# C

# Appendix: Solar Position 1st of November

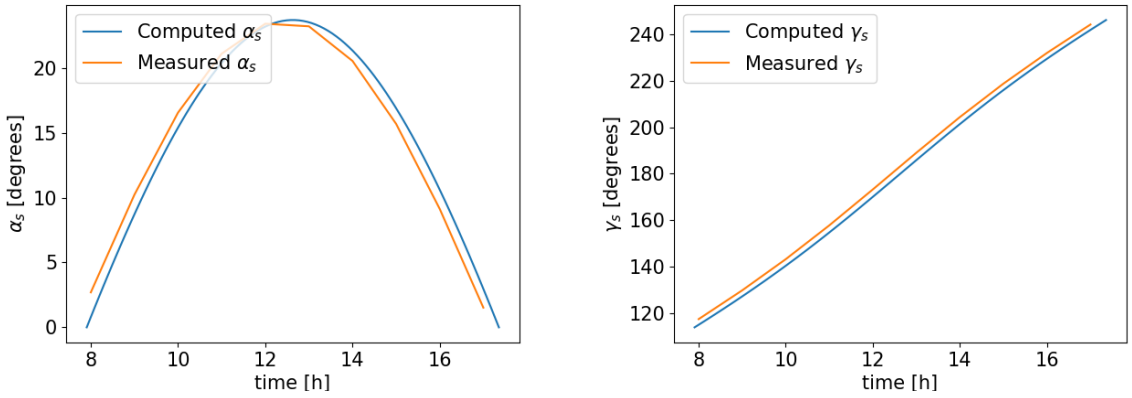


a) Elevation Angle b) Azimuth Angle

Figure C.1: Elevation (a) and azimuth (b) angle during daytime on Nov 1st in Rotterdam, calculated values and from (Keisan Casio, 2022)

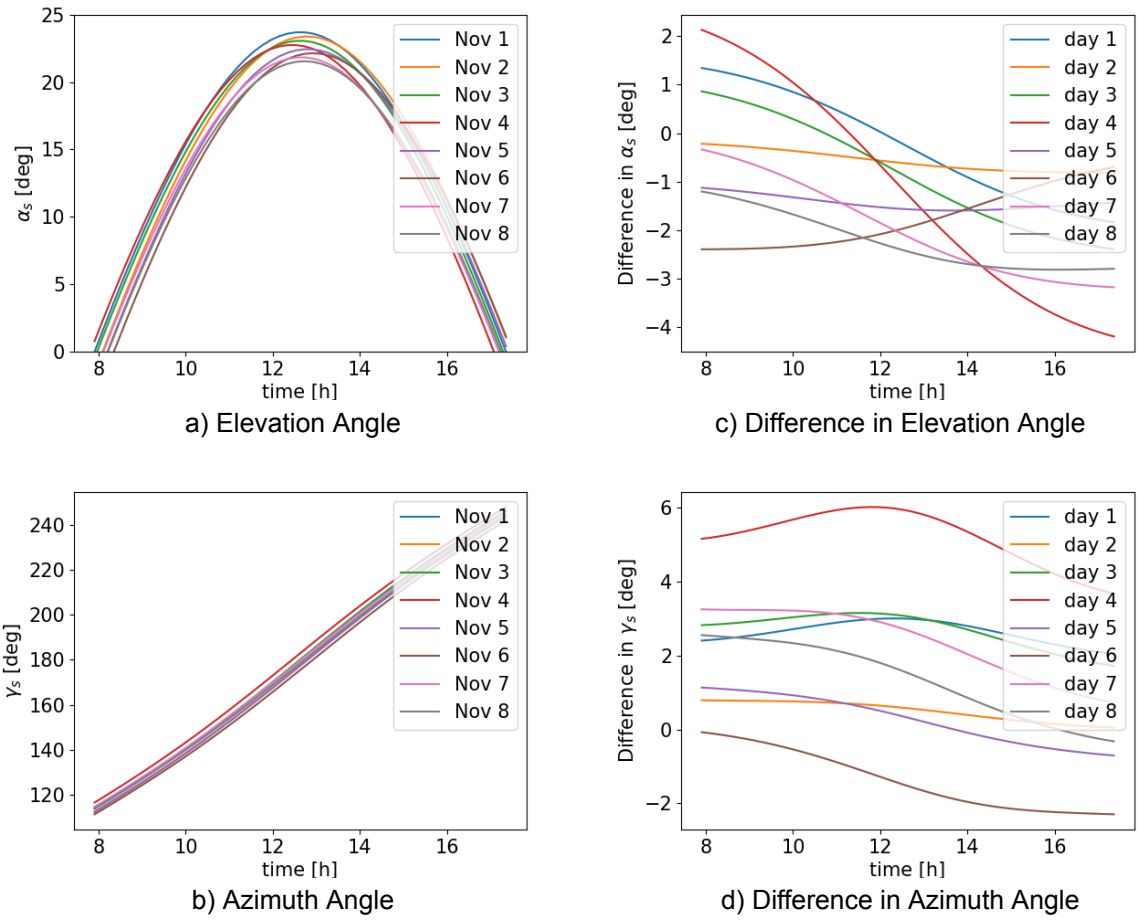


Figure C.2: On the left we see the elevation angle (a) and azimuth angle (b), during 7 consecutive days in November. On the right we see the difference with day 1 in elevation angle (c) and azimuth angle (d) during the same 7 consecutive days

# D

# Appendix: Shadow Factor Averaging

## D.1. SF Distributions for gridratio 25

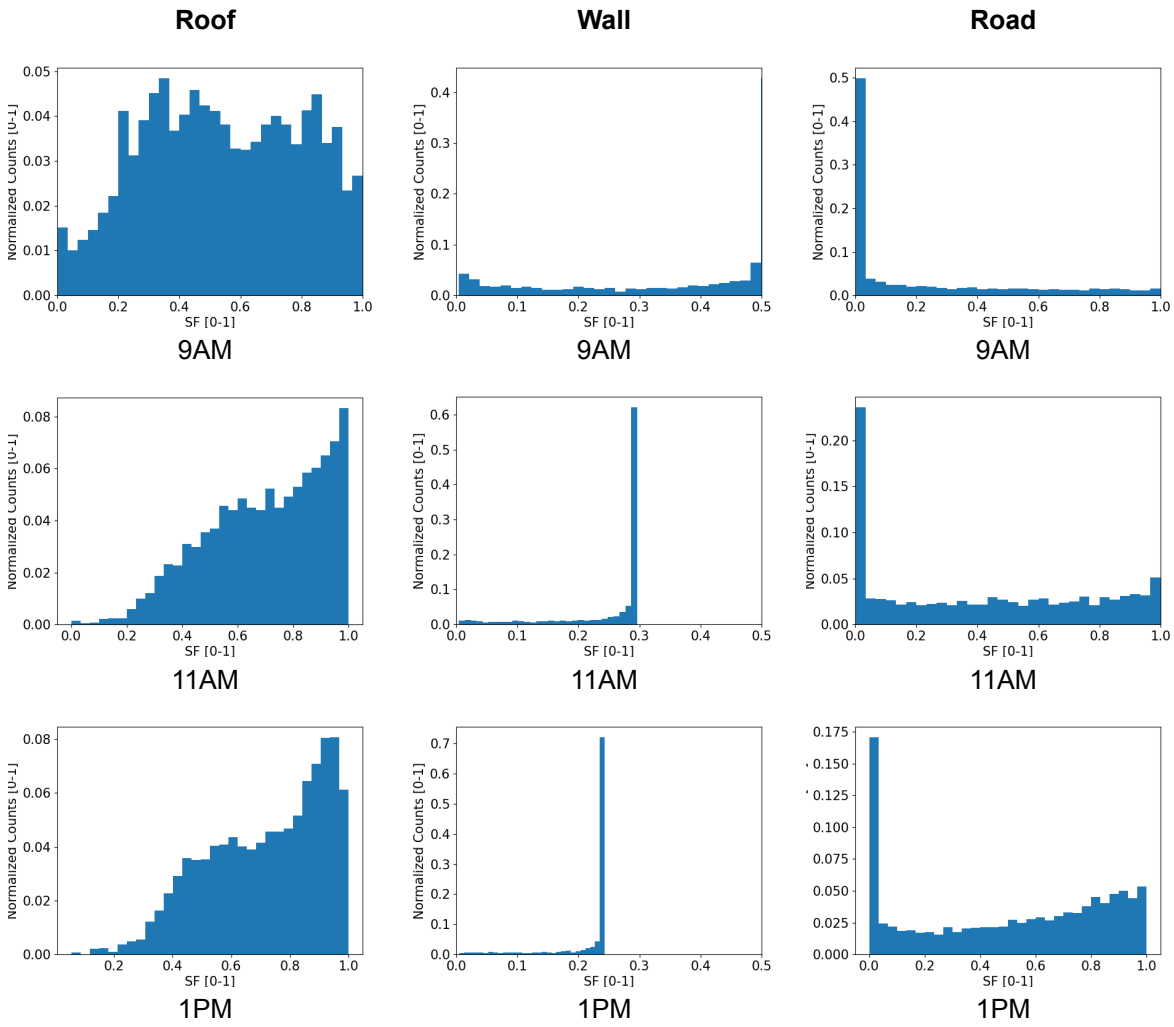


Figure D.1: SF distributions for roof (left), wall (middle) and road (right) surfaces, at 9AM (top), 11AM (middle) and 1PM (bottom), with a gridsize of 12.5m

## D.2. SF Distributions for gridratio 50

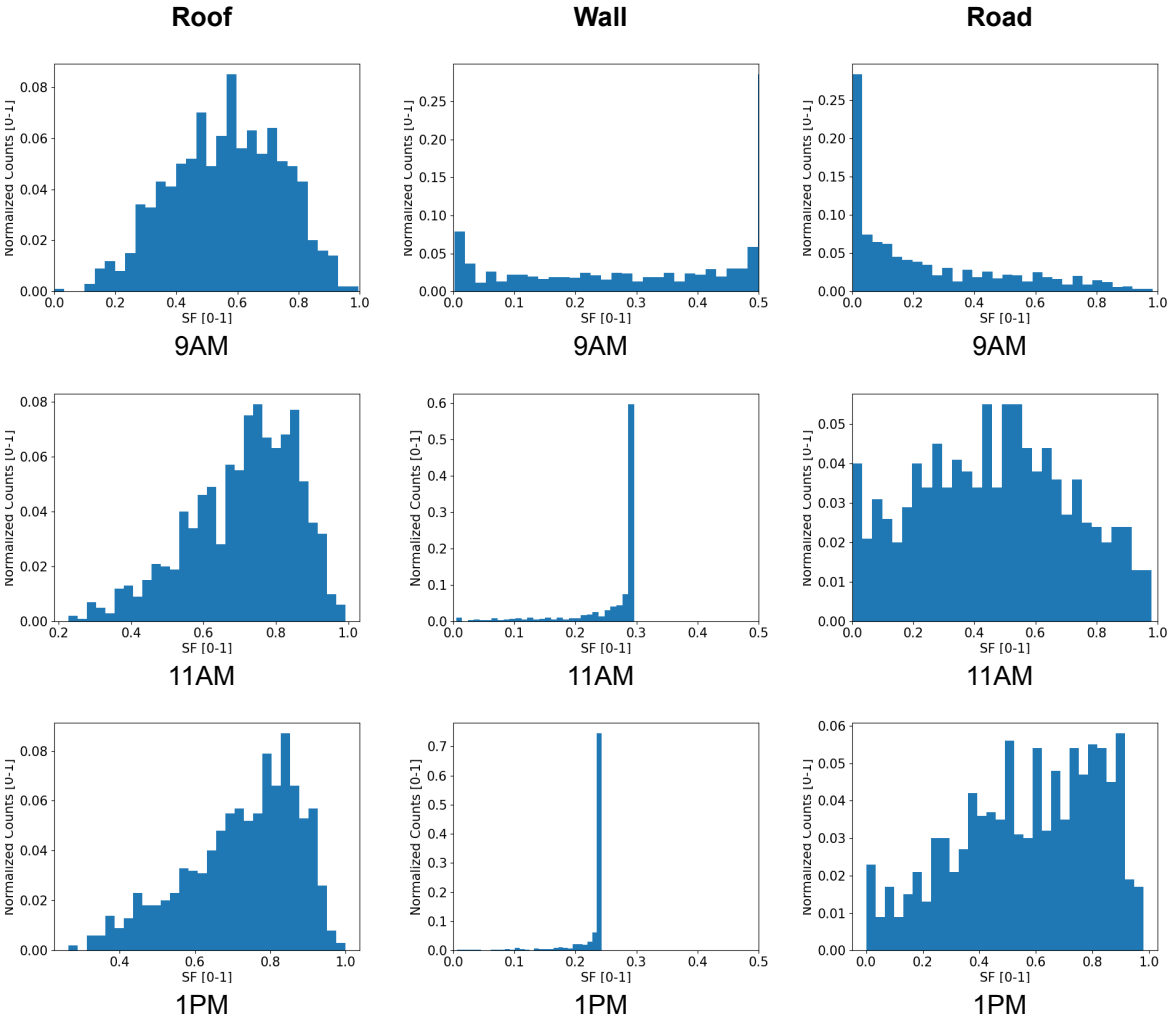


Figure D.2: SF distributions for roof (left), wall (middle) and road (right) surfaces, at 9AM (top), 11AM (middle) and 1PM (bottom), with a gridsize of 25m

# E

# Appendix: 3rd Grid

The LW and SW components for a third grid are compared to the 0.5m AHN grid LW and SW components. This third grid is averaged with the method described in 4.1 but with a much larger gridcell of $\Delta x_{LES}$=12.5m, $\Delta y_{LES}$=12.5m and $\Delta z_{LES}$=10m.

The average SVFs can be found in 4.1. The average SVFs are larger than the 2.5m LES grid and closer to the 0.5m AHN grid. The SFs are approximately constant during the day, where all roof surfaces receive direct sunlight during the entire day and all ground surfaces receive no sunlight during the day, since most building-height variability is removed. The mean SF is underestimated during the day but overestimated in the morning and evening.

For roof surfaces the SVF and SF are close to the 0.5m AHN grid, which shows in figures E.1a and E.1d: The SW and LW components are close together for the two grids.

The SF for ground surfaces is almost 0 everywhere during the entire day, which removes the large daily variations in absorbed SW radiation for the ground surfaces. The net SW radiation is largely caused by diffuse SW, and the direct SW radiation curve only shows a very small peak during the day.

The inclusion or exclusion of LW and SW reflection influences the two grids differently. The differences with the 0.5m AHN grid are much smaller for roof surfaces and slightly smaller for wall surfaces for the larger grid cell size. However for ground surfaces this grid also causes a large temperature difference with the 0.5m AHN grid, caused by the smaller SVF and SFs.

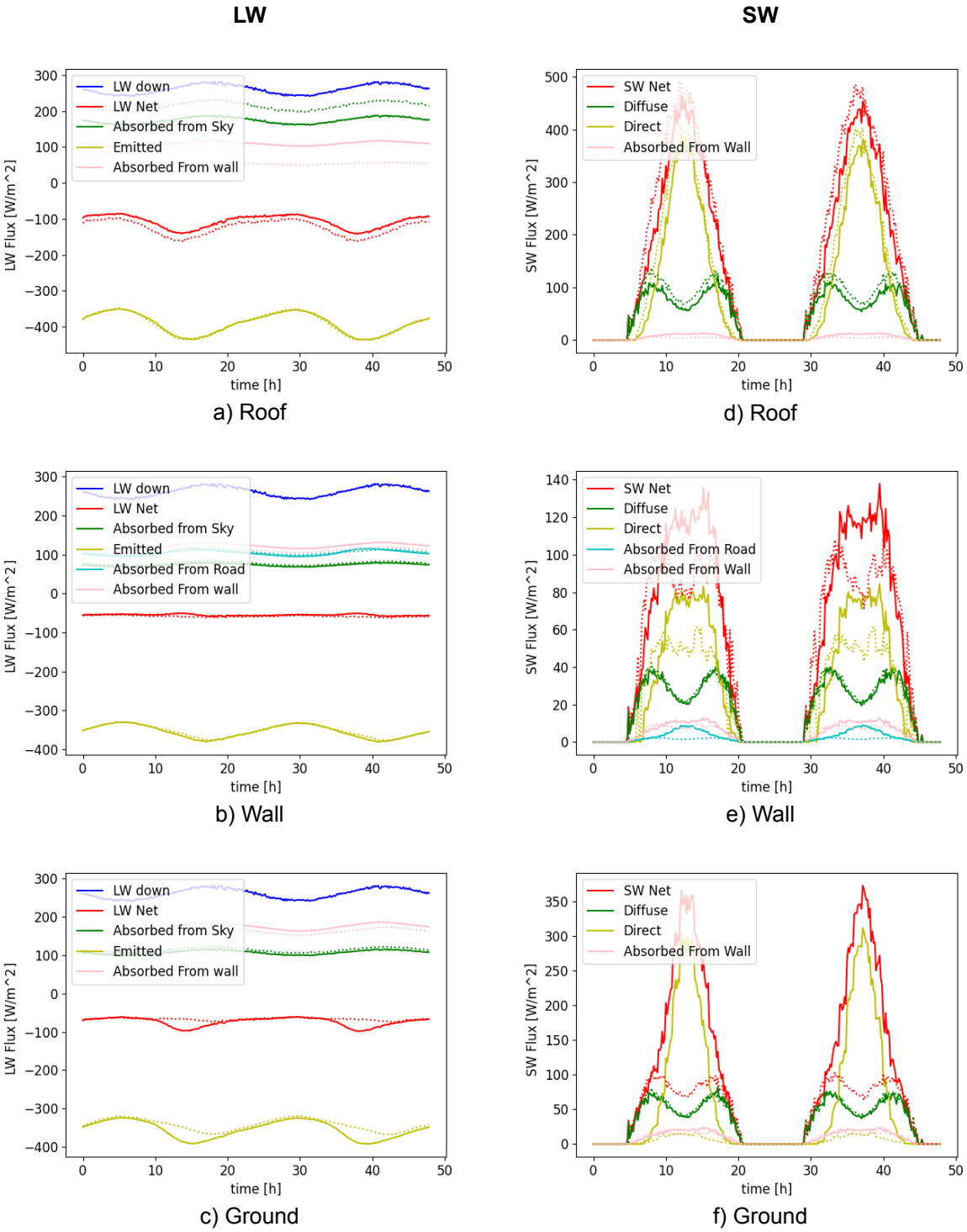


Figure E.1: The net longwave (LW, a-c) on the left, and shortwave (SW, d-f) on the right radiative flux of roof (top), wall (middle) and road (bottom) surfaces split into the different components. The ground surface flux is an area-weighted average of road and water surface flux calculated according to 4.5. In all figures the solid lines are for the 0.5m grid and dotted lines for the LES averaged grid where $\Delta x_{LES}$=12.5m, $\Delta y_{LES}$=12.5m and $\Delta z_{LES}$=10m.

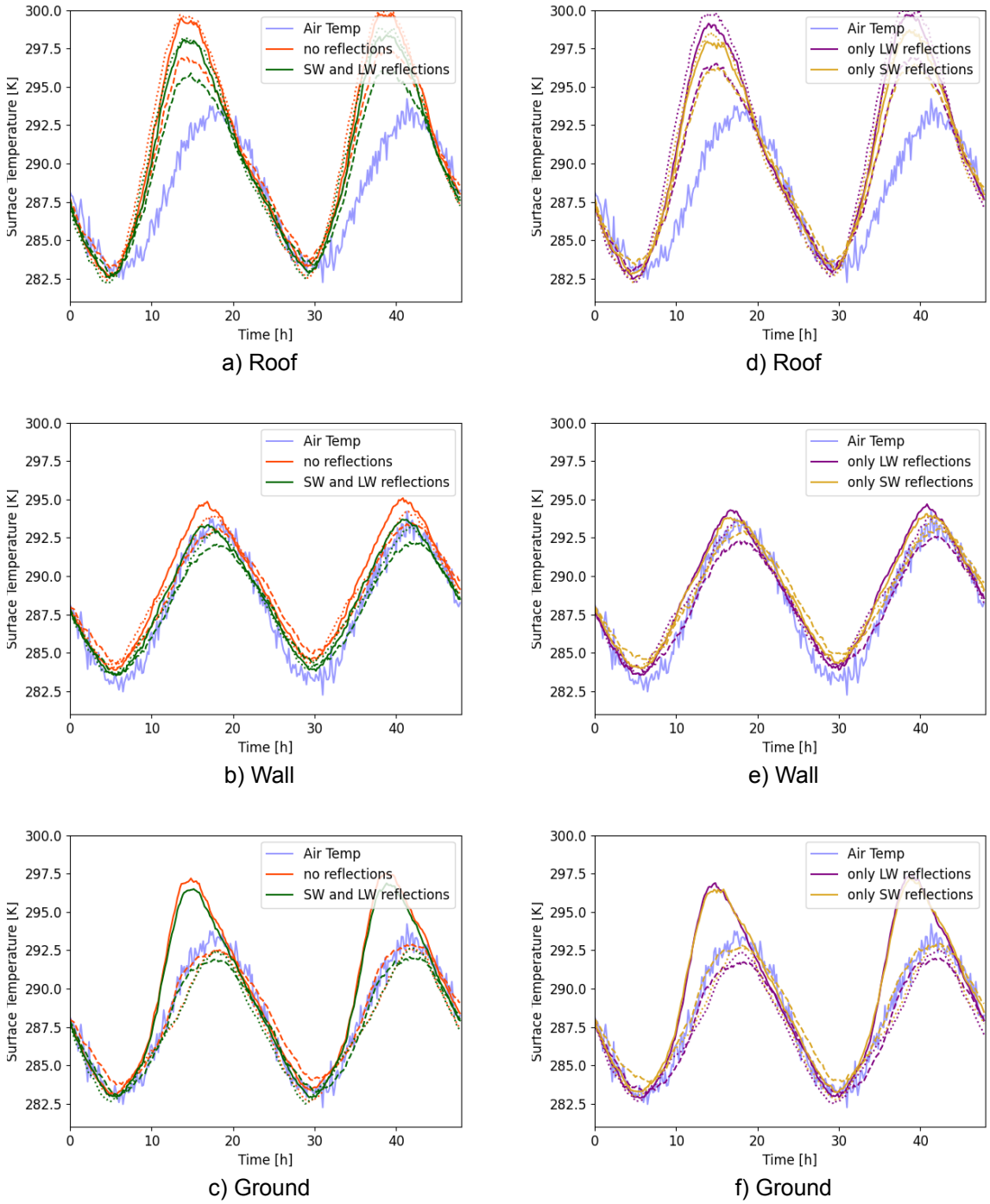


Figure E.2: On the left (a-c) we see the surface temperatures for roof (top), wall (middle) and ground (bottom), with the air temperature for reference, for all versus none reflections. On the right (d-f) we see the surface temperatures for only SW or only LW reflections. The solid lines are for the 0.5m AHN grid and the dotted lines are for the LES averaged grid where $\Delta x_{LES}$=12.5m, $\Delta y_{LES}$=12.5m and $\Delta z_{LES}$=10m.

# References


Agathangelidis, I., Cartalis, C., & Santamouris, M. (2019, 6). Integrating urban form, function, and energy fluxes in a heat exposure indicator in view of intra-urban heat island assessment and climate change adaptation. *Climate*, *7*(6). doi: 10.3390/cli7060075

Ali, U., Shamsi, M. H., Hoare, C., Mangina, E., & O'Donnell, J. (2021, 9). Review of urban building energy modeling (UBEM) approaches, methods and tools using qualitative and quantitative analysis. *Energy and Buildings*, *246*. doi: 10.1016/J.ENBUILD.2021.111073

An, S. M., Kim, B. S., Lee, H. Y., Kim, C. H., Yi, C. Y., Eum, J. H., & Woo, J. H. (2014, 6). Three-dimensional point cloud based sky view factor analysis in complex urban settings. *International Journal of Climatology*, *34*(8), 2685–2701. doi: 10.1002/joc.3868

Baghaeipoor, G., & Nasrollahi, N. (2019, 12). The Effect of Sky View Factor on Air temperature in High-rise Urban Residential Environments. *Journal of Daylighting, Vol. 6, Issue 2, pp. 42-51*, *6*(2), 42–51. Retrieved from http://www.solarlits.com/jd/6-42http://solarlits.com/jd/6-42 doi: 10.15627/JD.2019.6

Bernard, J., Bocher, E., Petit, G., & Palominos, S. (2018, 9). Sky view factor calculation in urban context: Computational performance and accuracy analysis of two open and free GIS Tools. *Climate*, *6*(3). doi: 10.3390/cli6030060

Bhattacharya, S., Braun, C., & Leopold, U. (2021, 9). An efficient 2.5D shadow detection algorithm for urban planning and design using a tensor based approach. *ISPRS International Journal of Geo-Information*, *10*(9). doi: 10.3390/ijgi10090583

Buter, K. (2002). Solar radiation, longwave radiation and daylight Annex to CIBSE Guide A chapter 2.

CBS. (2021). *Bodemgebruik; uitgebreide gebruiksvorm, per gemeente.* Retrieved from https://www.cbs.nl/nl-nl/cijfers/detail/70262ned

Center for Science Education. (2023). *Air Quality and Climate Change | Center for Science Education.* Retrieved from https://scied.ucar.edu/learning-zone/air-quality/air-quality-and-climate-change

Desthieux, G., Carneiro, C., Camponovo, R., Ineichen, P., Morello, E., Boulmier, A., … Ellert, C. (2018, 3). Solar energy potential assessment on rooftops and facades in large built environments based on lidar data, image processing, and cloud computing. Methodological background, application, and validation in geneva (solar cadaster). *Frontiers in Built Environment*, *4*. doi: 10.3389/fbuil.2018.00014

Dirksen, M., Ronda, R., Theeuwes, N., & Pagani, G. (2019). Sky view factor calculations and its application in urban heat island studies.
doi: 10.1016/j.uclim.2019.100498

Dozier, J. (1990). Rapid Calculation of Terin Parameters For Radiation Modeling From Digital Elevation Data. *IEEE Transactions on Geoscience and Remote Sensing*, *28*(5), 963–969. Retrieved from https://www.researchgate.net/publication/3200762_Rapid_Calculation_of_Terrain_Parameters_for_Radiation_Modeling_From_Digital_Elevation_Data doi: 10.1109/36.58986

Ferreira, D. G., Diniz, C. B., & Assis, E. S. d. (2021, 3). Methods to calculate urban surface parameters and their relation to the LCZ classification. *Urban Climate*, *36*, 100788. doi: 10.1016/J.UCLIM.2021.100788

Grimmond, C. S. B., & Oke, T. R. (1998). Aerodynamic Properties of Urban Areas Derived from Analysis of Surface Form.

Hammerberg, K., Brousse, O., Martilli, A., & Mahdavi, A. (2018, 4). Implications of employing detailed urban canopy parameters for mesoscale climate modelling: a comparison between WUDAPT and GIS databases over Vienna, Austria. *International Journal of Climatology*, *38*, e1241-e1257. doi: 10.1002/JOC.5447

Harman, I. N., & Belcher, S. E. (2006). The surface energy balance and boundary layer over urban street canyons. *Meteorol. Soc*, *132*, 2749–2768. doi: 10.1256/qj.05.185

Harman N. (2003). The energy balance of urban areas.

Heusinkveld, B. G., Steeneveld, G. J., Van Hove, L. W., Jacobs, C. M., & Holtslag, A. A. (2014, 1). Spatial variability of the rotterdam urban heat island as influenced by urban land use. *Journal of Geophysical Research*, *119*(2), 677–692. doi: 10.1002/2012JD019399

Jiao, Z. H., Ren, H., Mu, X., Zhao, J., Wang, T., & Dong, J. (2019, 2). Evaluation of Four Sky View Factor Algorithms Using Digital Surface and Elevation Model Data. *Earth and Space Science*, *6*(2), 222–237. Retrieved from https://onlinelibrary.wiley.com/doi/full/10.1029/2018EA000475https://onlinelibrary.wiley.com/doi/abs/10.1029/2018EA000475https://agupubs.onlinelibrary.wiley.com/doi/10.1029/2018EA000475 doi: 10.1029/2018EA000475

Kalogirou, S. A. (2022, 1). Solar Thermal Systems: Components and Applications—Introduction. *Comprehensive Renewable Energy*, 1–25. doi: 10.1016/B978-0-12-819727-1.00001-7

Kastendeuch, P. P. (2013, 5). A method to estimate sky view factors from digital elevation models. *International Journal of Climatology*, *33*(6), 1574–1578. Retrieved from https://www.researchgate.net/publication/258790521_A_method_to_estimate_sky_view_factors_from_digital_elevation_models doi: 10.1002/JOC.3523

Keisan Casio. (2022). *Solar elevation angle (for a day) Calculator - High accuracy calculation.* Retrieved from https://keisan.casio.com/exec/system/1224682277

KNMI - Data Services. (2019). *Sky View Factor of The Netherlands - Dataset - KNMI Data Platform.* Retrieved from https://dataplatform.knmi.nl/dataset/svf-nl-3

Kusaka, H., Kondo, H., Kikegawa, Y., & Kimura, F. (2001). *A SIMPLE SINGLE-LAYER URBAN CANOPY MODEL FOR ATMOSPHERIC MODELS: COMPARISON WITH MULTI-LAYER AND SLAB MODELS* (Tech. Rep.).

Lindberg, F., & Grimmond, C. S. B. (2010). Continuous sky view factor maps from high resolution urban digital elevation models. *Research*, *42*(3), 177–183. doi: 10.2307/24870333

Löwe, H., & Helbig, N. (2012). Quasi-analytical treatment of spatially averaged radiation transfer in complex terrain. *Journal of Geophysical Research Atmospheres*, *117*(18). doi: 10.1029/2012JD018181

Masson, V. (2000). *A PHYSICALLY-BASED SCHEME FOR THE URBAN ENERGY BUDGET IN ATMOSPHERIC MODELS* (Tech. Rep.).

Masson, V., Grimmond, C. S. B., & Oke, T. R. (2002). *EVALUATION OF THE TOWN ENERGY BALANCE (TEB) SCHEME WITH DIRECT MEASUREMENTS FROM DRY DISTRICTS IN TWO CITIES* (Tech. Rep.).

McShane, R., Driscoll, K., & Sando, R. (2017). Prepared in cooperation with the International Joint Commission A Review of Surface Energy Balance Models for Estimating Actual Evapotranspiration with Remote Sensing at High Spatiotemporal Resolution over Large Extents Scientific Investigations Report 2017-5087. Retrieved from https://doi.org/10.5066/F7DF6PDR. doi: 10.5066/F7DF6PDR

Middel, A., Lukasczyk, J., Maciejewski, R., Demuzere, M., & Roth, M. (2018, 9). Sky View Factor footprints for urban climate modeling. *Urban Climate*, *25*, 120–134. doi: 10.1016/J.UCLIM.2018.05.004

Oswald, S. M., Revesz, M., Heidelinde Trimmel, □., Weihs, P., Zamini, S., Schneider, A., … Lindberg, □. F. (2019). Coupling of urban energy balance model with 3-D radiation model to derive human thermal (dis)comfort. *International Journal of Biometeorology*, *63*, 711–722. Retrieved from https://doi.org/10.1007/s00484-018-1642-z doi: 10.1007/s00484-018-1642-z

Ratti, C., & Richens, P. (2004). Raster analysis of urban form. *Environment and Planning B: Planning and Design*, *31*(2), 297–309. doi: 10.1068/b2665

Schrijvers, P. (2020). Urban Climate at Street Scale Analysis and Adaptation. Retrieved from https://doi.org/10.4233/uuid:6d00bdc4-f985-4b3a-9238-38be68cb3f2f doi: 10.4233/uuid:6d00bdc4-f985-4b3a-9238-38be68cb3f2f

Schrijvers, P., Jonker, H., Kenjereš, S., & de Roode, S. (2015, 1). Breakdown of the night time urban heat island energy budget. *Building and Environment*, *83*, 50–64. doi: 10.1016/j.buildenv.2014.08.012

Suter, I., Grylls, T., Sützl, B. S., Owens, S. O., Wilson, C. E., & Van Reeuwijk, M. (2022). uDALES 1.0: a large-eddy simulation model for urban environments. *Geosci. Model Dev*, *15*, 5309–5335. Retrieved from https://doi.org/10.5194/gmd-15-5309-2022 doi: 10.5194/gmd-15-5309-2022

Tsirantonakis, D., & Chrysoulakis, N. (2022, 3). Earth Observation Data Exploitation in Urban Surface Modelling: The Urban Energy Balance Response to a Suburban Park Development. *Remote Sensing*, *14*(6). doi: 10.3390/rs14061473

Van Hove, L. W. A., Steeneveld, G. J., Jacobs, C. M. J., Heusinkveld, B. G., Elbers, J. A., Moors, E. J., & Holtslag, A. A. M. (2011). Assessment based on a literature review, recent meteorological observations and datasets provided by hobby meteorologists Exploring the Urban Heat Island Intensity of Dutch cities. Retrieved from www.alterra.wur.nl/uk

Wang, K., & Dickinson, R. E. (2013, 4). Global atmospheric downward longwave radiation at the surface from ground-based observations, satellite retrievals, and reanalyses. *Reviews of Geophysics*, *51*(2), 150–185. Retrieved from https://onlinelibrary.wiley.com/doi/full/10.1002/rog.20009https://onlinelibrary.wiley.com/doi/abs/10.1002/rog.20009https://agupubs.onlinelibrary.wiley.com/doi/10.1002/rog.20009 doi: 10.1002/ROG.20009

Wang, Z., Bou-Zeid, E., Au, S., & Smith, J. (2011, 9). Analyzing the sensitivity of WRF's single-layer urban canopy model to parameter uncertainty using advanced Monte Carlo simulation. *Journal of Applied Meteorology and Climatology*, *50*(9), 1795–1814. doi: 10.1175/2011JAMC2685.1

Wang, Z., Bou-Zeid, E., & Smith, J. (2011, 2). A Spatially-Analytical Scheme for Surface Temperatures and Conductive Heat Fluxes in Urban Canopy Models. *Boundary-Layer Meteorology*, *138*(2), 171–193. doi: 10.1007/s10546-010-9552-6

Yaghoobian, N., Kleissl, J., & Krayenhoff, E. S. (2010, 3). Modeling the thermal effects of artificial turf on the urban environment. *Journal of Applied Meteorology and Climatology*, *49*(3), 332–345. Retrieved from https://www.researchgate.net/publication/249603819_Modeling_the_Thermal_Effects_of_Artificial_Turf_on_the_Urban_Environment doi: 10.1175/2009JAMC2198.1

Yang, J., Menenti, M., Krayenhoff, E. S., Wu, Z., Shi, Q., & Ouyang, X. (2019, 6). Parameterization of urban sensible heat flux from remotely sensed surface temperature: Effects of surface structure. *Remote Sensing*, *11*(11). doi: 10.3390/rs11111347